L'impact du streamer de bleu jet sur la chimie stratosphérique

Chen Xu

UNIVERSITÉ D'ORLÉANS

ÉCOLE DOCTORALE

ENERGIE, MATERIAUX, SCIENCES DE LA TERRE ET DE L'UNIVERS

LABORATOIRE DE PHYSIQUE ET CHIMIE DE

L'ENVIRONNEMENT ET DE L'ESPACE (LPC2E)

THÈSE présentée par :

Chen XU

pour obtenir le grade de : **Docteur de l'université d'Orléans**

Discipline/ Spécialité : Sciences de la Terre et de l'Atmosphère

The effect of blue jet streamer on stratospheric chemistry

JURY

PR. Valéry CATOIRE	LPC2E/OSUC, Université d'Orléans	Président du jury
DR. Franck LEFEVRE	LATMOS/IPSL, Paris	Rapporteur
Phys. Serge SOULA	LA/OMP, Université de Toulouse	Rapporteur
PR. Sébastien PAYAN	LATMOS/IPSL, Sorbonne Université, Paris	Examinateur
Dr. Céline PLANCHE	LAMP/OPGC, Université Clermont Auvergne	Examinatrice
Dr. Sébastien CELESTIN	LPC2E/OSUC, Université d'Orléans	Examinateur
PR. Nathalie HURET*	LPC2E/OSUC, Université d'Orléans	Directrice de thèse

* LAMP/OPGC, Université Clermont Auvergne depuis 2018

Table of Contents

List of Figures

List of Tables

ACKNOWLEDGMENTS

I would like to express my deep gratitude to Nathalie Huret, my research supervisor, for her patient and professional guidance, enthusiastic encouragement, and her insightful and constructive research suggestions. Thank you for offering me the opportunity to participate in summer schools as well as the European geoscience union and the American geoscience union conferences. I am also grateful for the kindness and considerate support from Nathalie and her family for my everyday life in France.

I would like to express my gratitude to Sébastien Célestin, for his valuable support and constructive criticism during the development of my research work. Thank you for giving me detailed and insightful explanations of plasma physics. Thank you to Mathieu for his help in characterizing the dynamic electric field for my model.

I would like to offer my special thanks to Franck Lefèvre, who provided me with the chemical data from the REPOBUS model, to Frédéric Romand for his assistance with the BOLSIG+ solver, and to Kévin Ihaddadene and Jean-Louis Pinçon for their helpful scientific discussions. My special thanks to a good friend Saskia, who assisted me with English language for this manuscript.

My sincere thanks are also extended to Michel Tagger and Dominique Delcourt, the directors of LPC2E, for having allowed me to work in the laboratory. Thank you to Isabelle Langer and Catherine Hong for helping me with laboratory life and managing missions. I would also like to extend my thanks to the technicians, Franck Elie, Antoine Mattei, Paul Postnikoff and Philippe Cacault for providing valuable computer services. Thank you to Lucas Guillemot and Xavier Vallieres for their kind considerations on my PhD study and life.

I would like to sincerely acknowledge all members of the jury, Valéry Catoire, Sébastien Célestin, Nathalie Huret, Franck Lefèvre, Sébastien Payan, Céline Planche, and Serge Soula, for their feedback, insightful comments and suggestions.

I would like to thank all my friends for these past three years, thank you for enriching my life. Thanks go to my colleagues at LPC2E for all the ‘Bon courage’ and uplifting ‘Bonjour’. Thank you to Vanessa for all the chats and for introducing me to sweets, to Charlotte for her assistance in French calls and homemade crêpes. Thanks go to Tjarda for sharing many fun moments and a very memorable trip to Philadelphia, to Saskia for inspiring me in my work and life, and for sharing a good hike in snowy mountains, to Claire for giving me a Python course and teaching me sewing, to French teacher Marta for improving my French and exploring restaurants in Orléans, to Vamsee for helping me in the connections to the lab and the doctoral school. Thanks to my Chinese friends, Rui, Li, Yangang, Hongsheng, Fangfang, Chaolei, Pinpin, Haifei, Min and Vamsee, for their kindness and support in my daily life.

Finally, I wish to thank my parents and my brother for their abiding support and encouragement throughout my studies.

RESUME ETENDU DU MANUSCRIT

La famille des événements lumineux transitoires (TLEs) comprend les jets bleus (BJs), les sprites et les elfes qui se produisent sporadiquement depuis la stratosphère à la mésosphère, de 20 km à 90 km d'altitude. Cette étude porte sur l'étude de l'impact chimique potentiel des BJs qui se développent dans la stratosphère depuis le sommet des nuages d'orages. Ces décharges électriques sont dues à un déséquilibre des charges électriques à l'intérieur des orages [*Krehbiel et al.,* 2008]. Les caractéristiques de ces décharges sont typiquement d'une durée d'environ 200 à 300 ms [*Wescott et al.,* 1996] avec une vitesse verticale ascendante de propagation d'environ 100 km/s. Ces travaux de thèse ont été menés dans le cadre de la mission spatiale TARANIS (Outil d'analyse de la radiation entre la lumière et les sprites) du Centre national d'étude spatiale (CNES) dédiée à l'étude des TLE dont le lancement est prévu en 2020 [*https://taranis.cnes.fr/fr/TARANIS/Fr/GP_mission.htm*].

Les BJ sont constitués d'un ensemble de streamers (« étincelles » se propageant vers le haut et ionisant l'air) rassemblés dans un cône d'angle d'ouverture étroit [*Raizer et al.,* 2006, 2007] initiés depuis le sommet des nuages. Ils ont une structure fractale plasmatique auto-similaire [*Wiesmann et Pietronero,* 1986; *Petrov et Petrova et al.,* 1999; *Pasko et al.,* 2002]. La structure fractale des BJ peut être constituée de streamers positifs [*Pasko et al.,* 1996] ou négatifs [*Sukhorukov et al.,* 1996]. La dimension fractale reste presque constante lorsque les streamers se propagent à différentes altitudes en raison du champ électrique réduit constant dans la tête du streamer [*Popov,* 2002]. Le fort champ électrique près de la pointe du streamer influe sur sa propagation et la forme du champ électrique domine la direction de propagation, la distribution spatiale du champ électrique détermine la probabilité de propagation [*Popov et al.,* 2016].

Les BJ traversent la gamme d'altitude où se situe la couche d'ozone stratosphérique. Les décharges électriques dans l'atmosphère, quelle que soit l'altitude considérée, produisent des oxydes d'azote NO_x (= $NO+NO_2$) en raison du réchauffement intense

et/ou de l'onde de choc dans le canal d'éclairement [*Chameides et al.,* 1987], associée à des réactions de recombinaison et réactions ions-neutres d'oxygène et d'azote atomiques [*Griffing,* 1977; *Kossyi et al.,* 1992]. Des études antérieures ont montré que les TLE devraient avoir un impact significatif sur la concentration de NO_x dans l'atmosphère moyenne [*Neubert et al.,* 2008; *Gordillo-Vazquez,* 2008; *Peterson et al.,* 2009]. Dans la stratosphère, les oxydes d'azote interagissent fortement avec la chimie de l'ozone par le biais de cycles catalytiques [*Johnston,* 1971; *Cohen and Murphy,* 2003] perturbant l'équilibre du système réactif de l'ozone.

Avec un modèle simplifié de chimie plasma, *Mishin* [1997] présente pour la première fois l'impact potentiel des BJ sur la teneur en ozone stratosphérique. Il met en évidence à 30 km d'altitude une augmentation de 10% et 0,5% des teneurs en NO_x et O_3 respectivement. *Smirnova et al.* [2003] étudient l'impact des perturbations du champ électrique sur la basse stratosphère et analysent la perturbation de la composition chimique et de l'ionisation. Les résultats de leurs simulations indiquent que la densité électronique du streamer qui commande le champ électrique à sa tête dépend fortement des réactions chimiques (et leurs coefficients de vitesse) prises en compte. Plus récemment, *Winkler et al.* [2015] (désignés par la suite sous le nom de W2015) ont développé un modèle de chimie-plasma détaillé (comprenant 88 espèces et plus de 1000 réactions) pour étudier l'impact des streamer associés aux BJ sur la chimie de l'ozone. L'augmentation relative des concentrations de NO_x et d'O_3 rapportée par W2015 est beaucoup plus importante que celle des deux études précédentes [*Mishin,* 1997; *Smirnova et al.,* 2003]. Par exemple, à 30 km, l'augmentation des teneurs en oxyde d'azote W2015 est deux fois supérieure à celle de *Mishin* [1997] et de *Smirnova et al.* [2003]. W2015 indique une augmentation relative de 2% des concentrations en O_3 à 30 km, tandis que celles de l'étude de *Smirnova et al.* [2003] n'étaient que de 0,03%, et 0,5% pour *Mishin* [1997]. Les études précédentes citées se concentraient sur les cent premières secondes suivant l'événement de décharge, alors que dans la stratosphère les NO_x interagissent avec la chimie de l'ozone sur une échelle de temps de plusieurs jours en raison des cycles catalytiques.

Dans ce contexte l'objectif des travaux dans cette thèse est de mener une étude détaillée de l'impact potentiel des streamers des BJ sur la chimie stratosphérique via le développement d'un modèle de chimie plasma pour identifier les mécanismes clés associés aux différentes échelles temporelles (millisecondes, centaines de secondes, jours).

Après une revue des connaissances dans le domaine d'étude, le modèle de chimie du plasma développé est présenté ainsi que les paramétrisations permettant de modéliser la décharge du streamer. Puis les caractéristiques des simulations (cas d'étude et initialisation) sont décrites. Le quatrième chapitre est consacré à la validation du modèle par comparaison à l'étude de W2015 ainsi qu'à l'analyse des résultats obtenus en fonction de la paramétrisation considérée pour représenter le streamer :

i) paramétrisation simplifiée avec impulsion électrique simple utilisée dans les études citées.

ii) paramétrisation réaliste développée dans le cadre de ces travaux de thèse avec une impulsion électrique issu d'un modèle électrodynamique.

Ce chapitre se focalise dans la moyenne stratosphère (27 km) au cœur de la couche d'ozone.

Le cinquième chapitre est dédié à l'étude systématique de l'impact de la décharge électrique de BJ sur la perturbation du système chimique en fonction de l'altitude considéré entre 20 km et 50 km d'altitude aux différentes échelles de temps. Enfin les conclusions et perspectives seront présentées.

En résumé cette étude tente d'identifier et d'apporter des pistes de réponse aux questions suivantes :

- Quelles système réactionnel chimie plasma et constantes de réaction associées sont à considérer ? (chapitres 2 et 4)
- Comment représenter la décharge associée au streamer ? (chapitres 2 et 4)

- Quel est l'impact du streamer sur les teneurs en oxyde d'azote et l'ozone en fonction de l'échelle de temps considéré (100 s, 48 h) ? (chapitres 4 et 5)
- Quel est l'impact des décharges électriques associées au BJ sur l'équilibre du système chimique de la stratosphère en fonction de l'altitude considérée ? (chapitre 5)

INTRODUCTION

Transient luminous events (TLEs) are high-altitude lightning flashes and large-scale optical events which last less than one second. TLEs have been documented and characterized above thunderstorms [*Pasko et al.*, 2002] and over most regions of the globe. The TLE family includes blue jets (BJs), sprites and elves which occur above thunderstorm clouds up into the stratosphere and mesosphere (or into the lower ionosphere, from altitudes of 20 km to 100 km). They are directly related to the electrical activity in underlying thunderstorms [*Sentman et al.*, 1995; *Neubert*, 2003; *Pasko*, 2003] and are luminous manifestations of the electrodynamic couplings between the atmospheric layers. The present research was performed in the framework of the TARANIS (Tool for the Analysis of RAdiation from lightNIng and Sprites) space mission dedicated to the observation and study of TLEs.

The ozone (O_3) layer exists in the stratosphere between a height of ~10 km to 50 km with its maximum concentration in the middle stratosphere in the altitude range of 15-35 km above the Earth's surface. The O_3 concentration and thickness also vary with season and latitude, because of the large-scale stratospheric circulation and the chemical production and destruction processes that depend on the latitude/season. The existing stratospheric O_3 layer is an important component of the chemical equilibria of the atmosphere, which plays a key role in modulating the stratospheric vertical temperature gradient, given that O_3 efficiently absorbs solar energy, protecting the biosphere from absorbing harmful ultraviolet (UV) solar radiation (wavelengths shorter than 340 nm). The photochemical production of stratospheric O_3 modulates the solar radiative forcing of climate [*Haigh*, 1994]. Stratospheric ozone thus impacts global climate change through atmospheric radiative budget processes and chemical equilibria.

The altitude range where blue jets occur is located in the stratospheric ozone layer. It is well known that electric discharge in the atmosphere produces NO_x (=NO+NO_2) as a result of intense heating and/or shock waves from lightning channels [*Chameides et*

al., 1987], by recombination reactions and ion-neutral reactions [*Griffing,* 1977; *Kossyi et al.,* 1992] of atomic oxygen and nitrogen. In addition, prior studies showed that TLEs should significantly impact NO_x concentration in the middle atmosphere [*Neubert et al.,* 2008; *Gordillo-Vazquez,* 2008; *Peterson et al.,* 2009]. In the stratosphere, NO_x species interact strongly with ozone chemistry through catalytic cycles [*Johnston,* 1971; *Cohen and Murphy,* 2003] as well as chlorine and bromine species.

Therefore, this study will focus on the potential chemical impact of streamers associated with blue jet (BJ) and gigantic jet (GJ) events, which develop above thunderstorms. BJs and GJs form by the escape of conventional lightning leaders upward from thunderclouds. They mainly occur over oceans near the tropopause located at ~17 km of altitude in the tropics and 13 km of altitude at mid-latitudes. A typical BJ is a slow-moving, fountain-like cone with a cone angle of ~15°, which emanates from the top of thunderclouds up to an altitude of ~ 40-50 km [*Wescott et al.,* 1995, 2001; *Lyons et al.,* 2003] with upward velocities of ~100 km/s. Its light emission duration is ~200-300 ms [*Wescott et al.,* 1996]. Due to a set of blue and near-ultraviolet emission lines from neutral and ionized molecular nitrogen, BJs have a visual color of blue [*Wescott et al.,* 1995, 1998, 2001].

Upward streamers of BJs produce a narrow cone confined by an aperture angle of ~15º [*Raizer et al.,* 2006, 2007]. Thus, BJs are similar to streamer coronas, where the discharge is a self-similar plasma fractal structure [*Wiesmann and Pietronero,* 1986; *Petrov and Petrova,* 1999; *Pasko et al.,* 2002]. The BJ fractal structure can comprise positive [*Pasko et al.,* 1996] or negative [*Sukhorukov et al.,* 1996] streamers. The fractal dimension remains almost constant when streamers propagate at different altitudes because of the constant reduced electric field in the streamer head [*Popov,* 2002]. The strong electric field near the streamer tip impacts the streamer propagation. The shape of the electric field dominates the propagation direction, while the spatial distribution of the electric field determines the propagation probability [*Popov et al.,* 2016].

There are, however, few investigations on the chemistry of BJs. With a simplified plasma chemistry model, *Mishin* [1997] reported an impact of BJ streamer discharge. He highlighted that nitric oxide and ozone concentrations increased by 10 and 0.5%, respectively, at an altitude of 30 km. *Smirnova et al.* [2003] updated the chemical composition and ionization and attachment rates to study the impact of electric field perturbations on the lower stratosphere. Their simulation results indicated the importance of reactions and their rate coefficients in BJ streamer electron density governed processes (electric field driven processes). More recently, *Winkler et al.* [2015] (referred to as W2015 hereafter) developed a detailed plasma chemistry model (including 88 species and more than 1000 chemical reactions) to investigate the impact of BJ streamers and leaders during the first 100 s after the discharge. For the impact of BJ streamers, the relative increases in NO_x and O_3 reported by W2015 are significantly larger than those reported by the previous two studies. For instance, at 30 km, the NO_x increase in the W2015 model is two orders of magnitude larger than it is in the model of *Mishin* [1997] and *Smirnova et al.* [2003]. W2015 indicated a relative O_3 increase of 2% at 30 km, while *Smirnova et al.* [2003] and *Mishin* [1997] inferred an O_3 increase of 0.03% and 0.5%, respectively. For the impact of BJ leaders, W2015 signified a strong loss of O_3 at altitudes below 27 km. The density of O_3 decreased to ~5 orders of magnitude smaller than the pre-leader case when the altitude decreased to 18 km. A study by *Perez-Invernon et al.* [2019] estimated the global chemical influence of BJs, considering the occurrence rate at a global scale using the Whole Atmosphere Community Climate Model (WACCM4). They used the local chemical impact of W2015 for a single BJ (including BJ streamer and leader) and assumed that the total productions of N_2O and NO at 30 km are dominated by the leader phase. The global scale chemical impact indicated that BJs decrease O_3 at 30 km by up to a maximum of ~5% in equatorial and polar regions.

While the model of W2015 considered the presence of chlorine family species (Cl_y), it did not consider the presence of bromine family species (Br_y), which also significantly contribute to O_3 destruction, particularly in the stratosphere [*Yung et al.*,

1980; *Prather et al.*, 1990]. All previous studies that have investigated the chemical effects of BJ events have moreover focused on the first hundred seconds after the discharge event, whereas NO_x species production in the stratosphere interacts with ozone chemistry on a timescale of several days.

Previous modeling studies assumed a constant pulse electric field to represent the discharge associated with BJs and sprite streamers [e.g. *Winkler et al.*, 2014, 2015; *Gordillo-Vázquez*, 2008; *Sentman et al.*, 2008], while it is well-known from electrodynamic streamer models [*Ihaddadene and Celestin*, 2017] that the electric field of streamers varies as a function of time during the discharge process.

The first part introduces the stratosphere environment focussing on ozone and the associated chemistry (production and destruction mechanisms). Then it describes the physical characteristics of transient luminous events with a specific focus on BJs and the plasma chemistry processes associated with electric discharge.

In the second part, the model developed to study the potential impact of BJ streamer on stratospheric chemistry is presented. The detailed chemistry-plasma model is named Microphysical and Photochemical Ozone and Streamer (hereafter MiPO-Streamer) model. The model considers 117 chemical species and 1760 chemical reactions including photochemistry, neutral chemistry, heterogeneous chemistry and plasma chemistry. The rate coefficients of electric-driven reactions were calculated using the BOLSIG+ solver. The parameterization of electric-driven processes to represent the BJ streamer discharge processes is then described.

The third part describes the case study in detail and the initialization of the model.

The fourth part focuses on the simulations at 27 km of altitude (in the ozone layer) where the catalytic cycle of NO_x is the most efficient to destroy ozone. The model validation results on neutral chemistry and plasma chemistry by comparing with the study of W2015 are presented. Compared to the simple pulse electric field generally used, the streamer parameterization of a time-dependent field derived from an explicit electrodynamic streamer model is investigated. Most of the results presented here

correspond to a paper submitted to the Journal of Geophysical Research [*Xu et al.*, 2019].

The fifth part is dedicated to the analysis of the BJ streamer chemical impacts in the stratosphere (from 20 km to 50 km). Detailed investigations as a function of altitude are conducted to highlight the major pathways of plasma chemistry and neutral chemistry, and their interactions on ozone abundance.

The last part presents concluding remarks and future work.

CHAPTER I

STRATOSPHERIC OZONE AND TRANSIENT LUMINOUS EFFECTS

Contents

Cette partie présente de manière générale la chimie de l'ozone stratosphérique et les mécanismes de production et de destruction associés (Section 1.1). Puis les événements lumineux transitoires sont décrits ainsi que les propriétés physiques spécifiques des Blue Jets et les mécanismes chimiques associés aux décharges électriques (Section 1.2). Les différents processus de chimie plasma au cours de la décharge que nous considèrerons dans cette étude sont décrits (Section 1.3).

Enfin les principales questions et objectifs scientifiques de ces travaux seront exposés (Section 1.4).

This study discusses the potential impact of blue jet streamers on stratospheric chemistry, especially on the ozone layer. This chapter will first show the distribution and importance of stratospheric ozone, and it will then introduce the associated chemistry of ozone production and destruction in Section 1.1. Secondly, a description of transient luminous events and their potential impacts on stratospheric chemistry are given in Section 1.2 with specific details on the physical properties and chemical impacts of blue jet events. Section 1.3 introduces the plasma chemistry processes associated with transient luminous events which will be considered in this study. Lastly, Section 1.4 presents the objectives of this study and the questions which will be answered by this study.

1.1 Stratosphere and ozone layer

1.1.1 Stratospheric ozone

The stratosphere is part of the Earth's atmosphere at altitudes between ~ 12 km and 50 km at mid-latitudes, where temperature increases with altitude, as shown in Figure 1-1, shaded in grey. The green line in Figure 1-1 outlines the ozone (O_3) layer, i.e. its concentration as a global mean distribution. The maximum ozone concentration occurs in the low and middle stratosphere between altitudes of ~15 km to 35 km above the Earth's surface. The O_3 concentration and thickness vary with season and with latitude.

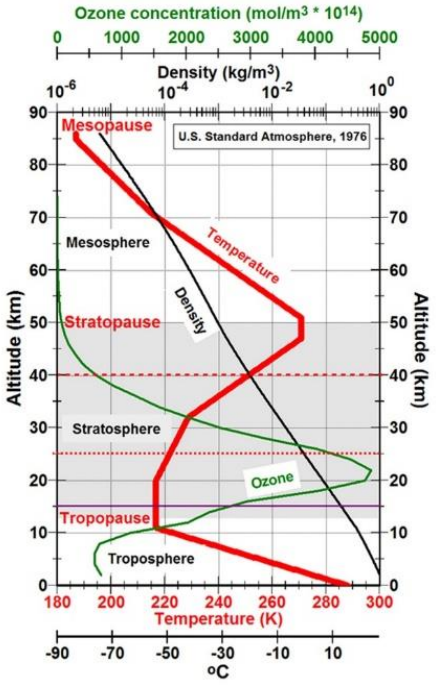

Figure 1-1. Temperature (red), density (black), and ozone concentration (green) as a function of altitude (km) for the U.S. Standard Atmosphere (1976) at mid-latitude. Ozone data are from *Krueger and Minzner* [1976].

The existing stratospheric O_3 layer is an important component of the chemical equilibrium of the atmosphere. The stratospheric vertical temperature gradient is caused by O_3 absorption of solar energy. It is well known that O_3 protects the biosphere from absorbing harmful ultraviolet (UV) solar radiation (i.e. radiation with wavelengths shorter than 340 nm). *Haigh* [1994] showed that the photochemical production of stratospheric O_3 modulates the solar radiative forcing of climate. The stratospheric ozone layer thus impacts global climate change, as it affects atmospheric radiative budget processes and chemical equilibria.

The cycle of stratospheric O_3 is governed by photochemistry and chemical reactions associated with nitrogen and oxygen. The processes associated with the stratospheric ozone abundance are shown in Figure 1-2. Stratospheric O_3 is impacted by stratospheric chemical processes and by temperature, polar stratospheric clouds, aerosols and greenhouse gases. During the last decades, the natural balance of chemical compounds in the stratosphere has been disturbed. Ozone depletion is caused by human emissions of ODSs (Ozone-Depleting Substances). ODSs include chlorofluorocarbons (CFCs),

bromine, hydrochlorofluorocarbons (HCFCs), carbon tetrachloride (CCl_4), and methyl chloroform. The emission of these species leads to the release of reactive halogen gases, especially chlorine and bromine, which destroy ozone. Since the Montreal Protocol in 1985 emissions are controlled and chlorine and bromine are declining in the atmosphere.

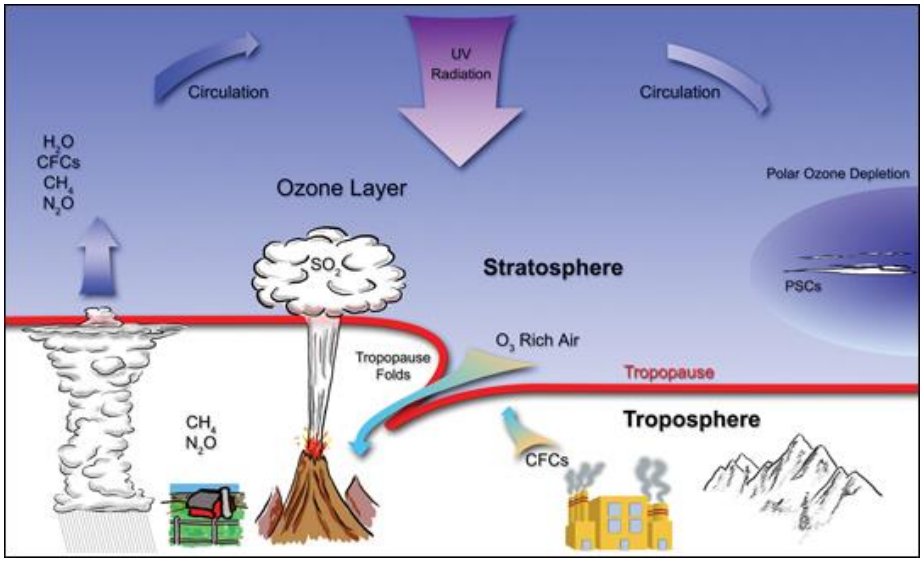

Figure 1-2. Natural and anthropogenic mechanisms associated with the stratospheric ozone layer. Credit from Barbara Summey, SSAI.

However, the ozone equilibrium is complex. The increased concentrations of greenhouse gases, e.g. CO_2, H_2O, and methane (CH_4), warm the tropopause and cool the stratosphere, thus diminish ozone depletion [*Shindell et al.,* 1998; *Austin et al.*, 1992; *Daniel et al.,* 1999]. In addition to directly modifying stratospheric temperature, by-products of chlorofluorocarbons (CFCs) and nitrous oxide (N_2O) also cause O_3 destruction, including reactions between O_3 and nitrogen dioxide (NO_2) or chlorine monoxide (ClO). Volcanic clouds and polar stratospheric clouds (PSC) can indirectly contribute to O_3 loss by accelerating heterogeneous chemical reactions on the surface of aerosols and clouds [e.g. *Pitari et al.*, 2002]. The $ClONO_2$ and N_2O_5 components involved suppress active NO_x to lower levels, and as a result of that, halogens cause more severe O_3 destruction at mid-altitude [*Prather,* 1992; *Solomon,* 1999].

Many models and observations have assessed the influence of stratospheric O_3 changes at global scale. O_3 depletion in the stratosphere cools the stratospheric temperature [*Langematz,* 2000], which impacts the tropopause altitude. It leads to more UV radiation reaching the troposphere and the Earth's surface. The cooling stratosphere could lead to increased PSC formation and more complete chemical processes [*Lee et al.,* 2001]. *Prather and Jaffe* [1990] demonstrated that the chemical propagation of the Antarctic ozone hole also destroys ozone at mid-latitudes. Increased UV radiation at the Earth's surface affects human and ecosystem health, e.g. increasing the risk of skin tumors and eye diseases. The modification of UV radiation in the troposphere also impacts on troposphere chemistry. For instance, *Bekki et al.* [1994] found through a model simulation that decreases in CH_4 and CO concentrations in the troposphere are impacted by increased UV radiation, which increases the production of hydroxyl radicals (OH).

Concerning ozone recovery, the WMO (World Meteorological Organization) ozone assessments [2014 and 2018] reported:

The decline of stratospheric ozone has been stopped in the late 1990s. Since about 2000, ozone levels in most parts of the stratosphere have remained approximately constant or have been increasing slightly. About half of the ozone increase is due to declining ozone-depleting substances (ODSs, declining due to the Montreal Protocol). The other half is due to cooling of the stratosphere due to carbon dioxide (CO_2) increases, which slows chemical ozone destruction cycles in the upper stratosphere. Not only ozone-depleting substances, but also increasing greenhouse gases affect the ozone layer.

A small acceleration of the global stratospheric Brewer-Dobson circulation (BDC) over the next century is expected from model simulations. Acceleration of the BDC will reduce ozone in the tropics and enhance ozone at higher latitudes.

In the second half of the century, ozone columns may even exceed historical levels.

Model simulations have confirmed that not only ODSs and CO_2, but also future levels of nitrous oxide (N_2O) and methane (CH_4) will play a significant role in the recovery of stratospheric ozone over this century. By itself, increasing N_2O will increase ozone loss. This would delay and negate part of the expected ozone recovery (due to declining ODSs and stratospheric cooling). Increasing methane, on the other hand, will generally increase ozone levels by tying up chlorine and by enhancing ozone production in the lower stratosphere. In the second half of the century, lower chlorine levels, stratospheric cooling, and other factors will reduce the efficiency by which CH_4 and N_2O emissions affect ozone.

1.1.2 Stratospheric ozone chemistry

Figure 1-3 shows the vertical distribution of major gas constituents (long lived species) in the atmosphere, including N_2, O_2, CO_2, H_2O, CH_4, N_2O, and O_3. Except for ozone with a maximum concentration in the stratosphere, the concentrations of the other constituents decrease with pressure (Figure 1-3a). The volume mixing ratios (VMRs) of N_2, O_2, N_2, CO_2 are constant as a function of altitude, whereas the VMRs of CH_4, N_2O and CFCs are constant in the troposphere, and those in the stratosphere are decreased (Figure 1-3b).

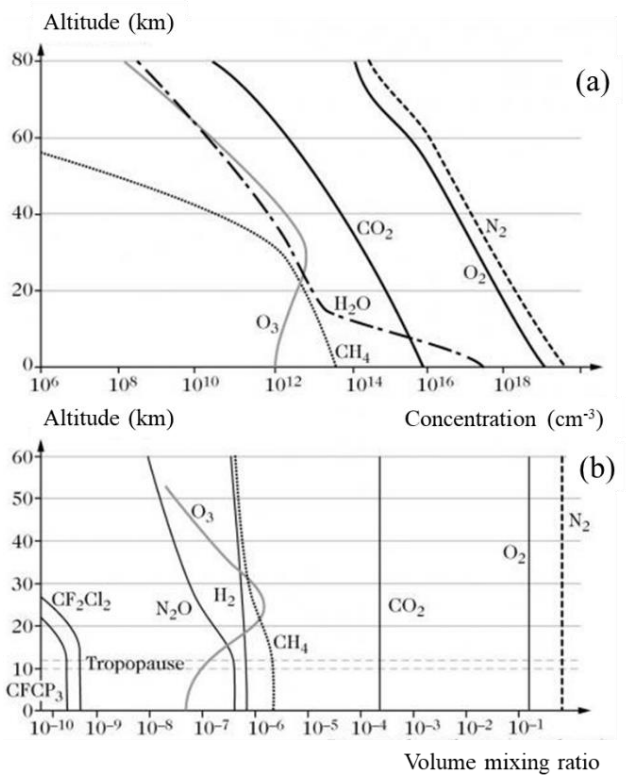

Figure 1-3. Vertical distribution of major gas constituents in the atmosphere by (a) number of molecules per cm^3 (absolute concentrations) and (b) volume mixing ratio (relative concentrations).

Credit from: *http://omer7.sedoo.fr/mallette/fiches/Distribution-des-polluants-echelles-de-la-pollution-atmospherique*

1.1.2.1 Ozone chemistry

The chemical mechanism of stratosphere ozone photochemistry was first described by *Chapman* [1930]. The ground state of oxygen atoms is first produced by the photolysis of O_2:

$$O_2 + h\nu \rightarrow O + O \qquad (\lambda < 240\ \text{nm}) \quad (1\text{-}1)$$

a reaction that requires a significant amount of energy. Ozone is then rapidly produced, recombining with free oxygen atoms and a large excess of O_2 through the reaction:

$$O_2 + O \xrightarrow{M} O_3 \qquad (1\text{-}2)$$

where M is any third-body molecule, e.g. N_2 or O_2. Following reaction (1-2), the interconversion of O and O_3 is fast via:

$$O_3 + h\nu \rightarrow O_2 + O(^1D) \quad (\lambda < 320 \text{ nm}) \quad (1\text{-}3)$$

$$O(^1D) \xrightarrow{M} O \quad (1\text{-}4)$$

$$\text{Net:} \quad O_3 + h\nu \rightarrow O_2 + O \quad (1\text{-}5)$$

The odd-oxygen family is defined as $O_x = O + O_3$. O_x is slowly destroyed through:

$$O_3 + O \rightarrow O_2 + O_2 \quad (1\text{-}6)$$

with a minor contribution through:

$$O + O \xrightarrow{M} O_2 \quad (1\text{-}7)$$

Reactions (1-2) and (1-5), which cycle between O and O_3, are much faster than reactions (1-1) and (1-6), which create and destroy O_x. The O_3 balance is determined mainly by the total sum of O_x. O_3 has a long photochemical lifetime in the lower stratosphere, thus photochemistry is important for O_3 production in the stratosphere, particularly in the tropics [*Avallone et al.*, 1996].

1.1.2.2 Ozone catalytic cycles

Besides the Chapman cycle, stratospheric O_3 is particularly perturbed through catalytic cycles [*Murphy et al.*, 1993]. Most O_3 is destroyed through potent catalytic cycles associated with gaseous nitrogen oxide [*Crutzen*, 1970; *Johnston*, 1971], hydrogen oxide [*Bates and Nicolet*, 1950] and chlorine radicals [*Molina and Rowland*, 1974; *Stolarski and Cicerone*, 1974] of the type:

$$O_3 + X \rightarrow O_2 + XO \quad (1\text{-}8)$$

$$O + XO \rightarrow O_2 + X \quad (1\text{-}9)$$

$$\text{Net:} \quad O_3 + O \rightarrow 2O_2 \quad (1\text{-}10)$$

with X = NO, OH, Cl. The catalyst X is neither created nor destroyed through the reactions. Therefore, the recycling of X molecules continues to destroy ozone until it converts to a less-reactive species. The catalytic cycle rate mostly depends on the catalyst concentrations.

There are two catalytic cycles involving halogenated compounds, which are particularly effective catalytic compounds in the Antarctic lower stratosphere. The first one comprises chlorinated species (odd-chlorine catalytic cycle):

$$2 \times (Cl + O_3 \rightarrow ClO + O_2) \qquad (1\text{-}11)$$

$$ClO + ClO \xrightarrow{M} Cl_2O_2 \qquad (1\text{-}12)$$

$$Cl_2O_2 \xrightarrow{h\nu} Cl + ClOO \qquad (1\text{-}13)$$

$$ClOO \xrightarrow{M} Cl + O_2 \qquad (1\text{-}14)$$

$$\text{Net:} \quad 2O_3 \rightarrow 3O_2 \qquad (1\text{-}15)$$

The second one comprises both chlorinated and brominated compounds (Cl-Br catalytic cycle, *McElroy et al.*, 1986):

$$BrO + ClO \rightarrow Cl + Br + O_2 \qquad (1\text{-}16a)$$

$$Br + O_3 \rightarrow BrO + O_2 \qquad (1\text{-}17)$$

$$Cl + O_3 \rightarrow ClO + O_2 \qquad (1\text{-}18)$$

$$\text{Net:} \quad 2O_3 \rightarrow 3O_2 \qquad (1\text{-}19)$$

The activation energy of light is essential for these two cycles. Furthermore, there are two other possible reactions between BrO and ClO:

$$BrO + ClO \rightarrow BrCl + O_2 \qquad (1\text{-}16b)$$

$$BrO + ClO \rightarrow OClO + Br \qquad (1\text{-}16c)$$

BrO and ClO rapidly react to BrCl overnight and the ozone destruction cycle thus stops. However, with the beginning of daylight, the rapid photo-dissociation of BrCl re-initiates the cycle through:

$$BrCl \xrightarrow{h\nu} Br + Cl \qquad (1\text{-}20)$$

Salawitch [1993] and *Anderson et al.* [1989] revealed that the odd-chlorine catalytic cycle contributes up to 70% of the ozone destruction observed, while the Cl-Br catalytic cycle contributes ~23%. Because inorganic, brominated compounds are ~150 times less abundant than inorganic chlorinated compounds in the stratosphere [*Harder et al.*, 2000], the Cl-Br catalytic cycle has a more severe contribution to stratospheric ozone destruction.

The left panel of Figure 1-4 shows the relative global annual mean ozone loss rates by chemical family, namely NO_x, O_x, HO_x, ClO_x/BrO_x, computed for the year 2000 by the NOCAR two-dimensional model [*Portmann et al.*, 2012]. Between the altitudes of 10 km to 18 km, the HO_x cycle is more efficient than the cycles of the other chemical families. The O_3 loss rate of the ClO_x/BrO_x cycle is larger than that of the NO_x cycle. Between the altitudes of 18 km to 22 km, O_3 loss is governed first by HO_x and second by the NO_x cycle. The NO_x cycle represents a major sink for O_3 in the middle stratosphere (from 22 km to 43 km). It is evident that the HO_x cycle is dominant in the upper stratosphere (higher than 43 km).

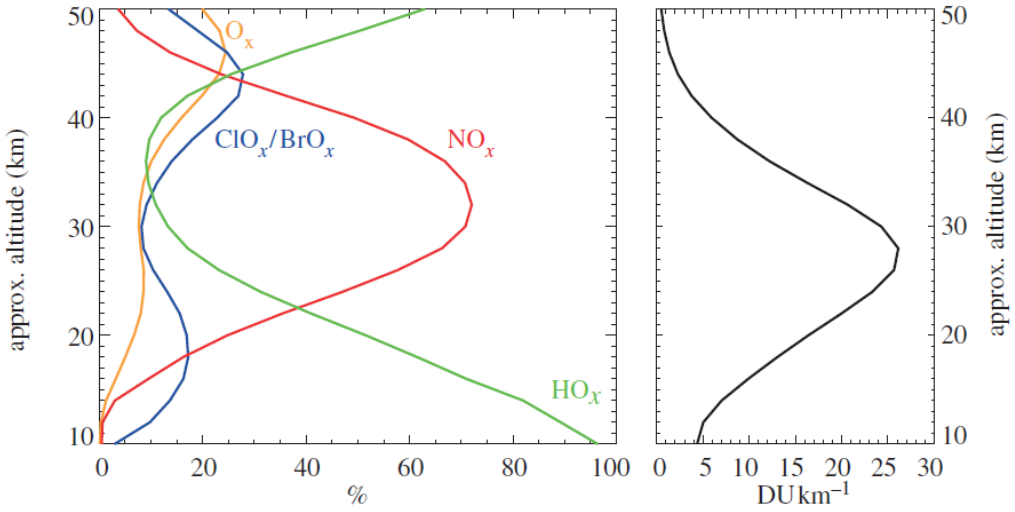

Figure 1-4. The relative global annual mean ozone loss rates by chemical family computed for the year 2000 by the NOCAR two-dimensional model (left). The global mean ozone profile (right). From *Portmann et al.* [2012].

The right panel of Figure 1-4 shows the maximum O_3 in the middle stratosphere. Since the O_3 loss rate through the NO_x cycle is the largest in the altitude of abundant O_3, NO_x concentrations are an important factor in ozone layer perturbation.

Nitrogen oxides are well known to have a crucial effect on O_3 loss, and also on the Cl_y and Br_y species [*Yung et al.*, 1980; *Prather et al.*, 1990]. Cl_y and Br_y species effectively destroy stratospheric ozone by several catalytic cycles which vary with latitude and altitude [*WMO*, 1995]. Compared to chlorine, bromine is ~45 times more effective in destroying global stratospheric ozone [*Daniel et al.*, 1999]. BrO is the major bromine species throughout the stratosphere, while the combined ClO/BrO cycles are dominant in the upper and lower stratosphere (Figure 1-4). Cl_y and Br_y chemistry thus cannot be neglected when characterizing and quantifying O_3 loss.

1.1.3 Chemistry of nitrogen

NO_x comprises nitrogen monoxide (NO) and nitrogen dioxide (NO_2). These two compounds are more abundant in day-time than at night-time. At night, NO is converted to NO_2 with ozone by the reaction:

$$NO + O_3 \rightarrow NO_2 + O_2 \qquad (1\text{-}21)$$

and NO_x is entirely in the form of NO_2. The abundance of NO_2 increases at night within altitudes of up to ~30 km.

At night, NO_x is preserved as N_2O_5 by the reaction:

$$NO_2 + NO_3 \xrightarrow{M} N_2O_5 \qquad (1\text{-}22)$$

where M is any third-body molecule, e.g. N_2 or O_2, whose density decreases with increasing altitude. Thus, more NO_2 is transformed to N_2O_5 at nighttime and at low stratosphere levels than at high stratosphere levels. The main sources for NO_x from the decay of N_2O_5 are produced by inverse thermal decomposition reactions:

$$N_2O_5 \xrightarrow{M} NO_2 + NO_3 \qquad (1\text{-}23)$$

which are more effective when the temperature is high, and by photo-dissociation reactions:

$$N_2O_5 \xrightarrow{h\nu} NO_2 + NO_3 \qquad (1\text{-}24)$$

As the temperature increases with increased altitude in the stratosphere, and the available light energy for a photo-dissociate molecule is higher in the upper stratosphere than in the lower stratosphere, the reaction rates of (1-23) and (1-24) are larger in the upper stratosphere. Therefore, N_2O_5 is consumed faster after sunrise in the upper stratosphere.

The primary production of reactive nitrogen NO_x in the lower and middle stratosphere comes from reactions with nitrous oxide (N_2O). First, N_2O is broken down via photolysis:

$$N_2O + h\nu \rightarrow N_2 + O(^1D) \qquad (1\text{-}25)$$

Then NO is produced via reaction with N_2O and $O(^1D)$:

$$N_2O + O(^1D) \rightarrow 2NO \qquad (1\text{-}26)$$

N_2O and $O(^1D)$ also produce N_2 and O_2:

$$N_2O + O(^1D) \rightarrow N_2 + O_2 \qquad (1\text{-}27)$$

where ~10% of N_2O can be converted to NO_x in the stratosphere [*Portmann et al.*, 2012]. Reactive nitrogen can be destroyed via the reaction:

$$N + NO \rightarrow N_2 + O \qquad (1\text{-}28)$$

N_2O can produce reactive nitrogen and then affect all of the chemical families, e.g. ClO_x and BrO_x via the formation of $ClONO_2$ and $BrONO_2$, ozone loss and so on. Moreover, the global lifetime of N_2O is as long as 114 years [*IPCC*, 2007] and it thus

has a long-term effect. Therefore, the perturbation of N_2O in the atmosphere is important for chemical cycles.

1.2 Transient Luminous Events (TLEs)

The TLE family includes high-altitude lightning flashes and large-scale optical events that last for less than a second (Figure 1-5). Although eyewitness reports of TLEs above thunderstorms have been recorded for more than a century, the first image of one was captured only in 1989, serendipitously during a test of a low-light television camera [*Franz et al.,* 1990]. Since then, many transient luminous events (TLEs) have been documented and classified above thunderstorms [*Pasko et al.,* 2002] from the ground [e.g. *Winckler et al.,* 1993; *Lyons,* 1994], from aircraft [e.g. *Sentman and Wescott,* 1993; *Wescott et al.,* 1995], from the space shuttle [e.g. *Boeck et al.,* 1992] and from orbiting sensors [e.g. *Neubert et al.,* 2001; *Chern et al.,* 2003; *Chen et al.,* 2008]. All of them show that TLEs appear over most regions of the globe.

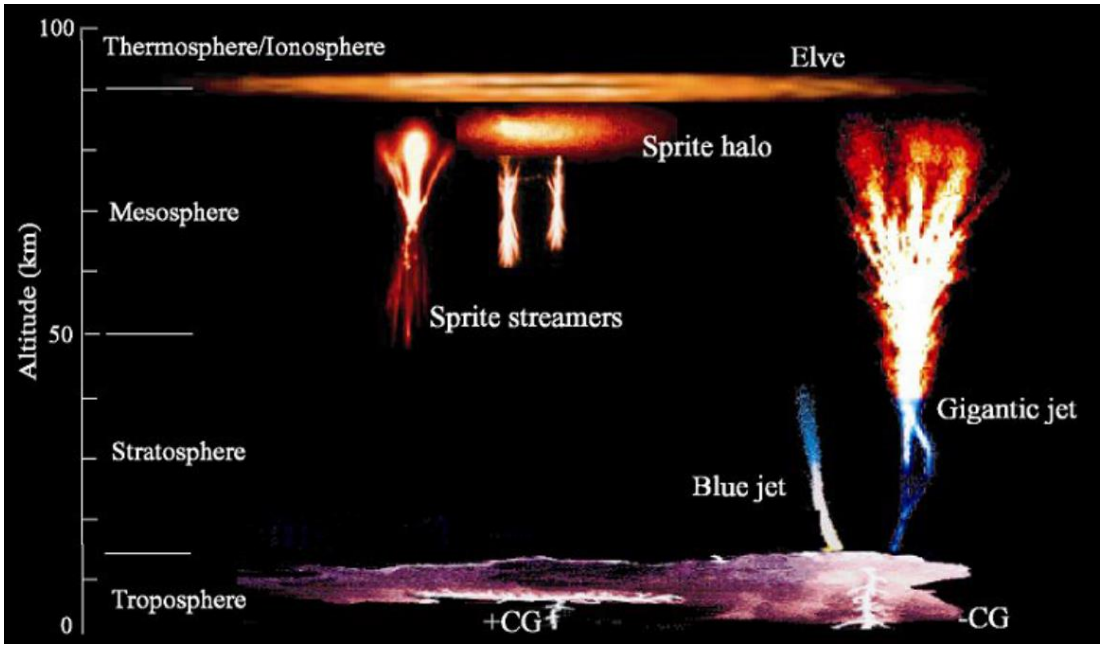

Figure 1-5. The distribution of transient luminous events in the atmosphere. Credit from: CNES. *https://taranis.cnes.fr/fr/TARANIS/Fr/GP_mission.htm*

They occur above thunderstorm clouds up to the mesosphere (or lower ionosphere). They are directly related to the electrical activity in the underlying thunderstorms [*Sentman et al.,* 1995; *Neubert,* 2003; *Pasko,* 2003] and they are luminous manifestations of the electrodynamic couplings between the atmospheric layers.

Sprites develop at the base of the ionosphere and move rapidly downwards at speeds of up to 10000 km/s. They appear in the altitude range of ~40 km to 90 km above large thunderstorms [*Sentman et al.,* 1995; *Boccippio et al.,* 1995; *Lyons,* 1996; *Stanley et al.,* 1999]. The first image of a sprite was captured by scientists from the University of Minnesota in 1989. Sprites generally appear in clusters of three or more and they can cover horizontal distances of ~50 km. They are reddish-orange in color and they have various shapes, i.e. carrot-, angel- or column-like shapes with hanging tendrils below. Sprites usually occur at altitudes of ~65 km to 75 km and their tendrils can extend down to altitudes as low as 40 km. Sprites are associated with powerful positive cloud-to-ground lightning [*Barrington-Leigh et al.,* 1999; *Bell et al.,* 1998]. The electromagnetic pulse (EMP) is generated above the thunderstorm cloud during an intense lightning discharge. The resulting intense electric field above the clouds can extend over a large altitude range to the upper atmosphere and is possibly responsible for atmospheric air breakdown or runaway electron ionization [*Pasko et al.,* 1995, 1996; *Bell et al.,* 1995]. Ionization and optical emissions that occur are manifested in the form of the visible Sprite.

Elves are lightning induced TLEs, occurring at high altitude above large and intense lightning strikes in a thunderstorm. They were first identified in 1990 in space shuttle images. Their ring-like shapes are different from sprites. They can spread over 100-300 km laterally, occurring in the lower ionosphere [*Fukunishi et al.,* 1996; *Inan et al.,* 1997]. Similar to sprites, elves are likely caused by heated lower ionospheric electrons by EMPs [*Inan et al.,* 1991; *Taranenko et al.,* 1995].

Jets include gigantic jets (GJs) (e.g. Figure 1-6a), blue jets (BJs) (e.g. Figure 1-6b) and blue starters. All jets emanate from the top of thunderclouds (~15-18 km), and they are differentiated by their terminal altitudes. GJs propagate upwards towards Earth's

ionosphere to an altitude of ~90 km [*Su et al.,* 2003], BJs up to 40 km with moving speeds of ~100 km/s [*Wescott et al.,* 1995, 1998, 2001; *Lyons et al.,* 2003], while blue starters rise to a maximum altitude of ~25.5 km [*Wescott et al.,* 1996, 2001]. Blue starters are considered as the initial stages of blue jets. As shown in Figure 1-6, GJs present a visible blue color in the lower channel, like BJs, and a red color with a streamer-like structure above 40 km.

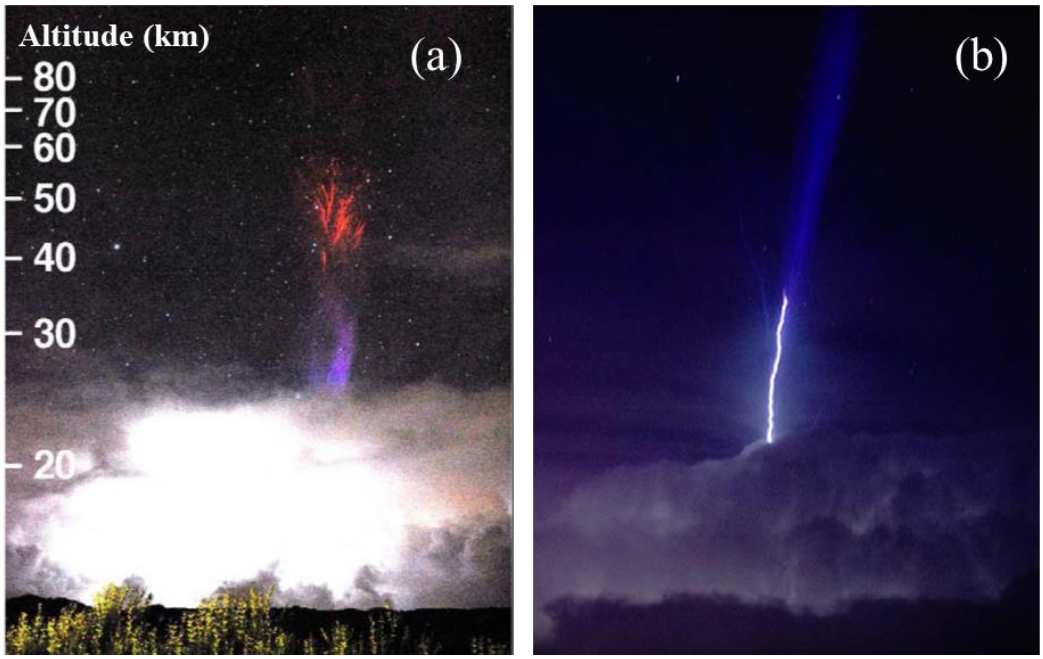

Figure 1-6. Color photographs of (a) gigantic jets, captured by Patrice Huet on 7th March 2010 [*Soula et al.*, 2011], and (b) blue jet captured by William Nguyen Phuoc on 8th December 2015.

1.2.1 Physical characteristics of jets

BJs and GJs form by the escape of conventional lightning leaders upward from thunderclouds. They are types of upper-atmospheric lightning and of cloud-to-air discharge within a thunderstorm, propagating upwards. They mainly occur over ocean [e.g. *Chen et al.,* 2008] and in the tropics (tropopause ~17 km) and at mid-latitudes (~15 km). A typical BJ is a slow-moving, fountain-like cone with a cone angle of ~15°, which emanates from the top of thunderclouds up to an altitude of ~ 40-50 km [*Wescott et al.,*

1995, 2001; *Lyons et al.*, 2003], moving with an upward velocity of ~100 km/s. Its light emission duration is ~200-300 milliseconds [*Wescott et al.*, 1996]. Due to a set of blue and near-ultraviolet emission lines from neutral and ionized molecular nitrogen, BJs are blue in color [*Wescott et al.*, 1995, 1998, 2001].

The structure and apparent speed of a jet vary significantly during its lifetime [*Pasko et al.*, 2002 (P2002); *Su et al.*, 2003]. The evolution of a jet is characterized by three main stages, i.e. formation of the leading jet, fully developed jet, and trailing jet. In a GJ event captured by P2002 (Figure1-7), the leading jet (stage A) grew at the beginning with an average speed of ~60 km/s, increasing to a speed of up to ~200 km/s (#11–12), and then decelerating (#12–13) and again brightening and accelerating to ~500 km/s (#13–14). Then, the tip propagated at ~500 km/s to ~48 km and ejected fully developed jets (stage B), which moved at ~1200 km/s. Meanwhile, bright diffuse spots appeared at a height of ~ 70 km. At the end of the event, the top of the trailing jet (stage C) faded away and its forked structure persisted at a height of ≤ 32 km.

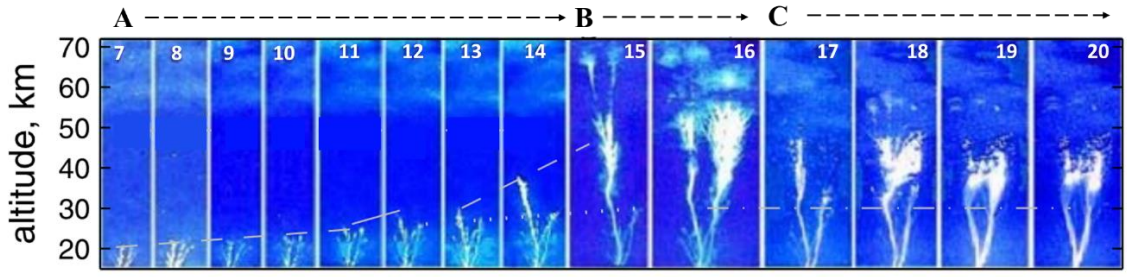

Figure 1-7. Video fields 7-20 (~17 ms each) during the 15 Sep 2001 GJ event that occurred ~200 km northwest of Arecibo Observatory, Puerto Rico. Credit from *Mishin and Milikh* [2008]

BJ and GJ events differ in their maximum altitude and their polarities [*Krehbiel et al.*, 2008]. As shown in Figure 1-8, BJs develop up to a lower altitude than GJs. Studies found that BJs are generated by electrical breakdown between upper storm charges and the cloud top screening charge. GJs initiate as an in-cloud discharge between a mid-level dominant charge and an upper-level screening charge, and then propagate out of the storm top. From normal polarity thunderclouds (Figures 1-8a and 1-8b), BJs

transport a positive charge upward, while GJs transport a negative charge upward. On inverted polarity storms (Figures 1-8c and 1-8d), BJs produce a negative charge upward, while GJs produce a positive charge upward. The mechanism that produces the jets is similar to cloud-to-ground lightning, which causes a charge imbalance in the storm.

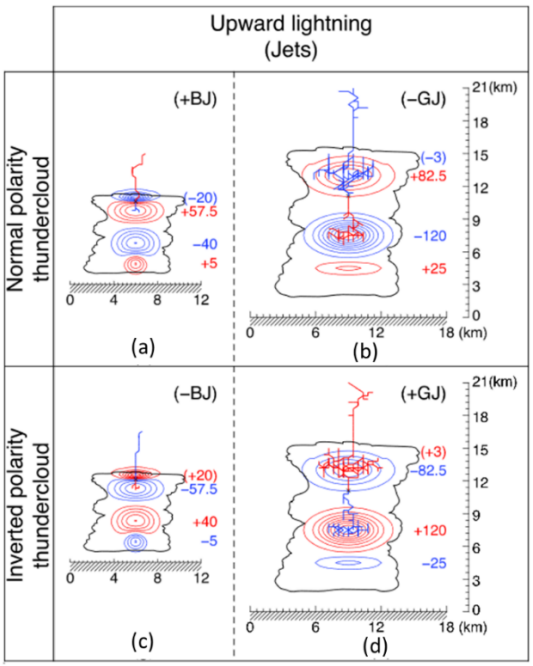

Figure 1-8. BJ and GJ simulation for normal- and inverted-polarity storms. Modified from *Krehbiel et al.* [2008].

Figure 1-9a shows the structure of BJs, which includes a tall tree with a thin trunk (called 'leader') and branches above (called 'streamer'). The numerical model of *Raizer et al.* [2006, 2007] demonstrated that, firstly, the leader is caused in the bending point after the largest electric field of the cloud charge appears, as described in Figure 1-9b. Then it moves upward and transfers the high electron potential energy outside the cloud top. BJ leaders emit streamers and streamers grow preferentially upward in the atmosphere. Thus, the streamers are formed as the corona.

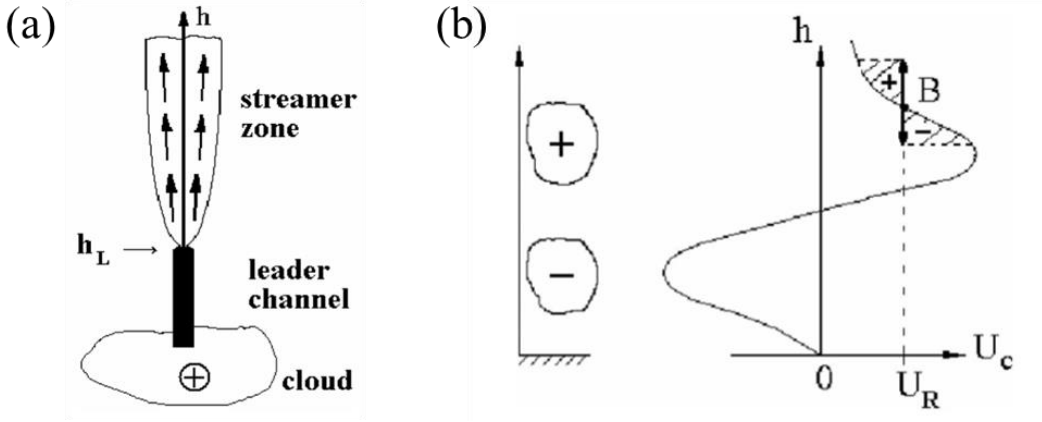

Figure 1-9. (a) A schematic of the bi-leader initiation in a thundercloud. (b) A schematic blue jet model. [*Raizer et al.*, 2007, 2010]

1.2.2 Chemistry associated with TLEs

It is well known that electric discharge in the middle atmosphere produces NO_x (=NO+NO_2) as a result of intense heating and /or shock wave from a lightning channel [*Chameides et al.*, 1987], by recombination reactions and ion-neutral reactions [*Griffing*, 1977; *Kossyi et al.*, 1992] of atomic oxygen and nitrogen. Thus, the lightning produces nitrogen oxides. The production of NO_x in TLEs has the same reaction steps as in tropospheric discharges [*Hiraki*, 2004]. The discharge generates an electric field which drives electron impact on air molecules and atoms by ionization, dissociation and excitation processes. *Goldenbaum and Dickerson* [1993] proposed that NO_x formation in thunderstorm discharges starts with the dissociation of oxygen and nitrogen molecules through:

$$e^- + N_2 \rightarrow N + N + e^- \qquad (1\text{-}29)$$

$$e^- + O_2 \rightarrow O + O + e^- \qquad (1\text{-}30)$$

NO is then produced by the single replacement of an oxygen or nitrogen atom with nitrogen or oxygen molecules:

$$N_2 + O \rightarrow NO + N \qquad (1\text{-}31)$$

$$O_2 + N \rightarrow NO + O \qquad (1\text{-}32)$$

Finally, the reaction ends with a recombination of nitrogen and oxygen atoms:

$$N + N \rightarrow N_2 \qquad (1\text{-}33)$$

$$O + O \rightarrow O_2 \qquad (1\text{-}34)$$

For N_2 and O_2, which are common air constituents, the principal ionization reactions are:

$$e^- + N_2 \rightarrow N_2^+ + 2e^- \qquad (1\text{-}35)$$

$$e^- + N_2 \rightarrow N^+ + N + 2e^- \qquad (1\text{-}36)$$

$$e^- + O_2 \rightarrow O_2^+ + 2e^- \qquad (1\text{-}37)$$

$$e^- + O_2 \rightarrow O^+ + O + 2e^- \qquad (1\text{-}38)$$

The oxygen and nitrogen atoms that are produced in these reactions can be in their ground states or in excited states. An example for O_2 is schematically shown in Figure 1-10. The excitation of N_2 or O_2 is caused by electron collisions, which produce electronically excited N_2 or O_2 molecules through vibration.

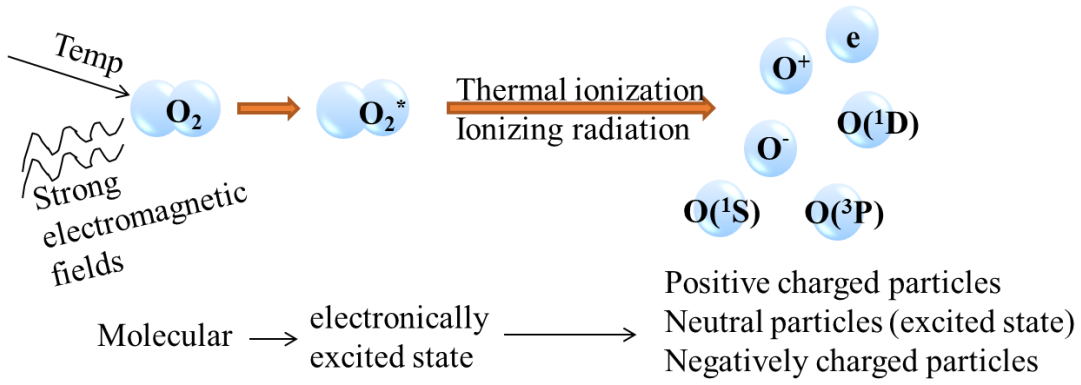

Figure 1-10. O_2 transformation process induced by discharge

As the upward discharges from thunderstorms or discharges in the stratosphere, the chemistry effects of TLEs have recently received significant attention. The study by *Sentman and Stenbaek-Nielsen* [2009], for example, determined the concentrations of species impacted by streamers. Compared to no-discharge, the study showed that

streamer impact leads to an increase in oxygen atom, $O(^1D)$ and $N_2(A^3\sum_u^+)$ by a factor of 2 and to an increase in $O_2(a)$ by a factor of 3. The study by *Gordillo-Vázquez* [2008] further concluded that H_2O affects the property of CO_4^- anions, but that there is no significant effect on NO_x formation or destruction.

Stratospheric NO_x contributes to O_3 depletion [*Callis,* 2002] and the high concentration of NO in the mesosphere can transport downward to the stratosphere in the polar winter. TLEs are thus important sources of middle atmosphere NO_x, while the effect of TLEs on NO_x production at higher altitudes still remains largely unexplored [*Pasko et al.,* 2012]. The chemical effects of sprites have been investigated in a number of model studies, e.g. those by *Hiraki et al.* [2008], *Evtushenko et al.* [2013], and *Parra-Rojas et al.* [2013]. In addition, prior studies have suggested that NO_x in the middle atmosphere are locally significantly impacted by TLEs, based either on calculation-based estimates [*Neubert et al.,* 2008; *Gordillo-Vazquez,* 2008; *Sentman et al.,* 2008; *Enell et al.,* 2008; *Arnone et al.,* 2014; *Perez-Invernon et al.,* 2019], on observation-based estimates [*Arnone et al.,* 2008], or on laboratory experiments [*Peterson et al.,* 2009]. *Enell et al.* [2008] inferred that NO_x increases by about 1 order of magnitude within streamers. The NO_x produced is significant in its local concentration and distribution, especially at high altitudes. The long-term behaviors of NO_x, O_x and HO_x species impacted by night sprites were calculated by *Hiraki et al.* [2008]. They noted that sprites can impact local chemistry for hours at high altitudes (40-70 km). *Peterson et al.* [2009] estimated that the NO_x production impacted by each event comprises 1.7×10^{22}-7.4×10^{26} molecules in blue jets and 6.8×10^{23}-6.3×10^{27} molecules in red sprites. *Perez-Invernon et al.* [2019] showed that there are about 3.8 Tg (1Tg=10^{12} grams) N_2O-N/year and 0.07 Tg NO-N/year produced by BJs near the stratosphere by using a global climate model.

In the past, more studies on sprites have been undertaken than on jets [*Chen et al.,* 2008]. However, the NO_x species interact strongly with ozone chemistry through catalytic cycles [*Johnston,* 1971; *Cohen and Murphy,* 2003] and blue jets occur in the

stratospheric ozone layer. Therefore, chemical perturbations due to BJs are of interest as they might influence the stratospheric ozone layer.

Only a few investigations have been carried out on the chemistry of BJs. With a simplified plasma chemistry model, *Mishin* [1997] reported the impact of such a discharge on ozone content. He highlighted a 10% increase in nitric oxide and a 0.5% increase in ozone at 30 km by a BJ streamer. *Smirnova et al.* [2003] further considered chemical composition, ionization, and attachment rates to study the impact of electric field perturbations on the lower stratosphere. Their simulation results indicate the importance of reactions and their rate coefficients in BJ streamer electron density governed processes (electric field driven processes). More recently, *Winkler et al.* [2015] (hereafter W2015) developed a detailed plasma chemistry model (including 88 species and more than 1000 reactions) to investigate BJ streamer impacts. The relative increases of NO_x and O_3 reported by W2015 are much larger than the increases that have been reported by other studies. For instance, at 30 km, the estimates of W2015 for NO_x increase are larger by two orders of magnitude than the estimates of *Mishin* [1997] and *Smirnova et al.* [2003]. W2015 indicated a relative O_3 increase of 2% at 30 km, while *Smirnova et al.* [2003] and *Mishin* [1997] inferred an O_3 increase of 0.03% and 0.5%, respectively. In addition, a study by *Perez-Invernon et al.* [2019] estimated the global chemical influence of BJs considering the occurrence rate at global scale, by using the Whole Atmosphere Community Climate Model (WACCM4). Their estimates indicated that BJs decrease O_3 at 30 km by up to ~5% in equatorial and in polar regions.

However, the model of W2015 did not consider bromine species (Br_y), which have an important effect on O_3 destruction, especially in the stratosphere [*Yung et al.,* 1980, *Prather et al.,* 1990]. The study by *Perez-Invernon et al.* [2019] used the local chemical results of W2015 for a single BJ (including BJ streamer and leader) to estimate the global chemical impact. Previous studies of local chemical models on BJs focused on the first hundred seconds after the discharge event, whereas NO_x species production in the stratosphere and its interaction with the ozone chemistry takes place on a timescale of several days.

For reasons of simplicity, all previous studies used a constant pulse electric field to model BJs or sprite streamers [e.g. *Winkler et al.*, 2014, 2015; *Gordillo-Vázquez*, 2008; *Sentman et al.*, 2008], while it is well-established that the real streamer electric field varies through time during the discharge process [*Ihaddadene and Celestin*, 2017].

1.3 Plasma chemistry processes

The plasma chemistry taking place during electric field-driven processes in BJ streamers includes chemical reactions related to positive ions, negative ions and neutral excited state species. They include reaction types of electron attachment, detachment processes, associative and Penning ionization, positive ion chemistry, negative ion chemistry, electron-ion recombination, ion-ion recombination and radiative de-excitation. The excitation, de-excitation, ionization and recombination chemistry processes are summarized schematically in Figure 1-11.

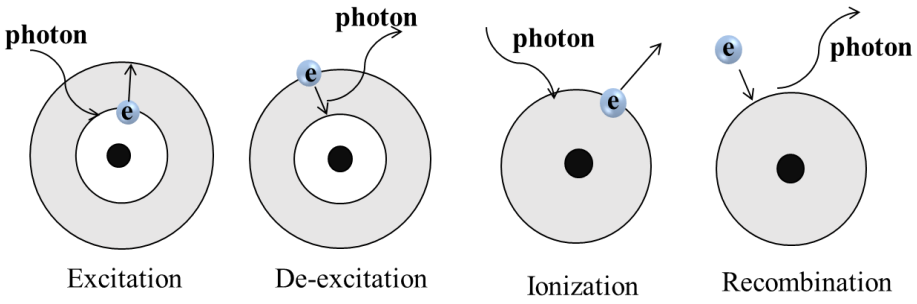

Figure 1-11. Excitation, de-excitation, ionization and recombination processes.

An electron attachment process is the excitation of the electronic states of electrons and the ionization of neutral particles by electron impacts. The electronic states of particles are short-lived.

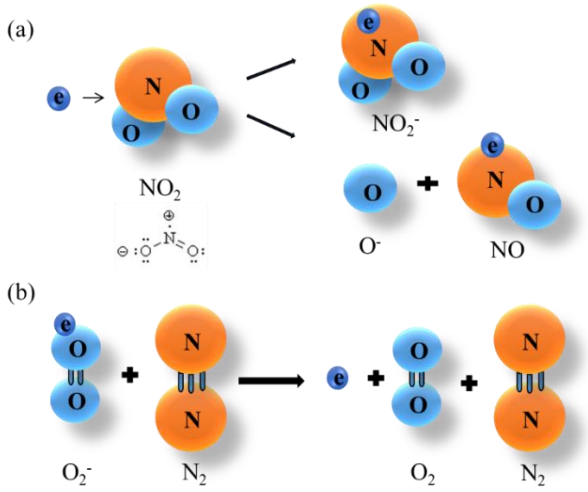

Figure 1-12. Examples for (a) attachment reactions, (b) a detachment reaction

Examples of the two processes are shown in Figure 1-12, (a) for attachment: $e^- + NO_2 \rightarrow NO_2^-$ and $e^- + NO_2 \rightarrow NO + O^-$, (b) for detachment: $O_2^- + N_2 \rightarrow e^- + O_2 + N_2$.

Electronically excited species during the discharge process are influenced by associative and Penning ionization processes [*Gritsinin et al.*, 1987; *Baiadze et al.*, 1985] and the processes are represented by the associated chemical reactions [*Brunet et al.*, 1985].

1.4 Summary

Recently, many TLEs have been observed. The TLE family includes blue jets (BJs), sprites and elves, which occurs in the stratosphere and in the mesosphere. Research has demonstrated that these electric discharge events in the middle atmosphere can perturb stratospheric O_3 through catalytic O_3 loss cycles by producing NO_x (=NO+NO_2).

The altitude where blue jets occur is located in the stratospheric ozone layer. This study focuses on the chemical impact of streamers associated with blue jets and gigantic jet events, which develop above thunderstorms. These electrical discharges are a result of an electrical charge imbalance inside thunderstorms, including the discharge of

leaders and streamers. The discharge typically occurs upward with vertical velocities of ~100 km/s and with a duration of ~200-300 milliseconds.

The objective of this study is to evaluate the potential impacts of blue jet streamer discharges on stratospheric chemistry. The questions are addressed:

- Which chemical reaction system and associated reaction rates should be considered?

Chapters 2 and 4

- How should the discharge associated with the streamer be represented?

Chapters 2 and 4

- What is the impact of a streamer on nitrogen oxide and ozone content according to the time scale considered (100 s, 48 h)?

Chapters 4 and 5

- What are the impacts of electric discharge associated with the BJ streamer on the balance of the stratospheric chemical system as a function of the altitude?

Chapter 5

CHAPTER Ⅱ

MIPO-STREAMER MODEL DESCRIPTION

Contents

Le modèle MiPO-Streamer développé et utilisé dans cette étude est basé sur le modèle Microphysical and Photochemical Lagrangian Stratospheric Model of Ozone (MiPLaSMO). Le modèle MiPLaSMO a été développé au LPC2E (Laboratoire de Physique et de Chimie de l'Environnement et de l'Espace) et a été largement utilisé au cours des 20 dernières années pour interpréter les mesures sous ballon stratosphérique et sur satellite associées à l'ozone stratosphérique [par exemple, *Croizé et al.,* 2015, *Grossel et al., 2010*, *Brogniez et al.,* 2003, *Huret et al.,* 2003, *Rivière et al.,* 2002, *Rivière et al.,* 2000].

Cette partie présente le modèle MiPO-Streamer, les espèces chimiques et l'ensemble des réactions prises en compte, ainsi que les deux paramétrisations associées au BJ streamer.

The MiPO-Streamer model developed and employed in this study is based on the Microphysical and Photochemical Lagrangian Stratospheric Model of Ozone (MiPLaSMO) model. The MiPLaSMO model was developed at LPC2E (Laboratoire de Physique et de Chimie de l'Environnement et de l'Espace) and has been widely used over the last 20 years to interpret balloon and satellite measurements associated with stratospheric ozone [e.g. *Croizé et al.,* 2015, *Grossel et al.,* 2010, *Brogniez et al.,* 2003, *Huret et al.,* 2003, *Rivière et al.,* 2002, *Rivière et al.,* 2000].

This part will present the MiPO-Streamer model and the model initialization. The model description includes the introduction of the box model used, the chemical species and sets of reactions considered, and the parameterization of electric-driven processes that characterize BJ streamer discharge processes.

2.1 MiPO-Streamer model description

MiPLaSMO model describes the time evolution of the chemical, microphysical, and thermodynamic properties of an air parcel through a chemistry reaction scheme (133 photochemical gaseous and heterogeneous reactions) and microphysics calculations (size distribution and nature of aerosols) for 5 types of stratospheric particles (liquid binary aerosols, sulfuric acid tetrahydrate particles, type Ia polar stratospheric cloud (PSC, nitric acid trihydrate), liquid type Ib PSC (supercooled ternary solution, $H_2SO_4/HNO_3/H_2O$), and type II PSC (ice particles)). This model is described in more detail by *Rivière et al.* [2000].

2.1.1 The box model

In this thesis, the model is used in its box model version (closed system, zero-dimension) which is briefly summarized in Figure 2-1. Each "air box" represents the time evolution of chemical concentration, and microphysics (size distribution and

nature of aerosols and polar stratospheric clouds) at different altitudes. This box includes a characteristic distribution of aerosols and the chemical compounds of the stratospheric chemical species associated with oxygen, hydrogen, nitrogen, chlorine and bromine families. The nonlinear system of equations governing the chemical species evolution is converted into a linear system of equations using a semi-implicit symmetric (SIS) method. The system is given with:

$$\vec{y}_{n+1} - \vec{y}_n = \frac{h}{2}\left(\frac{\partial \vec{f}}{\partial \vec{y}}\right)_n \vec{y}_{n+1} \qquad (2\text{-}1)$$

where (consider an example, e.g. $aA + bB \rightarrow cC + dD$, of a system of two chemical species A and B)

$$\vec{y} = ({}^1y,\ {}^2y)^T \qquad (2\text{-}2)$$

$$\vec{f} = ({}^1f,\ {}^2f)^T \qquad (2\text{-}3)$$

$$h = \Delta t = \frac{t_n - t_0}{n} \qquad (2\text{-}4)$$

and

$$f = f(t, y) \qquad (2\text{-}5)$$

where t is time, h is the time step, y is the concentration of the given compounds (${}^1y$ and ${}^2y$ are the concentrations of A and B in the example given here), ${}^1f$ and ${}^2f$ represent respectively the loss and production rates of the compounds, conserving the number of atoms and molecules. A description of this method can be found in the work by *Ramaroson et al.* [1989, 1992]. The time step of the model can be easily adapted with typically 5 minutes during day and night, reduced to 30 s for twilight periods in its basic neutral chemistry configuration [*Rivière et al. 2000*]. To take into account the very fast plasma chemistry processes occurring during a BJ streamer discharge, several sensitivity tests were conducted to prevent instabilities due to the increase in the system stiffness. Thus, during the BJ event the time step is reduced to 10^{-11} s.

This numerical method has been recently adapted to manage the stiffness of the system automatically (SIS Method). It has been used to simulate the atmospheric chemistry of Venus [*Stolzenbach,* 2016].

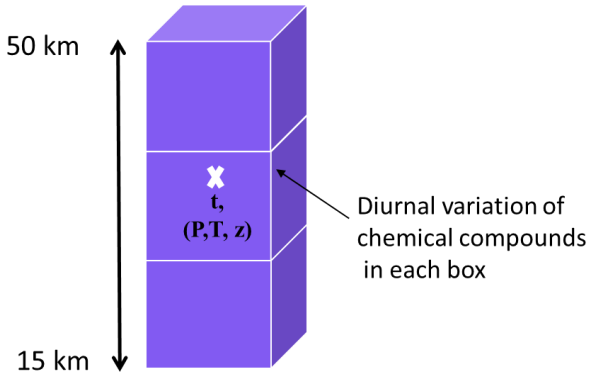

Figure 2-1. MiPLaSMO model properties of an air mass.

2.1.2 Chemical species

The MiPLaSMO model only includes 42 neutral species which are shown in Table 2-1.

Table 2-1. Neutral species considered in the MiPLaSMO model

N_2	O_2	H_2O	CH_4	H_2	CO	
O_3	O	$O(^1D)$				
H	OH	HO_2	H_2O_2			
N	NO	NO_2	NO_3	N_2O_5	HNO_3	HO_2NO_2
Cl	ClO	HCl	HOCl	OClO	Cl_2O_2	
Cl_2	$ClNO_2$	$ClONO_2$				
Br	BrO	HOBr	HBr	BrCl	$BrONO_2$	Br_2
CH_3	CH_2O	CH_3O_2	CH_3O	CH_3OOH	CHO	

In order to evaluate the potential chemistry impact by streamer discharge processes, the chemical scheme of the MiPO-Streamer model has been enlarged to include plasma chemistry. Taken from W2015, the additional neutral species are shown in Table 2-2. They are excited state species, N_3, N_2O, N_2O_2, HNO, HNO_2, CO_2, CO_3 and HCO_3. Most excited state species are first generated through electric field driven processes. In this study, an abbreviated notation of excited species is also used, e.g. $N_2(A)= N_2(A^3\sum_u^+)$, depending on the context. As the background species of N_2, O_2, H_2O, CH_4, H_2, CO and CO_2 have a high density, these species are held constant during the simulation.

Table 2-2. The additional neutral species considered in the MiPO-Streamer model

$N_2(A^3\sum_u^+)$	$N_2(B^3\prod_g)$	$N_2(C^3\prod_u)$	$N_2(a^1\prod_g)$	$N_2(a'^1\sum_u^-)$	$N(^2D)$	$N(^2P)$
$O(^1S)$	$O_2(a)$	$O_2(b)$				
N_2O	N_2O_2	N_3	N_4	HNO	HNO_2	
CO_2	CO_3	HCO_3				

The additional positive and negative ion species are shown in Tables 2-3 and 2-4. As the MiPO-Streamer model considered bromine species, compared to W2015, there are two additional negative ion species, Br^- and BrO^-. After taking plasma chemistry into account, there are 117 species in the MiPO-Streamer model.

Table 2-3. Positive ions considered in the MiPO-Streamer model

N^+	N_2^+	N_3^+	N_4^+	O^+	O_2^+	O_4^+	NO^+	NO_2^+	N_2O^+	$N_2O_2^+$
$NO^+(N_2)$	$NO^+(O_2)$	H_2O^+	OH^+	$H^+(H_2O)_{n=1-7}$		$H^+(H_2O)(OH)$		$O_2^+(H_2O)$		
$H^+(H_2O)(CO_2)$		$H^+(H_2O)_2(CO_2)$		$H^+(H_2O)(N_2)$			$H^+(H_2O)_2(N_2)$			
$NO^+(H_2O)_{n=1-3}$		$NO^+(CO_2)$		$NO^+(H_2O)(CO_2)$						
$NO^+(H_2O)_2(CO_2)$		$NO^+(H_2O)(N_2)$		$NO^+(H_2O)_2(N_2)$						

Table 2-4. Negative ions considered in the MiPO-Streamer model

e^-								
O^-	O_2^-	O_3^-	O_4^-	NO^-	NO_2^-	NO_3^-	CO_3^-	CO_4^-
$O^-(H_2O)$		$O_2^-(H_2O)$		$O_3^-(H_2O)$	OH^-	HCO_3^-		
Cl^-		ClO^-		Br^-	BrO^-			

2.1.3 Sets of reactions and reaction coefficient rates

Compared to the MiPLaSMO model, the MiPO-Streamer model has 293 more neutral chemistry reactions, which are taken from W2015. Most reaction rate coefficients are also taken from W2015, but some of them are taken from the Jet Propulsion Laboratory [*Sander et al.*, 2006, hereafter JPL]. The sets of reactions associated with plasma chemistry processes in the MiPO-Streamer model were also taken from the W2015 study. The sets of reactions and reaction rates used are shown in Annex 1.

However, compared to the model developed by W2015, the MiPO-Streamer model considers more neutral species relevant for stratospheric investigations, including additional bromine species (Br_y), chlorine species (Cl_y), hydrogen species and their corresponding reactions, and additional photochemistry of NO_x (for details, see Annex 1). The rate coefficients of these reactions are taken from the JPL.

Besides, given that W2015 did not consider Br_y, the bromine ion reactions added in the MiPO-Streamer model use the reaction rates inferred by *Kopp et al.* [1997]. The rate coefficients for bromine ion reactions are displayed in Table 2-5.

Table 2-5. Reactions of bromine ions in the MiPO-Streamer model. The rate coefficients are those of Kopp et al. [1997].

	Reactions of bromine ions	Rate Coefficient (Kopp et al.,1997)
1	$O_2^- + HBr \rightarrow Br^- + HO_2$	5.2×10^{-10}
2	$OH^- + HBr \rightarrow Br^- + H_2O$	1.5×10^{-9}
3	$NO_3^- + HBr \rightarrow Br^- + HNO_3$	3.3×10^{-10}
4	$Br^- + HNO_3 \rightarrow NO_3^- + HBr$	7.0×10^{-10}
5	$Br^- + O_3 \rightarrow BrO^- + O_2$	5.0×10^{-13}
6	$BrO^- + O_3 \rightarrow Br^- + O_2 + O_2$	6.0×10^{-11}
7	$Br^- + H \rightarrow e^- + HBr$	9.6×10^{-10}

There is a total of 1760 reactions in the MiPO-Streamer model.

The expression of the reaction rate coefficients for bimolecular reactions, tri-molecular reactions and photo-dissociation reactions are expressed in the following ways.

2.1.3.1 Bimolecular reactions

For two body reactions,

$$aA + bB \rightarrow cC + dD \qquad (2\text{-}6)$$

the reaction constant k (cm^3 $molec^{-1}$ s^{-1}) is defined by the relationship:

$$k = -\frac{1}{a}\frac{d[A]}{dt} = -\frac{1}{b}\frac{d[B]}{dt} = \frac{1}{c}\frac{d[C]}{dt} = \frac{1}{d}\frac{d[D]}{dt} \qquad (2\text{-}7)$$

where [X] is the concentration of compound X in molec/cm^3. The constant k depends on the temperature and is expressed in the form of an Arrhenius law:

$$k(T) = A\exp[(-\frac{E}{R})(\frac{1}{T})] \qquad (2\text{-}8)$$

where E is the activation energy for the reaction, R is the universal gas constant and T is the absolute temperature (in Kelvin). The coefficients A and E/R are given by *DeMore et al.* [1997] and *Sander et al.* [2011].

The reaction rate is often found to be expressed in the form:

$$r = k(T)[A]^m[B]^n \qquad (2\text{-}9)$$

Here k(T) is the reaction rate constant that depends on temperature. [A] and [B] are the concentrations of substances A and B in molec per volume. The exponents m and n are called partial orders of reaction. They are not generally equal to the stoichiometric coefficients a and b, but depend on the reaction mechanism and can be determined experimentally.

2.1.3.2 Tri-molecular reactions

For three-body reactions,

$$A + B + M \rightarrow C + D + M \qquad (2\text{-}10)$$

where M represents a molecule of air. The constant rate k (cm^6 $molec^{-2}$ s^{-1}) can be expressed in a three-body reaction as a constant rate of second order, which depends on pressure and temperature:

$$k(M,T) = \left[\frac{k_0(T)[M]}{1+[k_0(T)[M]/k_\infty(T)]}\right] 0.6^{\{1+[\log(k_0(T)[M])/k_\infty(T)]^2\}^{-1}} \qquad (2\text{-}11)$$

with

$$k_0(T) = k_0^{300}(T/300)^{-n} \qquad (2\text{-}12)$$

$$k_\infty(T) = k_\infty^{300}(T/300)^{-m} \qquad (2\text{-}13)$$

where k_0^{300} is adjusted for M as a third body, k_∞^{300} is in the limit of high pressures. More details on the calculation of data k_0^{300}, k_∞^{300}, m and n can be found in *DeMore et al.* [1997] and *Sander et al.* [2011].

2.1.3.3 Photo-dissociation reactions

For photo-dissociation reactions,

$$A + h\nu \rightarrow B + C \qquad (2\text{-}14)$$

the constant rate J (or photo-dissociation coefficient), expressed in s^{-1} is:

$$\frac{d[A]}{dt} = -J[A] \qquad (2\text{-}15)$$

J is expressed in terms of the quantum yield of the reaction (Φ), the absorption cross-section (σ) and the solar spherical or point irradiance (F) of compound A. The quantum yield and cross-section are dependent on the wavelength λ and temperature *T*. The spherical or point irradiance is dependent on the wavelength λ and solar zenith angle θ. J is in the wavelength interval between λ and λ+dλ:

$$J = \int_{\lambda 1}^{\lambda 2} \Phi(\lambda, T)\sigma(\lambda, T)F(\theta, \lambda)d\lambda \qquad (2\text{-}16)$$

where Φ is ≤ 1, σ in cm^2, and F in photons s^{-1} cm^{-2} nm^{-1}. λ_1 and λ_2 define the wavelength range within which compound A is absorbed.

The solar spherical or point irradiance at altitude z is:

$$F_\lambda(z) = F_{\lambda,\infty} e^{-\frac{\delta}{\cos\theta}} \qquad (2\text{-}17)$$

Where $F_{\lambda,\infty}$ is at the top of the atmosphere, θ is the solar zenith angle (between the sun and the vertical), and δ is the optical depth of the atmosphere above z computed:

$$\delta = \int_z^\infty (\sigma_{O2} n_{O2}(z) + \sigma_{O3} n_{O3}(z))dz \qquad (2\text{-}18)$$

where n_{O2} and n_{O3} are the densities of O_2 and O_3. Thus, because of the efficient absorption by O_2 and O_3 [*DeMore et al.*, 1997], the F values at UV wavelengths decrease rapidly with decreasing altitude in the stratosphere.

2.1.4 Electric field driven reactions

2.1.4.1 Sets of reactions

Various authors have inferred sets of reactions for electric field driven processes. *Gordillo-Vazquez* [2008] considered Ar, O_3, O, N_2O, NO, H_2O and CO_2 species through 45 electric field driven reactions (Table 2-6). They performed simulations at three altitudes (63 km, 68 km, 78 km) and investigated the non-equilibrium plasma chemistry triggered by a sprite streamer. They investigated the optical emission associated with sprites. Besides visible emissions, sprites emit in the IR and UV regions. As the IR and UV emissions come from excited species of, e.g. CO_2, N_2, NO and/or N_2^+, they are usually strongly absorbed by H_2O (IR emissions) and O_2 (UV emissions). In the study by *Sentman et al.* [2008], a single sprite streamer at an altitude of 70 km was investigated using a simplified set of reactions (23 reactions) associated with N_2 and O_2 species (Table 2-7). They focused on the chemical effect induced by the passage of a sprite streamer and simulations during 1000 s, particularly on ion concentration perturbations.

More recently *Winkler et al.* [2014] focused on daytime BJ events in the altitude range of 30-54 km. They accounted for the electron impact reactions with N_2 and O_2 given in Table 2-8, considering 20 sets of electric field driven reactions.

All these studies investigated the early chemical perturbations from streamer discharges, i.e. during the first 100 s to 1000 s after the event. They did not investigate the potential chemical impact of the discharge on the neutral chemistry equilibrium relevant for ozone distribution in the atmosphere, which can take several days.

Table 2-6. Reactions associated with electron driven chemistry [*Gordillo-Vazquez,* 2008]. The rate coefficients for the electron-impact processes are evaluated using the calculated electron distribution function (EDF) and the corresponding cross-section (references are shown below the table).

	Reaction
	EDF-dependent processes (1)
1	$Ar + e \rightarrow Ar(^3P_2) + e$
2	$Ar + e \rightarrow Ar^+ + 2e$
3	$N_2 + e \leftrightarrow N_2(v_i) + e;\ (i = 1, \ldots 8)$
4	$N_2(v_1) + e \leftrightarrow N_2(v_2) + e$
5	$N_2(v_2) + e \leftrightarrow N_2(v_3) + e$
6	$N_2(v_3) + e \leftrightarrow N_2(v_4) + e$
7	$N_2(v_4) + e \leftrightarrow N_2(v_5) + e$
8	$N_2(v_5) + e \leftrightarrow N_2(v_6) + e$
9	$N_2(v_6) + e \leftrightarrow N_2(v_7) + e$
10	$N_2(v_7) + e \leftrightarrow N_2(v_8) + e$
11	$N_2 + e \rightarrow N_2(A\,^3\Sigma_u^+) + e$
12	$N_2 + e \rightarrow N_2(a\,^1\Pi_g) + e$
13	$N_2 + e \rightarrow N_2(a'\,^1\Sigma_u^-) + e$
14	$N_2 + e \rightarrow N_2(B\,^3\Pi_g) + e$
15	$N_2 + e \rightarrow N_2(C\,^3\Pi_u) + e$
16	$N_2 + e \rightarrow N_2^+ + 2e$
17	$N_2 + e \rightarrow N_2^+(B\,^2\Sigma_u^+) + 2e$
18	$N_2 + e \rightarrow N + N + e$
19	$N_2 + e \rightarrow N + N(^2D) + e$
20	$N_2 + e \rightarrow N + N(^2P) + e$
21	$O_2 + e \rightarrow O_2^+ + 2e$
22	$O_2 + e \rightarrow O_2(a\,^1\Delta_g) + e$
23	$O_2 + e \rightarrow O_2(b\,^1\Sigma_g^+) + e$
24	$O_2 + e \rightarrow O + O + e$
25	$O_2 + e \rightarrow O^- + O$
26	$O_3 + e \rightarrow O^- + O_2$
27	$O_3 + e \rightarrow O_2^- + O$
28	$O + e \rightarrow O^+ + 2e$
29	$O + e \rightarrow O(^1D) + e$
30	$O + e \rightarrow O(^1S) + e$
31	$N_2O + e \rightarrow N_2 + O^-$
32	$N_2O + e \rightarrow N_2O^+ + 2e$
33	$NO + e \rightarrow N + O^-$
34	$NO + e \rightarrow NO^+ + 2e$
35	$NO + e \rightarrow NO(A\,^2\Sigma^+) + e$

	Reaction
	EDF-dependent processes (2)
36	$H_2O + e \rightarrow H + OH + e$
37	$H_2O + e \rightarrow O(^1D) + H_2 + e$
38	$H_2O + e \rightarrow H_2O^+ + 2e$
39	$H_2O + e \rightarrow OH^- + H$
40	$H_2O + e \rightarrow H^- + OH$
41	$H_2O + e \rightarrow H_2 + O^-$
42	$CO_2 + e \leftrightarrow CO_2(0\,1\,0) + e$
43	$CO_2 + e \leftrightarrow CO_2(1\,0\,0) + e$
44	$CO_2 + e \leftrightarrow CO_2(0\,0\,1) + e$
45	$CO_2 + e \rightarrow CO + O^-$

(Reaction 17): *Capitelli et al.* [2000];

(Reaction 1-16, 18, 21-25): http://jilawww.colorado.edu/ avp/collision data/;

(Reaction 19, 20, 45): *Christophorou* [1984];

(Reaction 26, 27): *Skalny et al.* [1996];

(Reaction 28): *Brook et al.* [1978];

(Reaction 29, 30): *Majeed and Strickland* [1997];

(Reaction 31-35, 42-44, 42-44): *Hayashi* [1990];

(Reaction 36, 28-41): *Itikawa and Mason* [2005];

(Reaction 37): *Yousfi and Benabdessadok* [1996].

Table 2-7. Data used in the analytic evaluation of the rate coefficients for electron impact processes [*Sentman et al.*, 2008]. Numbers given in the form 1.23(4) mean 1.23×10^4, the logarithm is given for a base of 10.

Reaction No. From Table A1	Process	$f(E/N)$	Comment
(R5)	$e^* + N_2 \rightarrow e + e + N_2^+$	$\log k_5 = -(8.3 + 365/\theta)$	
(R6)	$e^* + O_2 \rightarrow e + e + O_2^+$	$\log k_6 = -(8.8 + 281/\theta)$	
(R7)	$e^* + N_2 \rightarrow e + N_2(v > 0)$	$k_7 = 10\ k_8$	(estimated $v = 1\ldots4$)
(R8)	$e^* + N_2 \rightarrow e + N_2(A)$	$\log k_8 = -(8.4 + 140/\theta)$	
(R9)	$e^* + N_2 \rightarrow e + N_2(B, W^3, B')$	$\log k_B = -(8.2 + 148/\theta)$	$k_9 = k_B + k_{W^3} + k_{B'}$
	$N_2(W^3, B') \xrightarrow{st} N_2(B)$	$\log k_{W} = -(8.3 + 154/\theta)$	
		$\log k_{B'} = -(8.7 + 168/\theta)$	
(R10)	$e^* + N_2 \rightarrow e + N_2(a', a, w^1)$	$\log k_{a'} = -(8.8 + 167/\theta)$	$k_{10} = k_{a'} + k_a + k_{w}$
	$N_2(a, w^1) \xrightarrow{st} N_2(a')$	$\log k_a = -(8.3 + 174/\theta)$	
		$\log k_{w} = -(8.8 + 175/\theta)$	
(R11)	$e^* + N_2 \rightarrow e + N_2(C, E, a'')$	$\log k_C = -(8.2 + 211/\theta)$	$k_{11} = k_C + k_E + k_{a''}$
	$N_2(E, a'') \xrightarrow{st} N_2(C)$	$\log k_E = -(10.1 + 254/\theta)$	
		$\log k_{a''} = -(9.2 + 262/\theta)$	
(R12)	$e^* + O_2 \rightarrow e + O_2(a)$	$\log k_{12} = -(10.2 + 3.5/\theta)$, $\theta > 40$, $= -(9.0 + 52/\theta)$, $\theta < 40$	(estimated from *Kossyi et al.* [1992])
(R13)	$e^* + O_2 \rightarrow e + O_2(b)$	$\log k_{13} = -(11.2 + 7.2/\theta)$, $\theta > 30$, $= -(9.5 + 60/\theta)$, $\theta < 30$	(estimated from *Kossyi et al.* [1992])
(R14)	$e^* + N_2 \rightarrow e + N + N$	$k_{14} = 2\ k_{15}$	(estimated from *Borisov et al.* [1993])
(R15)	$e^* + N_2 \rightarrow e + N + N(^2D)$	$k_{15} = 10^{-10}$ [3.096 −.671 Θ + 0.03 Θ^2 +1.59(−3) Θ^3 − 1.57(−5) Θ^4]	$\Theta = \theta/10$ $k_{15} = 0$ for $\theta < 76$ Td
(R16)	$e^* + O_2 \rightarrow e + O + O$	$\log k_{16} = -(7.9 + 134/\theta)$	
(R17)	$e^* + O_2 \rightarrow e + O + O(^1D)$	$\log k_{17} = -(8.0 + 169/\theta)$	
(R18)	$e^* + O_2 \rightarrow e + O + O(^1S)$	$\log k_{18} = -(8.8 + 119/\theta)$	
(R19)	$e^* + O_2 \rightarrow e + O + O^-$	$\log k_{19} = -(10.4 + 57/\theta)$, $\theta > 80$, $= -(9.575 + 123/\theta)$, $\theta < 80$	(estimated from *Kossyi et al.* [1992])
(R20)	$e^* + N_2(A) \rightarrow e + e + N_2^+$	$\log k_{20} = -(8.1 + 121/\theta)$	
(R21)	$e^* + N_2 \rightarrow e + e + N^+ + N$	$k_{21} = 3.18(-14)\ (T_e/300)^2 \times \exp(-296266/T_e)$	
		$T_e = 6[1.16(4)\ \theta/615]$	T_e (K) evaluated from (5) in text
(R22)	$e^* + O_2 \rightarrow e + e + O^+ + O$	$k_{22} = 3.18(-14)\ (T_e/300)^2 \times \exp(-206055/T_e)$	T_e (K) evaluated from (5) in text
		$T_e = 6[1.16(4)\ \theta]/615$	
(R23)	$e^* + O^- \rightarrow e + e + O$	$\log k_{23} = -(6.5 + 440/\theta)$	

Table 2-8. Electric field driven processes in the model [*Winkler et al.*, 2014]

Reaction			Reference(s)*
Ionisation			
$e + N_2$	$\rightarrow$	$N_2^+ + 2\,e$	1, 2
$e + N_2$	$\rightarrow$	$N^+ + N + 2\,e$	2, 3
$e + N_2$	$\rightarrow$	$N^+ + N(^2D) + 2\,e$	3
$e + O_2$	$\rightarrow$	$O_2^+ + 2\,e$	5
$e + O_2$	$\rightarrow$	$O^+ + O + 2\,e$	5
Attachment			
$e + O_2$	$\rightarrow$	$O^- + O$	1
Dissociation			
$e + N_2$	$\rightarrow$	$N + N + e$	3, 4
$e + N_2$	$\rightarrow$	$N + N(^2D) + e$	3
$e + N_2$	$\rightarrow$	$N + N(^2P) + e$	3
$e + O_2$	$\rightarrow$	$O + O + e$	6
$e + O_2$	$\rightarrow$	$O + O(^1D) + e$	5
$e + O_2$	$\rightarrow$	$O + O(^1S) + e$	7
Excitation			
$e + N_2$	$\rightarrow$	$N_2(A) + e$	1
$e + N_2$	$\rightarrow$	$N_2(B) + e$	1
$e + N_2$	$\rightarrow$	$N_2(a'^1) + e$	1
$e + N_2$	$\rightarrow$	$N_2(a^1) + e$	1
$e + N_2$	$\rightarrow$	$N_2(C) + e$	1
$e + O_2$	$\rightarrow$	$O_2(a) + e$	1
$e + O_2$	$\rightarrow$	$O_2(b) + e$	1
Detachment			
$O^- + N_2$	$\rightarrow$	$N_2O + e$	8

*(1) *http://jila.colorado.edu/~avp/collision_data/* (downloaded 3 January 2012); (2) *Itikawa* [2006]; (3) *Zipf et al.* [1980]; (4) *Cosby* [1993a]; (5) *Itikawa* [2009]; (6) *Cosby* [1993b]; (7) *LeClair and McConkey* [1993]; (8) *Luque and Gordillo-Vázquez* [2012].

To date, there is no agreement as to which sets of reactions should best be used because it depends on the processes investigated. However, since the altitudes at which BJs occur are close to the simulation altitudes of *Winkler et al.* [2014], and as a first step the light emission is not focused on, the same simplified sets of electric field driven reactions as those proposed in *Winkler et al.* [2014] are used. This thesis will closely compare our results to those of W2015 in order to validate our developments and investigate the impact of the discharge far from the event by performing several-day simulations to evaluate the potential impact of stratospheric ozone distribution.

2.1.4.2 Reaction coefficient rates

Electric field driven processes enhance the densities of electrons, atomic nitrogen, atomic oxygen, the excited states of atomic nitrogen and oxygen, and the excited states of N_2 and O_2. The rate coefficients of reactions in electric field driven processes depend on the electron energy distribution function (EEDF). Generally, they are calculated with collision cross-section data by solving the electron Boltzmann equation (BE):

$$\frac{\partial f}{\partial t} + v \cdot \nabla f - \frac{e}{m} E \cdot \nabla_v f = C[f] \qquad (2\text{-}19)$$

where f is the electron distribution in six-dimensional phase space, v are the velocity coordinates, e is the elementary charge, m is the electron mass, E is the electric field, ∇_v is the velocity gradient operator and C represents the rate of change in f due to collisions. The BOLSIG+ solver [*Hagelaar and Pitchford*, 2005] is a user-friendly BE solver that was used in this thesis.

In this study, the sets of reactions for electric field driven electron impact processes were taken from W2015. The reaction rate coefficients as functions of the reduced electric field ($\theta = \frac{E}{N}$, with E being the time-dependent electric field strength, and N the local air density) were calculated with the BOLSIG+ solver. As an example of 27 km shown in Figure 2-2, the BOLSIG+ solver starts with reading the electron collision files of cross-sections, setting calculation background conditions, e.g. reduced electric field, temperature and gas composition, as input parametrizations. The cross-section for electron collision depends on the free electron energy. The cross-section data used are displayed in Annex 2. The terms presented in 'Collisions' on Figure 2-2 are reaction number, species, reaction type and reaction threshold energy. The condition parameters are temperature (set to 223 K at 27 km) and N_2:O_2 proportion (set to 80:20). The rate coefficients depend on reduced electric fields and the fields are set every 25 Td from 0 Td to 600 Td (1 Td = 10^{-17} V cm^2).

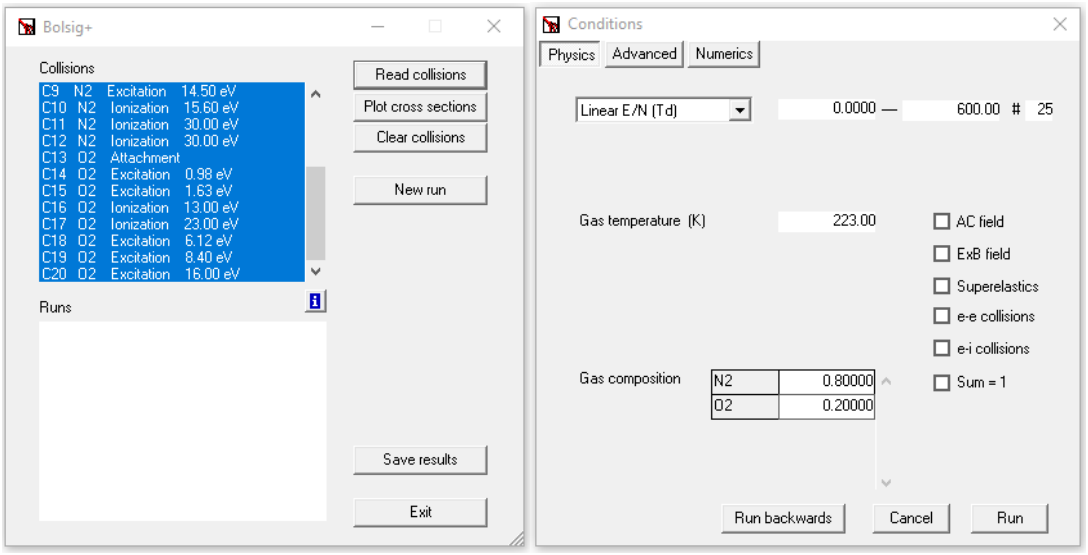

Figure 2-2. The BOLSIG+ solver starts by reading the collision files of cross-section (left) and setting calculation background conditions (right).

After running the BOLSIG+ solver, as an output, it gives the rate coefficients for all the reactions, which are considered in electric field driven processes, at each reduced electric field (Figure 2-3). The terms presented in 'Runs' on Figure 2-3 (left) are run number, reduced electric field, and energy. Figure 2-3 (right) shows an example of rate coefficients of the considered reactions at a reduced electric field of 600 Td. The units of rate coefficients from the BOLSIG+ solver are m^3/s.

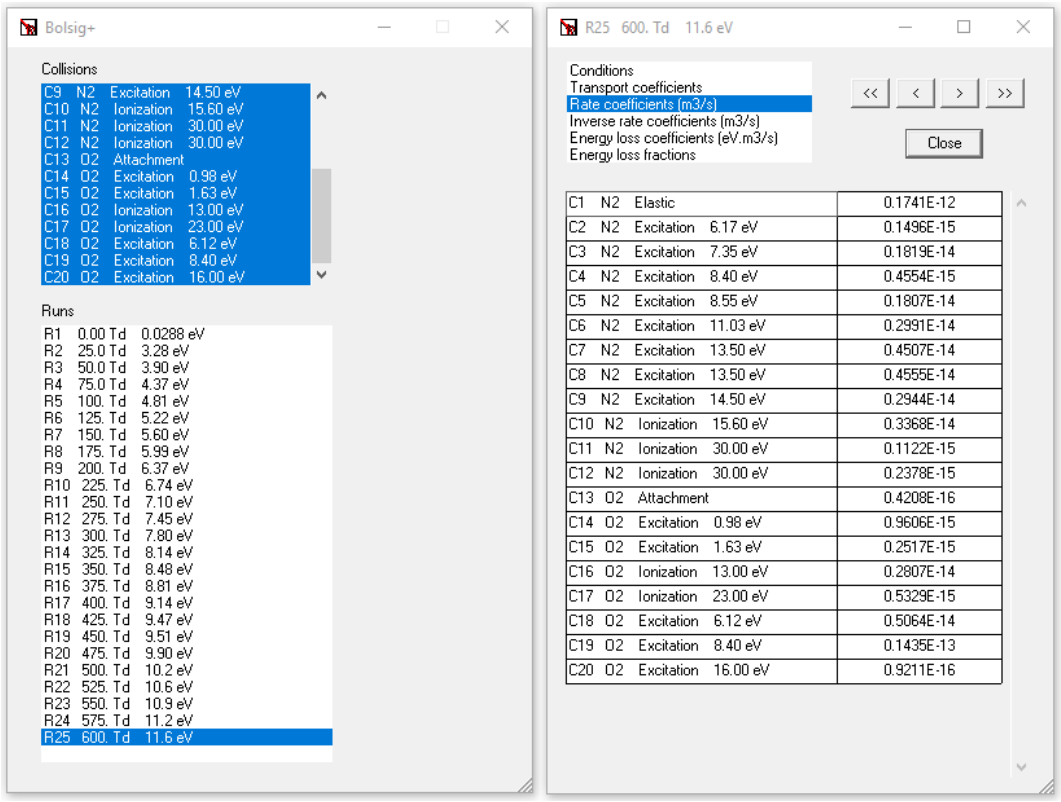

Figure 2-3. The rate coefficients of all reactions considered in electric field driven processes are shown for a reduced electric field of 600 Td as an example (right).

The rate coefficients calculated as a function of reduced electric fields are displayed in Figures 2-4, 2-5, and 2-6. The labels of curves indicate the reactions in Table 2-9. All the curves obtained are discontinuous and their discontinuous points appear at the reduced electric field of ~450 Td. This is caused by the EEDF. The rate coefficients depend on the EEDF (F_0) as:

$$k_i = \gamma \int_0^\infty \varepsilon \sigma_i F_0 d\varepsilon \qquad (2\text{-}20)$$

where $\gamma = (2e/m)^{1/2}$ is a constant, $\varepsilon = (v/\gamma)^2$ is the electron energy in eV, and σ_i is the total cross-section for inelastic collisions. The numerical solution of the EEDF equation assumes that F_0 is piecewise exponential due to the exponential factors in the scattering-out and scattering-in integrals. For further details, see the study by *Hagelaar and Pitchford* [2005].

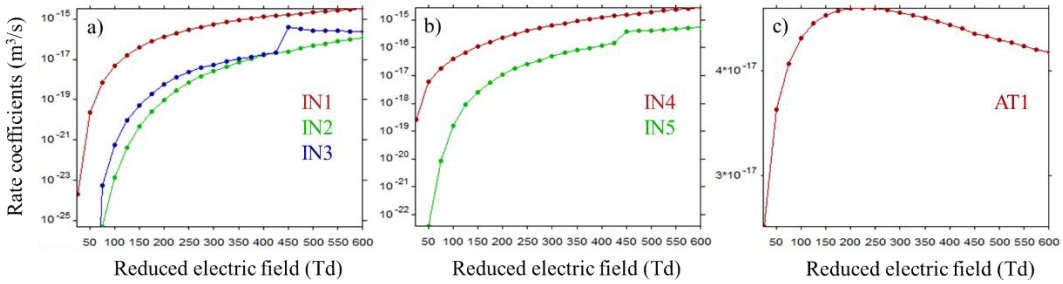

Figure 2-4. Reaction rate coefficients of (a) N_2 ionization, (b) O_2 ionization and (c) O_2 attachment.

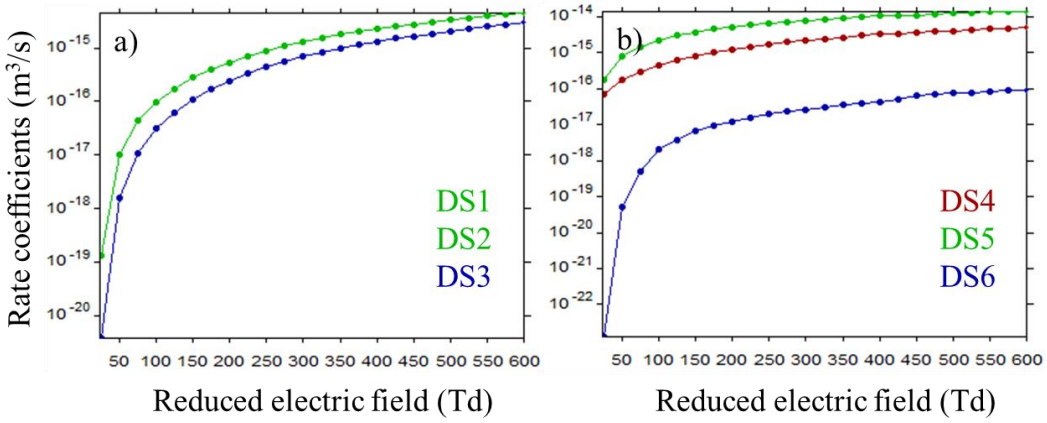

Figure 2-5. Reaction rate coefficients of (a) N_2 dissociation, (b) O_2 dissociation.

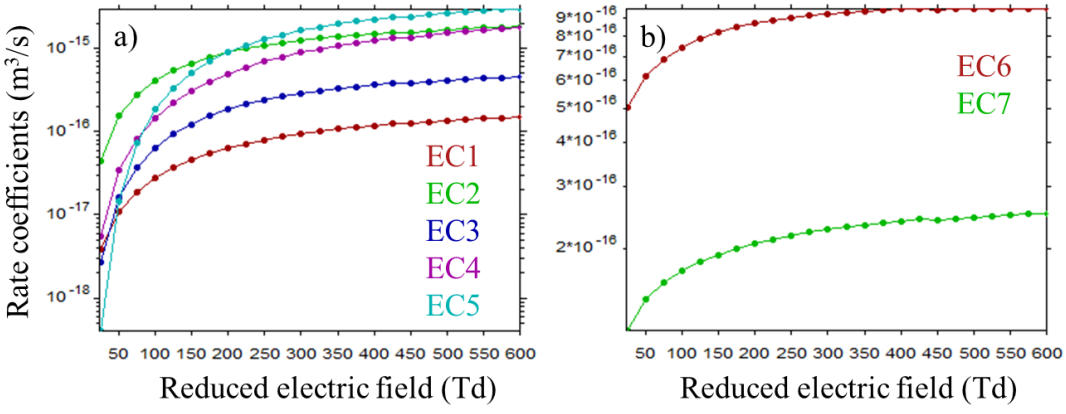

Figure 2-6. Reaction rate coefficients of (a) N_2 excitation, (b) O_2 excitation.

The reactions considered in the model, those associated with N_2 and O_2 by electron impact and their rate coefficients are shown in Table 2-9. As suggested by the

BOLSIG+ solver, the fit functions of rate coefficients use the form of $k_i = e^{(A_i + B_i \times \ln(\theta) + \frac{C_i}{\theta} + \frac{D_i}{\theta^2} + \frac{E_i}{\theta^3})} \times 10^6$. The cross-section ($\sigma_i$) data are from published studies as reported (for details, see Annex 2). The reaction rate coefficient of detachment is taken from *Luque et al.* [2012]. As the reaction rate coefficients depend only on the reduced electric field, they have the same fit functions for all altitudes and they are continuous.

Table 2-9. Electric field driven process reactions and their rate coefficients.

	Reaction	**Reference(s)***	**Fit coefficients (cm^3/s)** $k = e^{(A+B\times\ln(\theta)+\frac{C}{\theta}+\frac{D}{\theta^2}+\frac{E}{\theta^3})} \times 10^6$				
			A	B	C	D	E
	Ionisation						
IN1	$e^- + N_2 \rightarrow N_2^+ + 2e^-$	1	-42.03	1.486	-493.8	2603	-2.544×10^4
IN2	$e^- + N_2 \rightarrow N^+ + N + 2e^-$	2	-40.48	1.111	-2113	6.849×10^4	-2.933×10^6
IN3	$e^- + N_2 \rightarrow N^+ + N(^2D) + 2e^-$	3	-5.052	-3.749	-4791	3.096×10^5	-9.69×10^6
IN4	$e^- + O_2 \rightarrow O_2^+ + 2e^-$	5	-43.89	1.677	-235.3	8094	-1.162×10^5
IN5	$e^- + O_2 \rightarrow O^+ + O + 2e^-$	5	-44.73	1.637	-596.9	-416.6	-1.305×10^5
	Attachment						
AT1	$e^- + O_2 \rightarrow O^- + O$	1	-35.36	-0.344	-89.9	1966	-1.906×10^4
	Dissociation						
DS1	$e^- + N_2 \rightarrow N + N + e^-$	3	-40.51	1.229	-251	5771	-8.938×10^4
DS2	$e^- + N_2 \rightarrow N + N(^2D) + e^-$	3	-40.82	1.275	-237.6	5316	-8.426×10^4
DS3	$e^- + N_2 \rightarrow N + N(^2P) + e^-$	3	-42.75	1.505	-231.3	1230	-2.775×10^4
DS4	$e^- + O_2 \rightarrow O + O + e^-$	6	-38.19	0.8626	-163.9	5845	-6.728×10^4
DS5	$e^- + O_2 \rightarrow O + O(^1D) + e^-$	7	-35.26	0.5619	-128.9	2634	-2.791×10^4
DS6	$e^- + O_2 \rightarrow O + O(^1S) + e^-$	8	-44.61	1.235	-148.9	-5160	3.82×10^4
	Excitation						
EC1	$e^- + N_2 \rightarrow N_2(A) + e^-$	1	-36.88	0.1292	-250.3	7271	-7.754×10^4
EC2	$e^- + N_2 \rightarrow N_2(B) + e^-$	1	-33.78	0.0307	-231.9	5823	-5.984×10^4
EC3	$e^- + N_2 \rightarrow N_2(a'^1) + e^-$	1	-34.63	-0.028	-324.4	7935	-8.097×10^4
EC4	$e^- + N_2 \rightarrow N_2(a^1) + e^-$	1	-35.81	0.3662	-306.4	8103	-8.636×10^4
EC5	$e^- + N_2 \rightarrow N_2(C) + e^-$	1	-32.19	-0.0882	-428.4	7030	-6.059×10^4
EC6	$e^- + O_2 \rightarrow O_2(a) + e^-$	1	-33.51	-0.1455	-89.11	2641	-2.824×10^4
EC7	$e^- + O_2 \rightarrow O_2(b) + e^-$	1	-35.75	-0.0105	-70.61	2280	-2.536×10^4
	Detachment						
DT1	$O^- + N_2 \rightarrow N_2O + e^-$	9	1×10^{-12}				

*(1) *http://jila.colorado.edu/~avp/collision_data/* (downloaded 27 November 2017); (2) *Itikawa* [2006]; (3) *Zipf et al.* [1980]; (4) *Cosby* [1993a]; (5) *Itikawa* [2009]; (6) *Cosby* [1993b]; (7) *Eliasson B and Kogelschatz U* [1986]; (8) *LeClair and McConkey* [1993]; (9) *Luque and Cordillo-Vazquez* [2012].

2.1.4.3 Electron temperature

For the continuity of electron temperatures in strong ionization regions from head to tail of sprite streamers, *Sentman et al.* [2008] considered an electron temperature model based on reduced electric field (θ). This section examines the electron temperature impacts on the BJ streamer discharge simulation by testing ionization and attachment reactions, and by estimating the temperature for BJ streamer discharge processes.

Following *Sentman et al.* [2008], the electron mean energy E_e[eV] depends on θ as:

$$E_e = \begin{cases} 2.31 \times 10^{-2} \times \theta, & \theta < 65 \text{ Td} \\ 3 \times \left(\frac{\theta}{65}\right)^{2.6} / [1 + \left(\frac{\theta}{65}\right)^2], & \theta > 65 \text{ Td} \end{cases} \quad (2\text{-}21)$$

where the electron mean energy-related electron temperature is $T_e(\theta)$ [eV] $= 2 \times E_e/3$. Therefore, the electron temperature for discharge processes is $T_{e+g} = T_g + T_e(\theta)$, where T_g is the background temperature.

This part compares the bulk rate coefficients of ionization and attachment reactions between T_{e+g} and T_g. The simulations were set at 27 km (in the ozone layer) where the catalytic cycle of NO_x is the most efficient to destroy ozone, with $T_g = 223$ K, pressure P=19.7 hPa . The air density was set at 6.42×10^{17} mol/cm^3 , with O_2=1.35×10^{17} mol/cm^3, $N_2 = 5 \times 10^{17}$ mol/cm^3. The θ range evaluated was from 0.02 Td to 600 Td. The θ evolutions of T_{e+g} and $T_e(\theta)$ are shown in Figure 2-7.

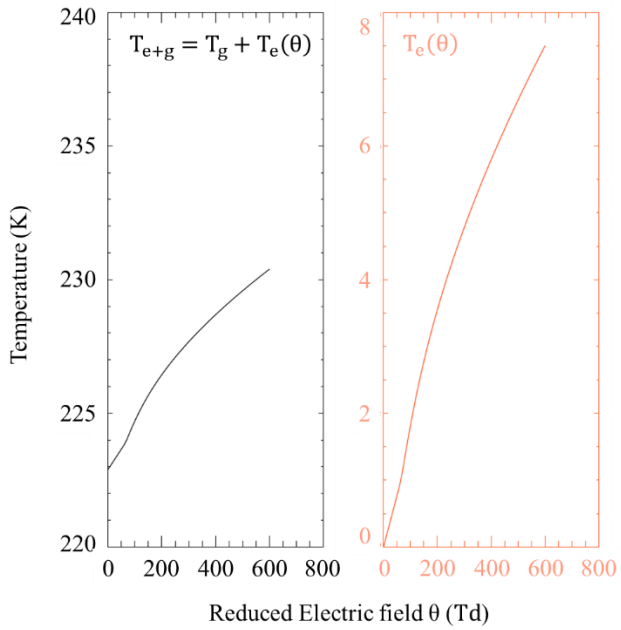

Figure 2-7. The θ evolution of T_{e+g} and $T_e(\theta)$ at 27 km.

Following *Sentman et al.* [2008], the rate coefficients of electron ionization and attachment reactions, which depend on temperature, were calculated. The reactions and their coefficients are summarized in Table 2-10.

Table 2-10. Electron ionization and attachment reactions and their rate coefficients calculated for electron temperature comparison. [*Sentman et al.*, 2008]

Process	$f(E/N)$
$e^- + N_2 \rightarrow N_2^+ + 2e^-$	$\log k = -(8.3 + 365/\theta)$
$e^- + N_2 \rightarrow N^+ + N + 2e^-$	$k = 3.18 \times 10^{-14}(T_e/300)^2 \times \exp(-296266/T_e)$ $T_e = 6 \times 1.16 \times 10^4 \times \theta/615$
$e^- + O_2 \rightarrow O_2^+ + 2e^-$	$\log k = -(8.8 + 281/\theta)$
$e^- + O_2 \rightarrow O^+ + O + 2e^-$	$k = 3.18 \times 10^{-14}(T_e/300)^2 \times \exp(-206055/T_e)$ $T_e = 6 \times 1.16 \times 10^4 \times \theta/615$
$e^- + O_2 \rightarrow O^- + O$	$\log k = -(10.4 + 57/\theta), \theta > 80,$ $= -(9.575 + 123/\theta), \theta < 80$
$e^- + O_2 + O_2 \rightarrow O_2^- + O_2$	$k = 1.4 \times 10^{-29} \times (T/300)^{-1} \times \exp(-600/T)$
$e^- + O_2 + N_2 \rightarrow O_2^- + N_2$	$k = 1.07 \times 10^{-31} \times (T/300)^{-2} \times \exp(-70/T)$

Figure 2-8 displays the θ evaluation of bulk ionization rates with T_g and T_{e+g}. The reactions:

$$e^- + N_2 \rightarrow N_2^+ + 2e^- \quad (2\text{-}22)$$

$$e^- + N_2 \rightarrow N^+ + N + 2e^- \quad (2\text{-}23)$$

are shown as black curves in Figures 2-8a and 2-8b. And the reactions:

$$e^- + O_2 \rightarrow O_2^+ + 2e^- \quad (2\text{-}24)$$

$$e^- + O_2 \rightarrow O^+ + O + 2e^- \quad (2\text{-}25)$$

are shown as purple curves in Figures 2-8a and 2-8b. The coefficients calculated with T_g and T_{e+g} for bulk ionization have no differences.

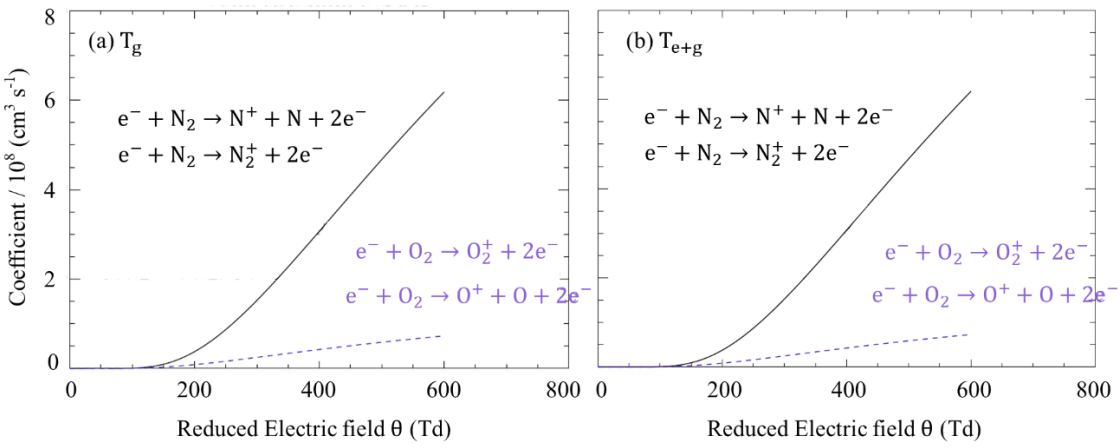

Figure 2-8. Reduced electric field evaluations of bulk ionization rates.
(a) Model calculated with background temperature (T_g)
(b) Model calculated with electron temperature (T_{e+g}).

The θ evaluations of attachment bulk rates with T_g and T_{e+g} are displayed in Figure 2-9. The reaction tested in (a) and (b) is:

$$e^- + O_2 + N_2 \rightarrow O_2^- + N_2 \quad (2\text{-}26)$$

With θ increasing from 0 to 600 Td, the coefficient of T_g is constant (Figure 2-9a), while the coefficient of T_{e+g} decreases from 9.54 to 9 ($\times 10^3$ cm^3 s^{-1}) (Figure 2-9b). For the reactions of

$$e^- + O_2 + O_2 \rightarrow O_2^- + O_2 \qquad (2\text{-}27)$$

$$e^- + O_2 \rightarrow O^- + O \qquad (2\text{-}28)$$

The evolution of θ is shown in Figures 2-9c and 2-9d. The coefficients calculated with T_g and T_{e+g} have no differences. The coefficients are in 10^6 cm^3 s^{-1}, which are 3 orders of magnitude larger than those displayed in Figures 2-9a and 2-9b.

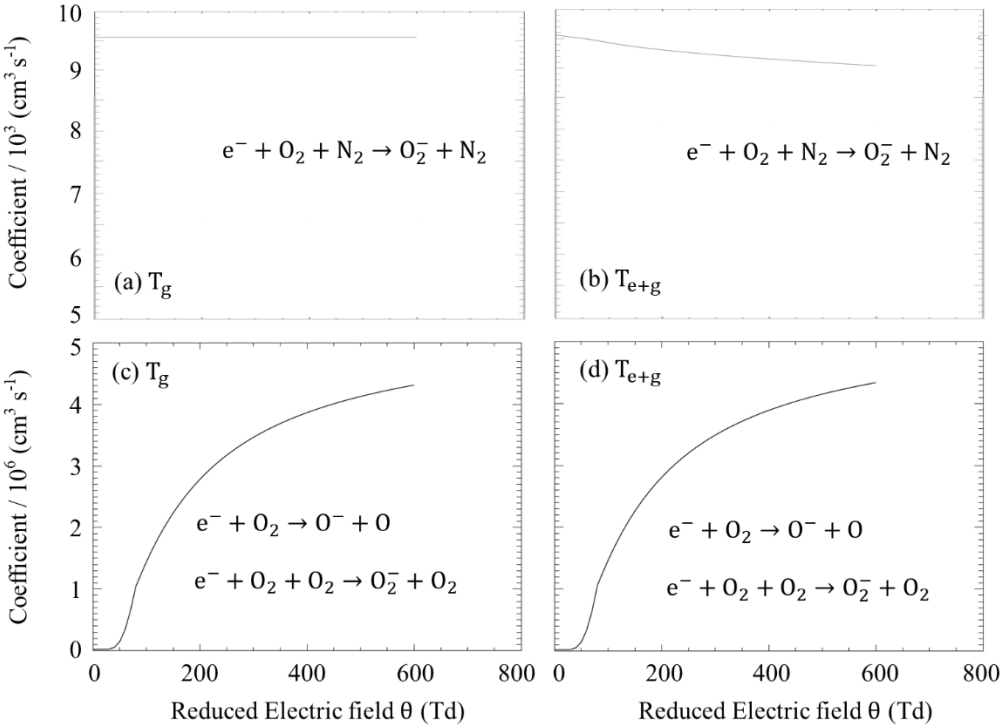

Figure 2-9. Reduced electric field evaluations of bulk attachment rates. (a) and (c) were calculated with background temperature (T_g), (b) and (d) with the electron temperature (T_{e+g}).

Given that the electron temperature does not critically impact on ionization or attachment reaction rates (during discharge processes with only roughly 10%) for the reaction 2-26, this study hereafter uses background temperature (T_g) for all simulations.

2.2 Streamer parameterization

During the streamer discharge, the production and loss of e^- is driven by ionization and attachment processes, which depend on the local electric field. Usually the discharge is parameterized considering a constant pulse electric field [e.g. *Winkler et al.,* 2014, 2015; *Gordillo-Vázquez,* 2008; *Sentman et al.,* 2008]. However, using an electrodynamic streamer model [*Ihaddadene and Celestin,* 2017], it appears that during the streamer passage the electric field of the streamer head varies as a function of time.

In our study the discharge is represented in two ways: a constant electric field pulse and a time variation of the electric field according to realistic simulations from an electrodynamic streamer model.

2.2.1 Pulse streamer parameterization

As in W2015, *Raizer et al.* [2007] and *Mishin et al.* [2008], the discharge associated with the streamer passage is represented by a simple boxcar electric field (rectangular function).

Based on the scaling relations of *Raizer et al.* [2007], the tip electric field of strong streamers [*Mishin and Milikh,* 2008] is taken to be:

$$E = 1.5 \times 10^5 \text{ V cm}^{-1} \frac{N}{N_0} \qquad (2\text{-}29)$$

where N is the local air density, and N_0 the air density at the Earth's surface, in cm^{-3}.

Thus, E/N is independent of altitude:

$$\frac{E}{N} = \frac{1.5\times10^{5}\ \mathrm{Vcm^{-1}}}{N_0} \qquad (2\text{-}30)$$

with $N_0 = 2.5 \times 10^{19}\ \mathrm{cm^{-3}}$. The pulse streamer is constant during the discharge process with the reduced electric field value of $\theta = E/N = 6 \times 10^{-15}\ \mathrm{V\ cm^2}$ (600 Td) for all altitudes. The boxcar reduced electric field is schematically shown in Figure 2-10.

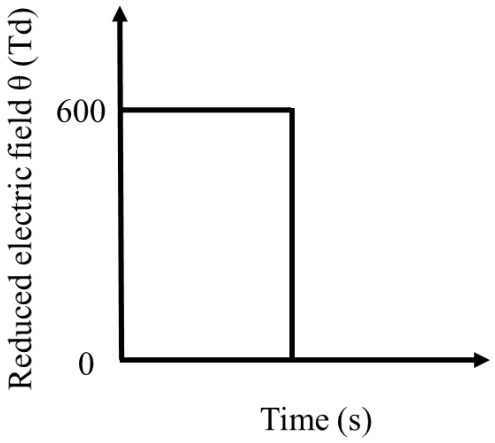

Figure 2-10. A boxcar reduced electric field (rectangular function).

2.2.2 Realistic streamer parameterization

In the present work, the outputs of a plasma fluid model to capture a realistic time dynamic snapshot of the electric field at a given location during the passage of a streamer was used. This electrodynamic model is based on numerical modelling of drift-diffusion equations for charged species coupled with Poisson's equation [e.g. *Ihaddadene and Celestin*, 2015; 2017]. In the case of streamer discharge in air, it is important to note that the electron density formed in the streamer channel reaches a maximum, similar to a saturation process [e.g. *Dyakonov and Kachorovsky*, 1989] on the order of $10^{14}\mathrm{cm^{-3}}\left(\frac{N}{N_0}\right)^2$, where N is local air density and N_0 is air density at the Earth's surface [e.g. *Babaeva and Naidis*, 1996; *Pasko et al.*, 1998].

As the electron density is exponentially dependent on the duration of the applied electric field at a given location, and the MiPO-Streamer model does not solve for the electric field self-consistently, small variations in the rate coefficients would lead to dramatic discrepancies in the electron density in the streamer channel. To circumvent this issue, an analytical fit of the electric field in the streamer head have been calculated. This analytical fit is used in the MiPO-Streamer model in a second step (Figure 2-11).

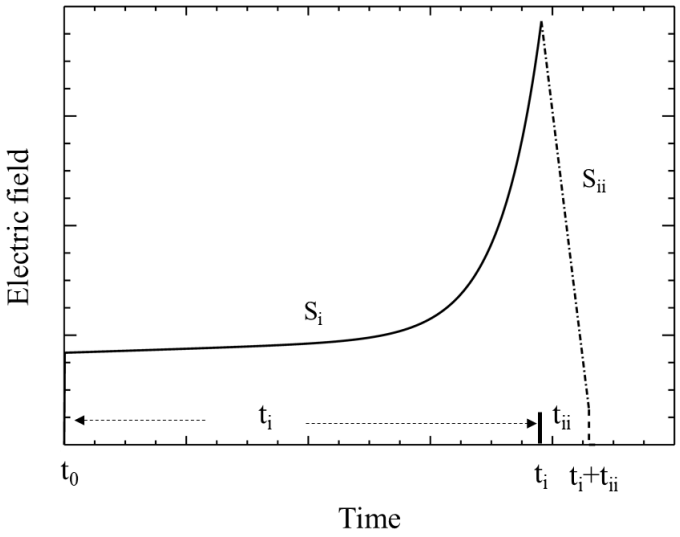

Figure 2-11. Time dependent electric field

At 27 km (in the ozone layer) where the catalytic cycle of NO_x is the most efficient to destroy ozone, the fit of rising electric field (kV/m) obtained from the electrodynamic streamer simulation outputs is:

$$E_{27km\_Si}(t) = 1.078 \times 10^5 \times e^{(2.105\times10^6\times t)} + 3.671 \times e^{(1.473\times10^8\times t)} \quad (2\text{-}31)$$

The electric field rises until the electron density of the streamer channel is reached (this stage is called S_i, the duration is t_i). The resulting difference in the duration of the rising field between the electrodynamic simulation and the MiPO-Streamer model is negligible (as is obvious from Figure 4-5b, where the very sharp slope in the electron density can be seen).

After reaching its maximum, the field is considered to relax linearly in time down to zero over the same timescale (S_{ii} stage, kV/m, duration is t_{ii}) as a fit of:

$$E_{27\ km\_Sii}(t) = -5.834 \times 10^{13} \times (t - t_i) + E_{27\ km\_Si}(t_i) \qquad (2\text{-}32)$$

The electric field fits at other altitudes are obtained by scaling the electric field fit function and the time base at 27 km with altitude:

$$E_{altitude}(t) = E_{27\ km}\left(t \times \frac{N_{altitude}}{N_{27\ km}}\right) \times \frac{N_{altitude}}{N_{27\ km}} \qquad (2\text{-}33)$$

Thus, the reduced electric fields (E/N, θ) at different altitudes have different field duration times (chapter V).

2.3 Summary

A new plasma chemistry model named MiPO-Streamer model have been developed. It includes 117 species and 1760 reactions. Compared to the model used by W2015, the MiPO-Streamer model considers more neutral species that are relevant for representing stratospheric chemistry, including those that involve the bromine family (Br_y), chlorine family (Cl_y), hydrogen species and their corresponding reactions, and more photochemistry of NO_x. The stratospheric O_3 chemistry is particularly perturbed by Cl_y, Br_y catalyzed cycles and by hydrogen-related reactive nitrogen compounds [*Murphy et al.*, 1993].

Two parameterizations are used to represent the BJ Streamer discharge. The first one, widely used in previous studies, considers only an electrical field pulse as a boxcar. The second one developed in this study is based on the results of a realistic modelling approach to streamers using an electrodynamic model, with a time evolution of the electric field during the passage of the streamer head.

Therefore, the simulation of the chemical impact of BJ streamers using the MiPO-Streamer model should be more comprehensive in terms of both plasma chemistry and neutral chemistry.

CHAPTER III

CASE STUDY AND MODEL INITIALIZATION

Contents

Ce chapitre présente le cas de BJ étudié (Section 3.1). Il a été identifié par *Chou et al.* [2011]. L'initialisation du modèle associé (espèces gazeuses initiales et électrons) est présentée dans la Section 3.2.

This chapter introduces the BJ case investigated in Section 3.1. The model initialisations corresponding to the study case, including the initial gaseous species and electrons, are presented in Section 3.2.

3.1 Case study

This thesis chooses to investigate in detail an event reported by *Chou et al.* [2011], which was the first type II gigantic jet observed over a thunderstorm in the Fujian province, China, on 22 July 2007 from the Lulin Observatory (121° E, 23° N) in Taiwan by three sight-aligned WATEC 100-N cameras. During this observation, there were 37 blue jets/starters and a gigantic jet, and 8 sprites recorded. As shown in Figure 3-1a, the red and blue cameras viewed the field between the two red lines. The unfiltered finder camera has a wider field of view between the two black lines. All the jets observed occurred along the two black lines in Figure 3-1b, which were over the smaller thunderstorm 400 km northwest of the observatory. The two white x symbols mark the regions where the jets emerged. The radar reflectivity of these regions was maximum while the jets occurred, as displayed in the regions' radar reflectivity maps at 12:00, 12:30 and 13:00 UTC, shown in Figure 3-2. The maximum radar reflectivity of the convective cell W01 at 12:00 UTC was ~52 dBZ (Figure 3-2a). W01 weakened at 12:30 UTC, while W02 intensified to a maximum radar reflectivity of ~44 dBZ (Figure 3-2b). At 13:00 UTC, the thunderstorm showed weakening reflectivity and it developed an extended anvil region (Figure 3-2c). The processes show the thunderstorm from the mature to the dissipating stage.

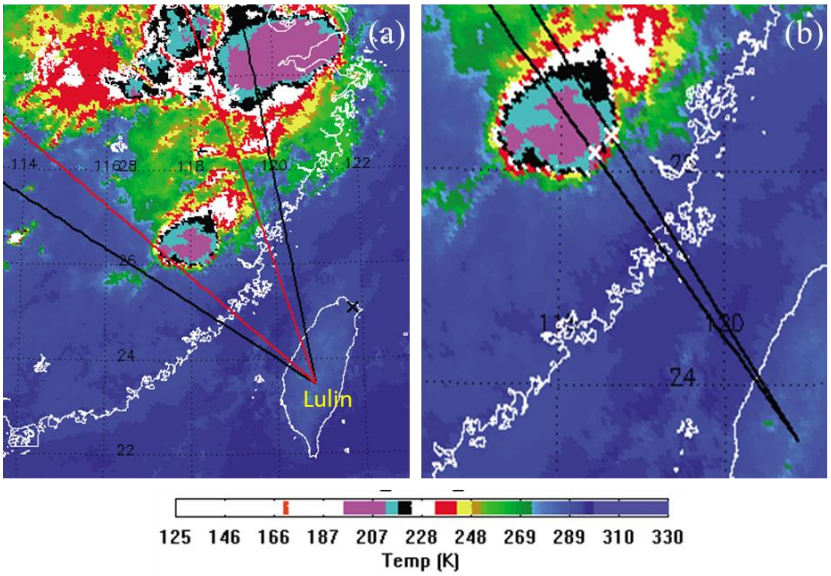

Figure 3-1. MTSAT (Multifunctional Transport Satellite) infrared cloud map on 22 July 2007, 13:00 UTC. [*Chou et al.*, 2011]

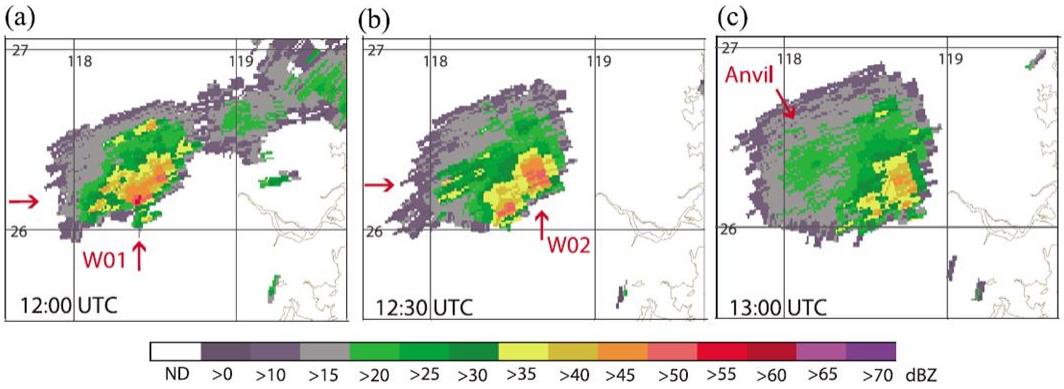

Figure 3-2. Radar reflectivity maps of the thunderstorm regions where jets occurred during the observation period at (a) 12:00, (b) 12:30, and (c) 13:00 UTC, 22 July 2007 [*Chou et al.*, 2011].

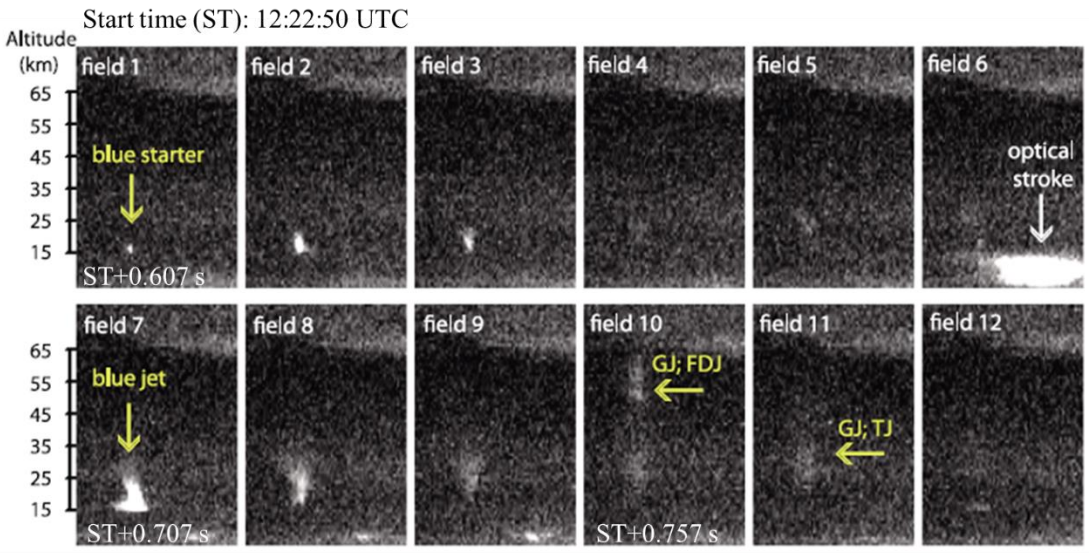

Figure 3-3. Image sequence of type II gigantic jet (GJ) at 12:22:50 UTC from the unfiltered camera. [*Chou et al.*, 2011]

Figure 3-3 describes the sequence of the type II gigantic jet (GJ) at 12:22:50 UTC from the unfiltered camera. At the beginning, a blue starter appeared above a 100 km diameter thunderstorm W01 convective cell (field 1). About 100 ms later, a blue jet occurred near the same cloud top region (field 7). It then developed into a gigantic jet (the fully developed jet, FDJ) reaching an altitude of at least ~65 km in 50 ms (field 10). After this GJ discharge reached the ionosphere, a trailing jet (TJ) rose up from the cloud top to ~35 km and lasted for less than 17 ms (field 11).

Based on the event descriptions, this thesis applies the case parameters of location at (118°E, 26°N) and of time at 12:00 UTC on 22 July 2007.

3.2 Model initialization

3.2.1 Initial profiles of neutral gaseous species distribution

The initial values of temperature, pressure and all gaseous species were calculated using the REPROBUS (REactive Processes Ruling the Ozone BUdget in the

Stratosphere) model. This is a three-dimensional chemistry transport model for characterizing the ozone budget in the stratosphere [*Lefèvre et al.,* 1994] with daily forecasts. Outputs are available on the AERIS data center for altitudes from 0 to 90 km [*http://cds-espri.ipsl.fr/*]. It calculates the temporal evolution of 55 chemical species via 147 chemical reactions, including 26 species explicitly transported (including typically long-lived species in the lower stratosphere, unstable constituents which have a rather long lifetime in darkness) [*Lefèvre et al.,* 1998]. Heterogeneous reactions are also taken into account. The vertical resolution of the REPROBUS model varies from ~1 km near the tropopause level to 2.2 km in the upper stratosphere.

The temperature, pressure and neutral chemical species VMRs deduced from REPROBUS model outputs were used as inputs to the MiPO-Streamer model. The temperature, pressure and total density values used are given in Table 3-1 as a function of altitude.

Table 3-1. Temperature and pressure values as a function of altitude from REPROBUS.

Altitude (km)	Temperature (K)	Pressure (hPa)	N (local air density) ($\times 10^{16}$ cm^{-3})
20	207.14	59.2314	207.06
22	211.13	42.7826	146.73
24	218.578	31.2762	103.61
26	222.658	22.935	74.59
27	222.891	19.7486	64.21
28	224.302	17.0107	54.92
30	227.794	12.5705	39.96
32	229.219	9.37318	29.61
34	231.016	6.99516	21.93
36	236.512	5.21133	15.96
38	246.9	3.96367	11.63
40	255.561	3.03826	8.61
42	259.821	2.34255	6.53
44	260.576	1.81188	5.04
46	259.691	1.40199	3.91
48	258.881	1.08021	3.02
50	259.346	0.830615	2.32

The simulations during daytime (chapter IV) and nighttime (chapter IV and V) are performed. The vertical profiles of chemical species VMR at 12:00 UTC (for the case study of *Chou et al.* [2011], night-time) are displayed in Figure 3-4a and those at 03:00 UTC (for the W2015 case study, noon) are shown in Figure 3-4b.

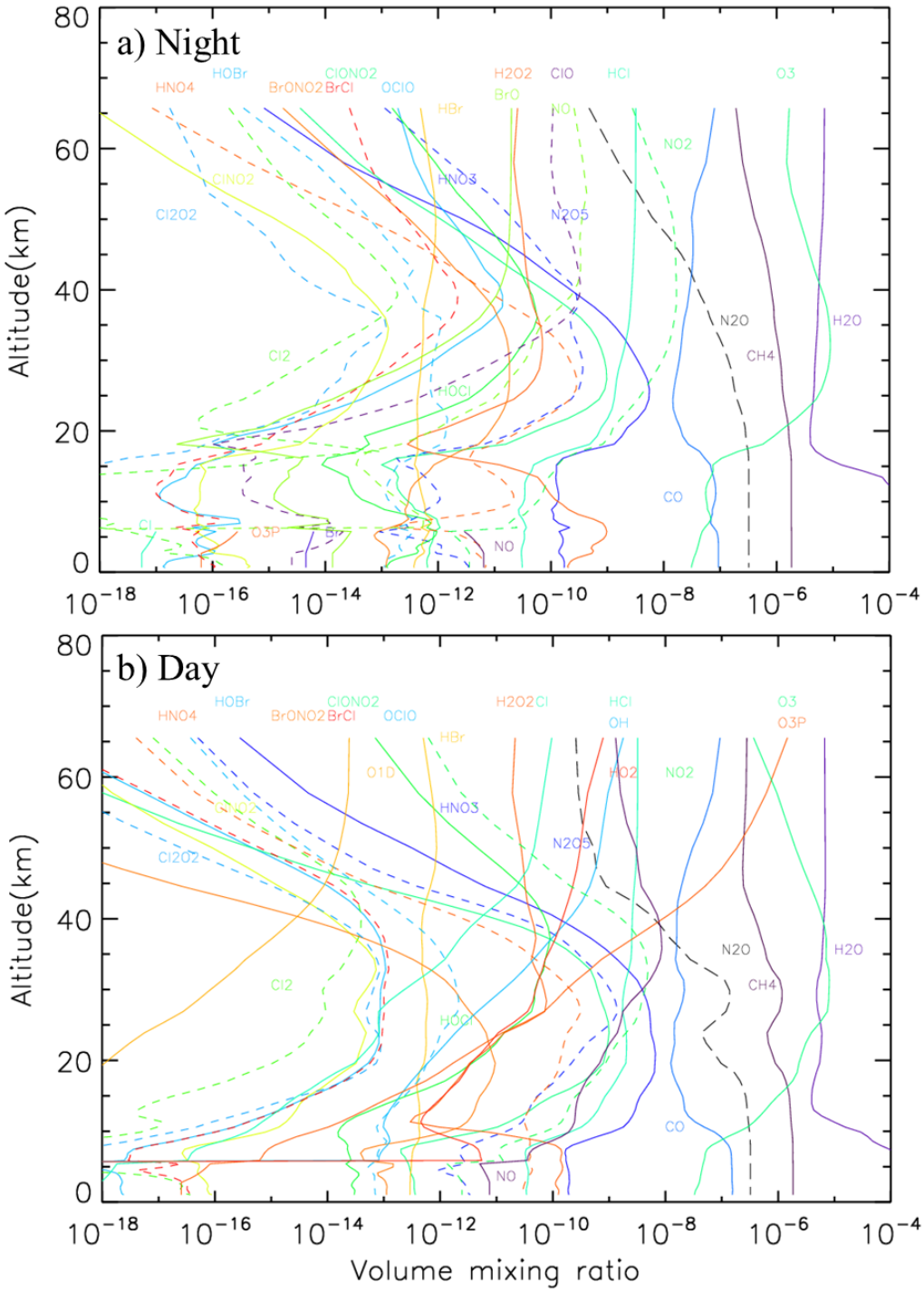

Figure 3-4. The mixing ratio profiles of species from the REPROBUS model at (a) night and (b) day.

From the night-time volume mixing ratio (VMR) profiles, the altitude of the tropopause is ~15 km at mid-latitude. The maximum density of O_3 occurs at ~30 km with the value of ~9 ppm v and the abundant O_3 distributes at the altitude range of 20-50 km. Therefore, this study will estimate the chemical impacts by BJ streamers at

the altitude from 20 km to 50 km. At these altitudes, the reactive species which can cause O_3 depletion display the VMRs of NO_x from 10 ppb v to 10^2 ppb v, of ClO from 10^{-3} ppt v to 10^2 ppt v, and of BrO from 10^{-3} ppt v to 10 ppt v at night-time. The VMR of NO_x increases with the increasing altitude from 20 km to 40 km, then remains the same at the altitude of 40-50 km. The VMR of ClO first increases and then decreases with increasing altitude, and its maximum value occurs at ~40 km. The VMR of BrO increases with the increasing altitude from 20 km to 50 km.

For daytime simulations (Figure 3-4b), the additional chemical species, such as $O(^1D)$, $O(^3P)$, NO, OH, Cl that are produced during the day are also initialized. Like the important reservoir species of Cl and Br, the VMRs of $ClONO_2$ and $BrONO_2$ are larger at night than in daytime.

3.2.2 Initial profiles of electron density

To determine the initial electron density at night time, this study used:

$$N_e = \frac{1.7\times10^{13}}{N} \qquad (3\text{-}1)$$

where N is the local air density, in cm^{-3} [*Mitchell and Hale*, 1973; *MacGorman and Rust*, 1998, p. 34]. The profile is shown in Figure 3-5a. Compared to the initial electron values used by W2015 (Figure 3-5b), the initial values of electron densities used in this study are smaller. For the day time simulation, this study used the same initial values of electron densities as W2015.

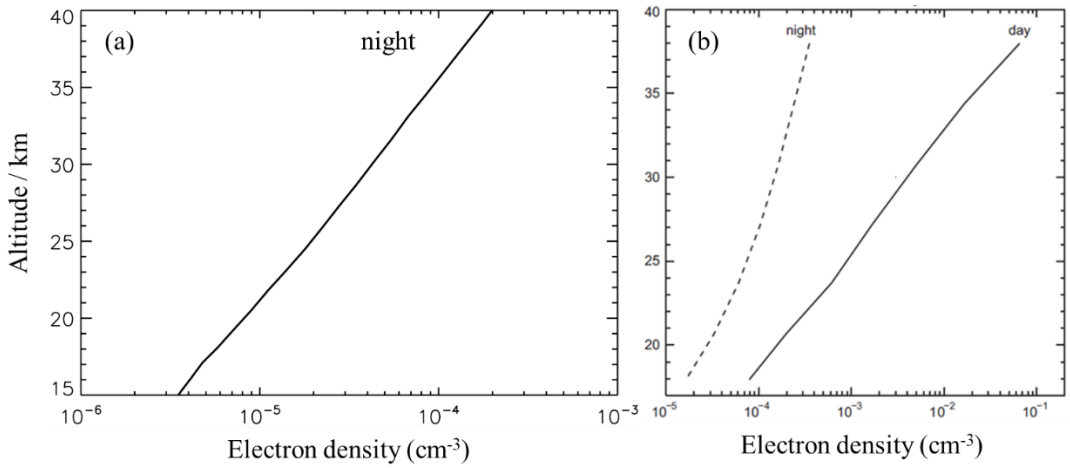

Figure 3-5. The initial electron values (a) at night used by this study, (b) at night and day used by W2015.

To compare plasma chemistry and neutral chemistry results among simulations at the same altitudes, it is necessary to produce the same number density of electrons at the end of the streamer discharge. Following *Raizer et al.* [2007], the electron density at the end of the electric field was calculated as:

$$e_{end} = 10^{14}\text{cm}^{-3}\left(\frac{N}{N_0}\right)^2 \qquad (3\text{-}2)$$

where N is the local air density and N_0 is the air density at the Earth's surface.

CHAPTER IV

MODEL VALIDATION AND EVALUATION BJ STREAMER PARAMETERIZATION

Contents

Dans cette partie, nous nous focalisons sur une étude à 27 km d'altitude dans la couche d'ozone. Nous menons tout d'abord un exercice de validation du modèle de chimie du plasma détaillé (MiPO-Streamer) par comparaison aux résultats de W2015. Pour cette validation comme W2015 (Section 4.1), les simulations sont effectuées de jour et nous utilisons la paramétrisation Pulse streamer pour représenter le champ électrique associé à la décharge.

Puis nous menons une étude détaillée de l'impact de la représentation du champ électrique associé à la décharge en comparant les résultats obtenus avec la paramétrisation pulse streamer et la paramétrisation réaliste du streamer (Section 4.2). Cette partie correspond à l'événement de BJ détecté par *Chou et al.* [2011]. La décharge électrique est initiée durant la nuit. L'analyse des résultats est conduite tout d'abord juste après l'événement au cours des 100 premières secondes pour étudier les perturbations engendrées sur les espèces excités et les ions.

Puis l'analyse est conduite durant les deux jours suivant l'événement afin d'étudier les perturbations engendrées sur les espèces neutres associées à la chimie de l'ozone (oxydes d'azote, chlores et bromes) et l'ozone (Section 4.3).

The objective of our study is the accurate evaluation of the potential impact of blue jet streamers on atmospheric chemistry. As the altitude of 27 km is in ozone layer where the catalytic cycle of NO_x is the most efficient to destroy ozone, the validations and simulations of the new detailed plasma-chemistry (MiPO-Streamer) model at 27 km are performed in this part. Instead of using a reduced electric field with constant value during the blue jet streamer discharge process, a time-dependent reduced electric field coming from an explicit streamer model are used. It includes two investigations under different duration times after the event: firstly, at the small time scale of a few seconds (100 s), to investigate the perturbation of excited species and ions; secondly, at the long time scale of a few days, to investigate the perturbation of the NO_x, bromine and chlorine families, and the induced O_3 modification.

This part first presents the results of the model validation on neutral chemistry and plasma chemistry which are compared to W2015 in Section 4.1. Then, Section 4.2 presents the results obtained of the chemistry impact by electric field parameterization between a simplified pulse streamer and a realistic streamer. The last part (Section 4.3) shows the results of the long-time (two-day) chemistry impact by a realistic streamer.

4.1 Model validation

This part presents the validation results of neutral chemistry and plasma chemistry by the MiPO-Streamer model. All the results are compared to the W2015 study to demonstrate the MiPO-Streamer model validity for neutral chemistry reactions and their rates studies, and its ability to simulate the impact of BJ streamer chemistry.

4.1.1 Neutral chemistry

For neutral chemistry validation, the results obtained considering JPL reaction and photolysis rates are compared to those used in W2015. With the same species and sets

of reactions as W2015, the rate coefficients of neutral chemistry in the MiPO-Streamer model are based on JPL. The reactions that have different rate coefficients between W2015 and JPL are noted in Annex 1. There are no discharge processes considered in this validation part. The model starts during night time (~8 pm, LT) with a two-day simulation, using a time step of 30 s.

Figure 4-1 shows the time evolution of volume mixing ratios (VMRs) of atomic oxygen, NO_2, ClO, BrO, which are the reactive species in the oxygen, nitrogen, chlorine and bromine families. Whatever the version of rate coefficients used, the same shape of diurnal variations and the same order of magnitude for all reactive species are obtained. For atomic oxygen, BrO and ClO, JPL rate coefficients induce a slightly smaller maximum of VMR (not more than 15%). For NO_2, the VMR simulated is greater with the rate coefficients of JPL than with those of W2015 (1.5 ppb v).

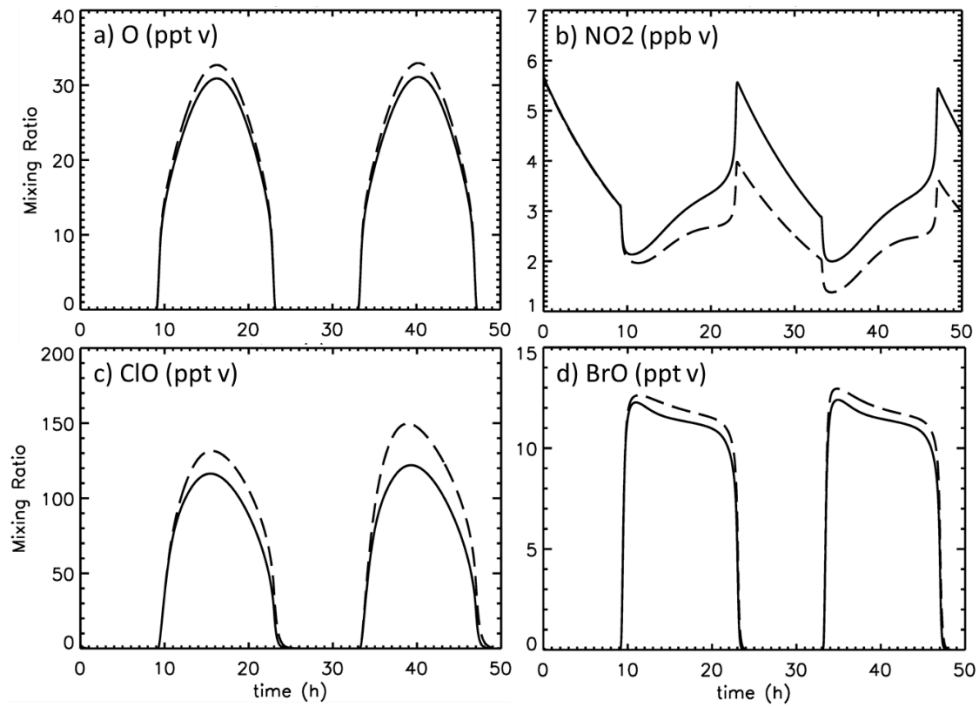

Figure 4-1. Time evolution of volume mixing ratios of (a) atomic oxygen, (b) NO_2, (c) ClO, (d) BrO representative oxygen, nitrogen, chlorine and bromine species, respectively. Rate coefficients of the W2015 version are in dotted line and of JPL in solid line.

The VMR of atomic oxygen with the rate coefficients of JPL is smaller than with those of W2015 (Figure 4-1a), mainly because the rate coefficients of neutral chemistry reactions (15, 16, 19, see Annex 1) from JPL are larger than those from W2015. Meanwhile, the larger rate coefficients of neutral chemistry reactions (16, 19), and the smaller rate coefficient of (25) mean that more NO_2 VMR is produced over the two-day simulation with JPL (Figure 4-1b). There are lower VMRs of ClO and BrO in the MiPO-Streamer model mainly due to their loss processes by NO and NO_2, such as the following chemical reactions:

$$\mathrm{ClO/BrO} + \mathrm{NO} \rightarrow \mathrm{Cl/Br} + \mathrm{NO_2} \qquad (4\text{-}1)$$

$$\mathrm{ClO/BrO} + \mathrm{NO_2} \xrightarrow{\mathrm{M}} \mathrm{ClONO_2/BrONO_2} \qquad (4\text{-}2)$$

Moreover, the diurnal variation of NO_2 with JPL initialization is better in equilibrium than that with W2015, it is not. Since there is no perturbation factor in this neutral chemistry simulation, the diurnal variation of species should be in equilibrium. As the JPL reaction rate coefficients are used and recommended for atmospheric chemistry models, the JPL reaction rates are considered as standard for neutral chemistry.

4.1.2 Plasma chemistry

For the sake of comparison, in the initialization of the plasma chemistry validation part, the initial n_e-, plasma chemistry reactions, rate coefficients, and BJ streamer starting time (03:12:30 UTC, Solar zenith angle ~14°, noon) are set as in W2015. Moreover, the BJ streamer discharge in the MiPO-Streamer model is considered as a boxcar field constant pulse as in W2015.

It is necessary to produce the same n_e- as W2015, in order to compare plasma chemistry and neutral chemistry results to W2015. The same sets of reactions for electric-field-dependant processes as in W2015 are used, and their rate coefficients are calculated by using the BOLSIG+ solver. As the production of electrons grows

exponentially, a small difference in reaction rates leads to a strong change in n_e- and as a consequence in the production of all excited species. Therefore, to obtain the same maximum n_e- as in W2015, the pulse duration is adapted. A 13.12 ns pulse (smaller than the one used in W2015, ~50 ns) is used to produce $n_{e^-}=5.1204\times10^{10}$ cm^{-3}, similar to $n_{e^-}=5.1529\times10^{10}$ cm^{-3} from W2015 [e.g. *Raizer et al.*, 2007]. Scaled to ground-level, this value of n_e- is very close to 10^{14} cm^{-3} [e.g. *Pasko et al.*, 1998], and hence representative of the electron density in a streamer channel.

As in W2015, during the streamer pulse, the density of excited N_2 states increases significantly (Figure 4-2). They are generated by electron impact excitation, radiative and collisional deactivation, and the rapid decay starts at the end of the pulse, due to radiative de-excitation, quenching, and chemical reactions. The shapes, timescales, and values obtained by the MiPO-Streamer model are similar to those of W2015 (see Figure 6 of W2015).

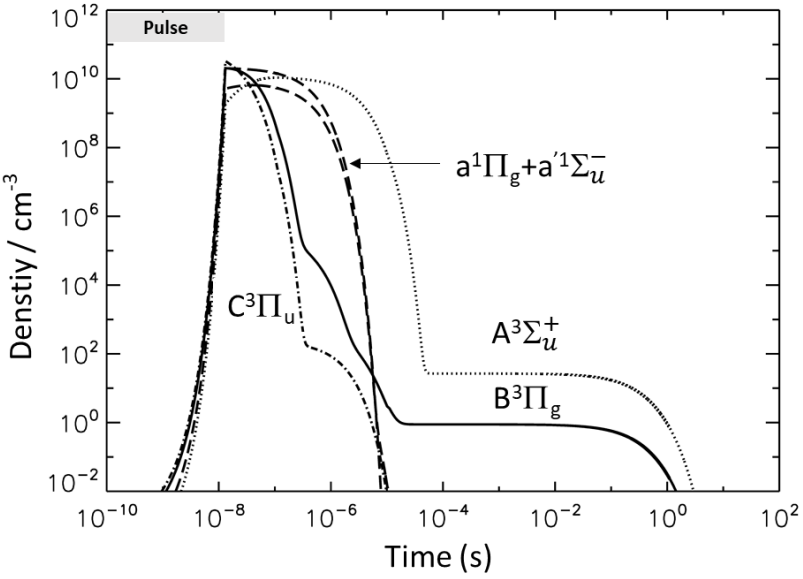

Figure 4-2. Time evolution of excited molecular nitrogen species at 27 km when the streamer pulse occurs.

Compared to W2015, the time evolution of nitrogen species (Figure 4-3a) shows the same shapes and similar densities for the time evolution of N(^{2}D) and N(^{2}P), due to the following reactions :

$$e^- + N_2 \rightarrow N + N(^2D) + e^- \qquad (4\text{-}3)$$

$$e^- + N_2 \rightarrow N + N(^2P) + e^- \qquad (4\text{-}4)$$

The rapid increase in NO density after the electric pulse at 10^{-5} s is caused by the loss of N(^{2}D) and N(^{2}P) by the reactions:

$$N(^2D) + O_2 \rightarrow NO + O \qquad (4\text{-}5)$$

$$N(^2P) + O_2 \rightarrow NO + O \qquad (4\text{-}6)$$

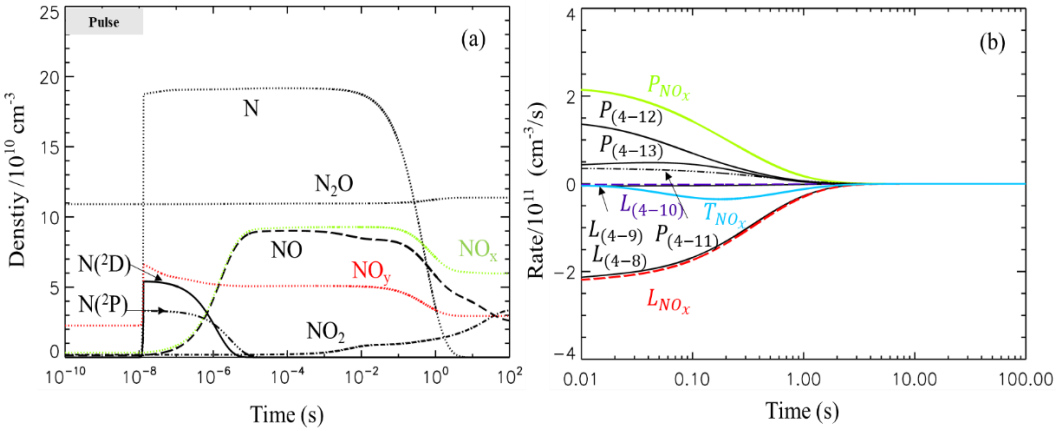

Figure 4-3. (a) Time evolutions of NO and other nitrogen radicals at 27 km when the streamer pulse occurs. The shaded area indicates the time period of the electric pulse. (b) Loss and production rate densities of NO_x associated with reactions (4-8), (4-9), (4-10), (4-11), (4-12) and (4-13) after 10^{-2} s.

The maximum densities of NO and NO_2 are larger than those obtained by W2015 (maximum density of NO ~ 6.25×10^{10} cm^{-3}, of NO_2 ~ 3.2×10^{10} cm^{-3}) and the maximum density of atomic nitrogen is much higher (~19.2×10^{10} cm^{-3}) in our simulation compared to W2015 (~2.2×10^{10} cm^{-3}) at ~10^{-8} s. These differences are not due to reactions (4-3), (4-4), (4-5) and (4-6), because the maximum densities of N(^{2}D)

and N(^{2}P) are similar to those of W2015. The atomic nitrogen (N) is also produced by the dissociation reaction (4-7):

$$N_2 + e^- \rightarrow N + N + e^- \qquad (4\text{-}7)$$

With the rate coefficient at 27 km with $\theta = 600$ Td calculate using the BOLSIG+ solver is 4.56×10^{-9} cm^3/s , a value between those of *Andre* [1997] ($\sim 2.31\times10^{-10}$ cm^3/s) and *Sentman* [2008] ($\sim 4.22\times10^{-8}$ cm^3/s).

Note that whatever the rate considered for reaction (4-7), the density of atomic nitrogen (O) must be greater than the densities of N(^{2}D) and N(^{2}P) due to reactions (4-3), (4-4) and (4-7), which is not the case in W2015. *Feldman and Doering* [1975], *Rees and Jones* [1973] and *Doering et al.* [1975] also reported a higher density of atomic nitrogen compared to the densities of N(^{2}D) and N(^{2}P). The large difference in atomic nitrogen density is due to reaction (4-7).

As in W2015, atomic nitrogen density starts to decrease after 0.01 s mainly due to the reactions:

$$N + NO \rightarrow O + N_2 \qquad (4\text{-}8)$$

$$N + NO_2 \rightarrow O + N_2O \qquad (4\text{-}9)$$

$$N + NO_2 \rightarrow O + O + N_2 \qquad (4\text{-}10)$$

$$N + O_2 \rightarrow NO + O \qquad (4\text{-}11)$$

These reactions lead to the production of atomic oxygen ((4-8), (4-9), (4-10) and (4-11)) and NO (4-11), the loss of NO, NO_2 ((4-8), (4-9) and (4-10)). The loss in atomic nitrogen is also associated with the reactions related to HO_x (odd-hydrogen family) (4-12) and (4-13), which produce NO:

$$N + OH \rightarrow NO + H \qquad (4\text{-}12)$$

$$N + HO_2 \rightarrow NO + OH \qquad (4\text{-}13)$$

Figure 4-3b presents the time evolution of the production and loss rates of NO_x associated with reactions (4-8), (4-9), (4-10), (4-11), (4-12) and (4-13) after 0.01 s. Among these reactions, the total loss rate of NO_x is $L_{NO_x}=-(L_{(4\text{-}8)}+L_{(4\text{-}9)}+L_{(4\text{-}10)})$ (in red), the total rate of NO_x produced is $P_{NO_x}=P_{(4\text{-}11)}+P_{(4\text{-}12)}+P_{(4\text{-}13)}$ (in green) and the net rate of NO_x is $T_{NO_x}=P_{NO_x}+L_{NO_x}$ (in blue). The production of NO_x is mainly due to reactions (4-11), (4-12) and (4-13), and loss of NO_x due to (4-8). The net rate value of NO_x is negative from 0.01s to 2 s, corresponding to the decrease in NO_x during the same period in Figure 4-3a. After 2 s, T_{NO_x} is equal to zero.

The time evolution of the densities of ground state atomic oxygen, excited state $O(^1S)$ and the O_3 change by discharge (ΔO_3) (Figure 4-4a) also present a similar shape to those in W2015. The density of atomic oxygen produced through electric field driven processes is slightly larger in our simulation (~3.7×10^{11} cm^{-3}) than in W2015 (~3.2×10^{11} cm^{-3}). This is mostly due to the small difference in the rate coefficients of electric field driven process reactions. The negative density value of ΔO_3 occurs around 10^{-8} s, due to the increased density of $O(^1S)$ by the reactions:

$$O(^1S) + O_3 \rightarrow O_2 + O_2 \qquad (4\text{-}14)$$

$$O(^1S) + O_3 \rightarrow O(^1D) + O + O_2 \qquad (4\text{-}15)$$

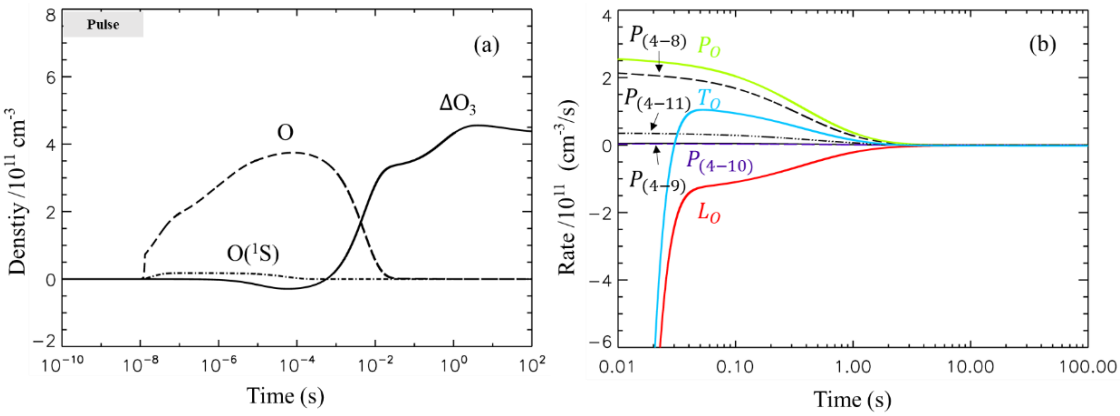

Figure 4-4. (a) Time evolution of densities of ground state atomic oxygen and excited O(^{1}S), ΔO_3 at 27 km. The shaded area indicates the time period of the electric pulse. (b) Loss and production rate densities of atomic oxygen associated with reactions (4-8)-(4-13) after 10^{-2} s.

The density of ΔO_3 starts to increase at 10^{-4} s when the atomic oxygen density decreases through

$$O + O_2 \xrightarrow{M} O_3 \qquad (4\text{-}16)$$

The density of ΔO_3 shows a similar behavior to W2015 until all the atomic oxygen has been consumed at ~0.01 s, after which the density of ΔO_3 rapidly increases until ~3 s. The maximum density of ΔO_3 obtained in our study (~4.56×10^{11} cm^{-3}) is larger than in W2015 (~2.9×10^{11} cm^{-3}), and the maximum density of ΔO_3 is larger than that of atomic oxygen produced during the discharge. Figure 4-4b presents the time evolution of the production and loss rates of atomic oxygen associated with reactions (4-8)-(4-11) after 0.01 s. The total production rate of atomic oxygen is $P_0=P_{(4\text{-}8)}+P_{(4\text{-}9)}+2\times P_{(4\text{-}10)}+P_{(4\text{-}11)}$ (in green), the total loss rate of atomic oxygen is $L_0=L_{(4\text{-}16)}$ (in red) and the net rate of atomic oxygen is $T_0=P_0+L_0$ (in blue). The net rate value of atomic oxygen is positive from 0.03 s to 3 s, corresponding to the increase in ΔO_3 density during the same period, as seen in Figure 4-4a. It means that the ΔO_3 density produced in this part is mainly due to reactions (4-8)-(4-11) with atomic nitrogen, which can produce atomic oxygen. Because of reaction (4-12) and (4-13), the

ΔO_3 density produced from 0.03 s to 3 s (1×10^{11} cm^{-3}) is smaller than the consumed atomic nitrogen density (1.9×10^{11} cm^{-3}). When all the atomic nitrogen has been consumed, O_3 density decreases slowly from 3 s by reaction with nitric oxide (see Figure 4-4a):

$$O_3 + NO \rightarrow O_2 + NO_2 \qquad (4\text{-}17)$$

As displayed above, the plasma chemistry validation results of the MiPO-Streamer model show a good agreement in shape but not in density when compared to W2015. Investigating the sets of reactions in detail, it appears that the atomic nitrogen production is critical for both NO_x and O_3 production.

4.2 Investigation of electric field shape impact

This part performs a comparison of results obtained using a simple electrical field pulse (pulse simulation) and the electric field time evolution, derived from an electrodynamic streamer model [*Ihaddadene and Celestin*, 2017], to represent the streamer.

4.2.1 Initialization

Most BJs are observed at night when convective clouds are in the mature stage. Simulations were therefore performed during night-time starting at a zenith angle of 104°. The initial n_{e^-} used is: $n_{e^-}=1.7\times10^{13}\ N^{-1}cm^{-3}$, N is the local air density [*Mitchell and Hale,* 1973; *MacGorman and Rust,* 1998, p. 34]. As in previous sections, this part focuses on the middle stratosphere at 27 km where reactive nitrogen interacts strongly with ozone.

4.2.2 Reduced electric field

The two electrical field time evolutions considered are presented in Figure 4-5a. For the pulse simulation case, the reduced electrical field θ = 600 Td is considered during 15.57 ns (stage P_i) and then θ = 0 Td (stage P_{ii}). In the case with field obtained from streamer simulation, the electric field shows a slight increase during 60 ns and then a strong increase up to 773.08 Td. The duration of this stage (called S_i) is 78.3 ns. Then, the field decreases exponentially down to 52 Td during 7.9 ns (S_{ii} stage), and then θ = 0 (S_{iii} stage). The total duration of the electrical field perturbation due to the streamer is 86.2 ns.

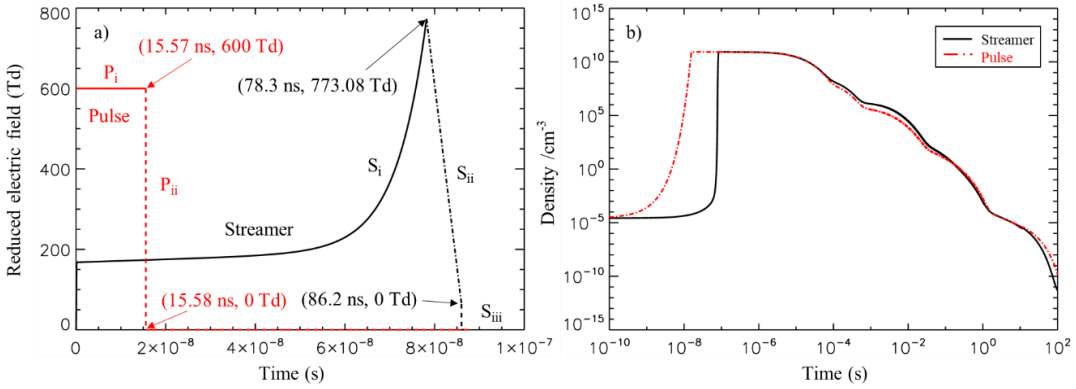

Figure 4-5. At 27 km, time evolution of (a) reduced electrical field θ (Td), (b) electron densities (n_{e^-} , cm^{-3}) with the pulse and simulated streamer cases, respectively in red and black.

As in the previous part, the duration of pulse simulation is adapted to get a similar n_{e^-} (Figure 4-5b) as in the streamer simulation (streamer simulation n_{e^-} is 8.56289×10^{10} cm^{-3} and pulse simulation n_{e^-} is 8.48007×10^{10} cm^{-3}). The decreases in n_{e^-} from the two simulations occur at the same time (~ 10^{-8} s) and are quite similar for both simulations.

4.2.3 Results during the first 100 s

Results obtained for N_2 excited species, atomic oxygen and atomic nitrogen reactive species with both parameterization pulse simulation and streamer simulation are presented in Figure 4-6 during the first 100 s.

For densities of excited N_2 (Figure 4-6a), their time evolutions are roughly similar except for the small delay for the maximum production of each species in the streamer simulation, which comes from the delay of electron production (Figure 4-5b). The de-excitation of N_2 excited species with density values lower than 10^{-10} cm^{-3} occurs in simulation cases at 10^{-5}-10^{-4} s for $N_2(A'^1\sum_u^-)$ and $N_2(a^1\prod_g)$, and at 10 s for $N_2(A^3\sum_u^+)$ and $N_2(B^3\prod_g)$.

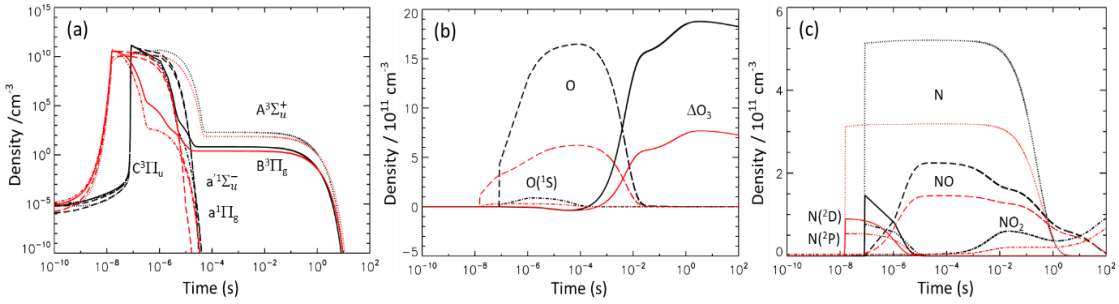

Figure 4-6. Time evolutions in 100 seconds for (a) excited N_2, (b) oxygen, (c) nitrogen family at 27 km from streamer simulation (in black) and pulse simulation (in red). The same line style in each graph indicates the same species.

For atomic oxygen and atomic nitrogen species (Figures 4-6b and 4-6c), the similar small delay for the production of atomic oxygen, O(^{1}S), N(^{2}D), and N(^{2}P) by the streamer simulation is observed, but each time the evolution presents roughly the same shape. Surprisingly, stronger density productions of atomic oxygen, O(^{1}S), N(^{2}D), atomic nitrogen, NO and NO_2 with the streamer simulation are obtained compared to the pulse simulation.

The maximum density values of electron, $N_2(A^3\sum_u^+)$, atomic oxygen, O(^{1}S), ΔO_3, atomic nitrogen, N(^{2}D), N(^{2}P), NO and NO_2 for the two simulations are reported in Table 4-1. Whereas the electron densities produced are similar for both simulations, the maximum density values of $N_2(A^3\sum_u^+)$, atomic oxygen, O(^{1}S), N(^{2}D), and N(^{2}P) are multiplied by a factor ~2 for the realistic streamer simulation case as compared to the pulse simulation case. This impact directly enhances the densities of O_3 and NO_x (NO and NO_2). After 100 s, the O_3 density is higher by a factor of two, and NO_2 density by a factor of 1.5, in the streamer simulation case as compared to the pulse simulation case (Figures 4-6b and 4-6c).

Table 4-1. Maximum densities of electron (e^-), $N_2(A^3\sum_u^+)$, atomic oxygen (O), O(^{1}S), ΔO_3, atomic nitrogen (N), N(^{2}D), N(^{2}P), NO, and NO_2 obtained in the pulse simulation case and in the streamer simulation case at 27 km.

Maximum Density 10^{11} (cm^{-3})	e^-	$N_2(A^3\sum_u^+)$	O	O(^{1}S)	ΔO_3	N	N(^{2}D)	N(^{2}P)	NO	NO_2
Pulse simulation	0.85	0.18	6.22	0.3	7.69	3.19	0.89	0.54	1.45	0.74
Streamer simulation	0.86	0.47	16.48	0.89	18.77	5.21	1.46	0.77	2.25	0.96

4.2.4 Discussion

As seen in the previous section, the time profiles of two types of electric fields have an effect on the oxygen and nitrogen production through the production and heating of electrons. To investigate the differences obtained, as the two simulations had the same maximum n_{e^-}, the density correlations between $N_2(A^3\sum_u^+)$, atomic nitrogen (N), atomic oxygen (O), and electrons are plotted in Figure 4-7, and represent the different sequences of the field evolution (three stages for the simulation-derived streamer, and two stages for the pulse case, see Figure 4-5a).

Figure 4-7 shows the density correlations between $N_2(A^3\sum_u^+)$, atomic oxygen, and nitrogen, and electrons with streamer simulation in black and pulse simulation in red.

The correlation between the densities of $N_2(A^3\sum_u^+)$ and electrons (Figures 4-7a and 4-7b), and densities of $N_2(A^3\sum_u^+)$ in the simulation-derived streamer case is lower than that obtained in the pulse case at the end of S_i (the first stage of streamer field evolution). At this point, the two simulations corresponded to the same n_e- ~ 10^6 cm^{-3}.

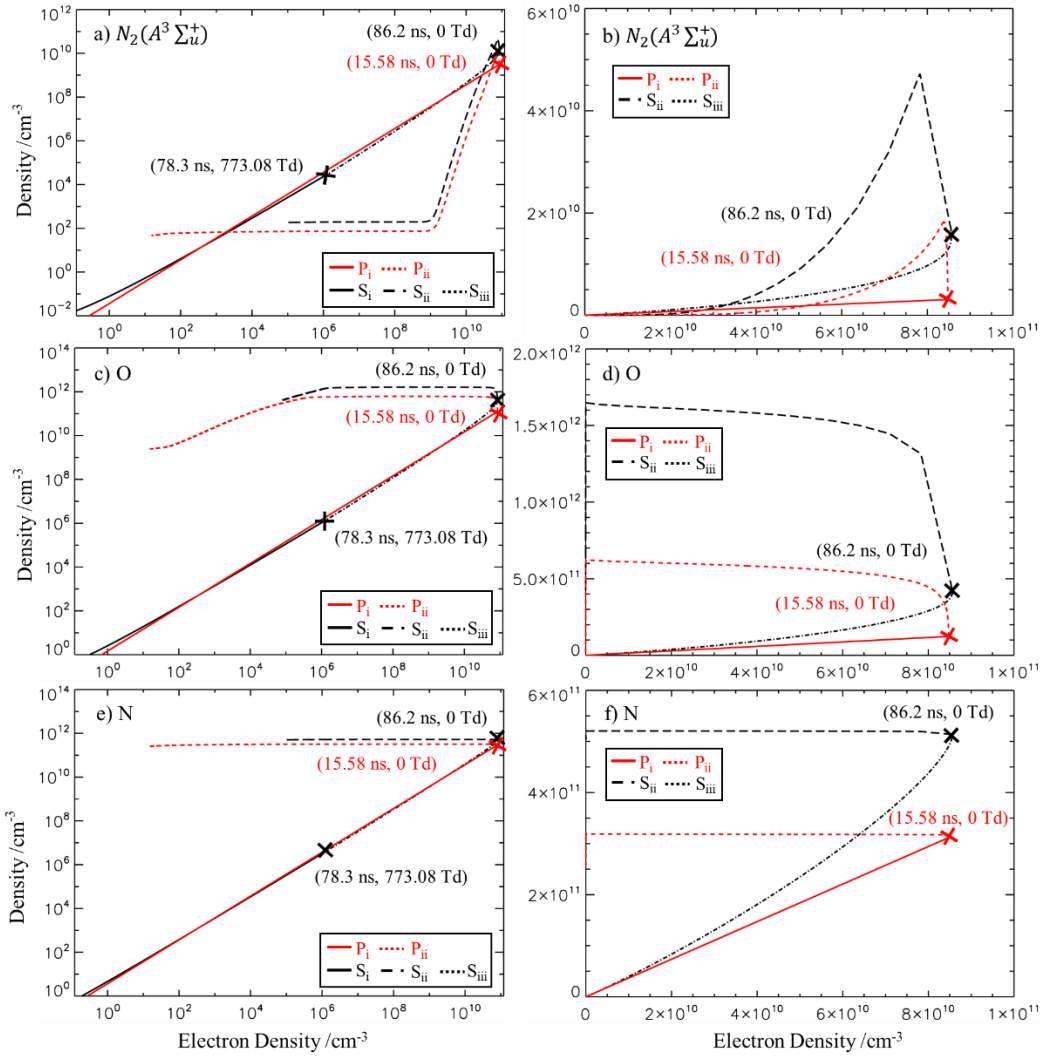

Figure 4-7. Density correlations between $N_2(A^3\sum_u^+)$, atomic oxygen and nitrogen to electrons. Densities for the case of field derived from electrodynamic simulations are shown in black and in red for the pulse simulation. Among them, a), c), e) are in log-log scale and b), d), f) are in linear scale. The sequences of the field are indicated by line-style as in Figure 4-5a.

As the decreasing part of the streamer field (S_{ii}) continues to produce $N_2(A^3\sum_u^+)$ and heat electrons, the $N_2(A^3\sum_u^+)$ density in the streamer simulation case is larger than that in the pulse simulation case when the two simulations obtain a similar maximum n_e-. In order to look at the details close to the maximum of $N_2(A^3\sum_u^+)$ density and explain the difference, its correlation in linear scale is plotted (Figure 4-7b). After n_e- reaches its maximum, $N_2(A^3\sum_u^+)$ density continues to increase for both simulations whereas the field starts to decrease (S_{ii} and P_{ii}). For both simulations, n_e- does not decrease directly with the decreasing field, due to the sets of reactions of associative and Penning ionization:

$$N_2(a'^1\Sigma_u^-) + N_2(A^3\Sigma_u^+) \rightarrow e^- + N_4^+ \qquad (4\text{-}18)$$

This is also due to the characteristic time of

$$e^- + O_2 \rightarrow O^- + O \qquad (4\text{-}19)$$

Moreover, a delay between excited electronic states and the maximum of n_e- in the streamer head was demonstrated by *Celestin and Pasko* [2010] and predicted by *Naidis* [2009]. This is caused by the reaction:

$$e^- + N_2 \rightarrow e^- + N_2(A^3\Sigma_u^+) \qquad (4\text{-}20)$$

which maintains the $N_2(A^3\sum_u^+)$ production density. Moreover, in the simulation-derived streamer field, the increase in $N_2(A^3\sum_u^+)$ density at the end of S_{ii} ($\theta > 0$ Td) is partly impacted by the decreasing electric field. After reaching a maximum in $N_2(A^3\sum_u^+)$ density, the simulation-derived streamer field maintains a higher $N_2(A^3\sum_u^+)$ density than that in the pulse simulation. The maximum value of $N_2(A^3\sum_u^+)$ density from the simulation-derived streamer field is ~3 times larger than that from the pulse simulation case (as shown in Table 4-1). The correlations for density of atomic oxygen and nitrogen to n_e- (Figures 4-7c and 4-7e) are similar to $N_2(A^3\sum_u^+)$ density. The density of atomic nitrogen depends only on field and there is no delay in the production of atomic nitrogen, since there is no related associative and Penning ionization reaction.

4.3 Impact of streamer discharge after two days of simulation

The perturbations of atomic oxygen, NO_2, ClO, and BrO reactive species impacted by streamer discharge during two days at 27 km are analyzed in this part, as well as the time evolution of O_3.

Figure 4-8 shows the time evolution of atomic oxygen, NO_2, ClO, and BrO VMRs during two days with streamer simulation in black, pulse simulation in red and a no-discharge simulation case in blue. These four reactive species present classical diurnal variation with maximum VMRs at noon for atomic oxygen, ClO and BrO, and at night for NO_2.

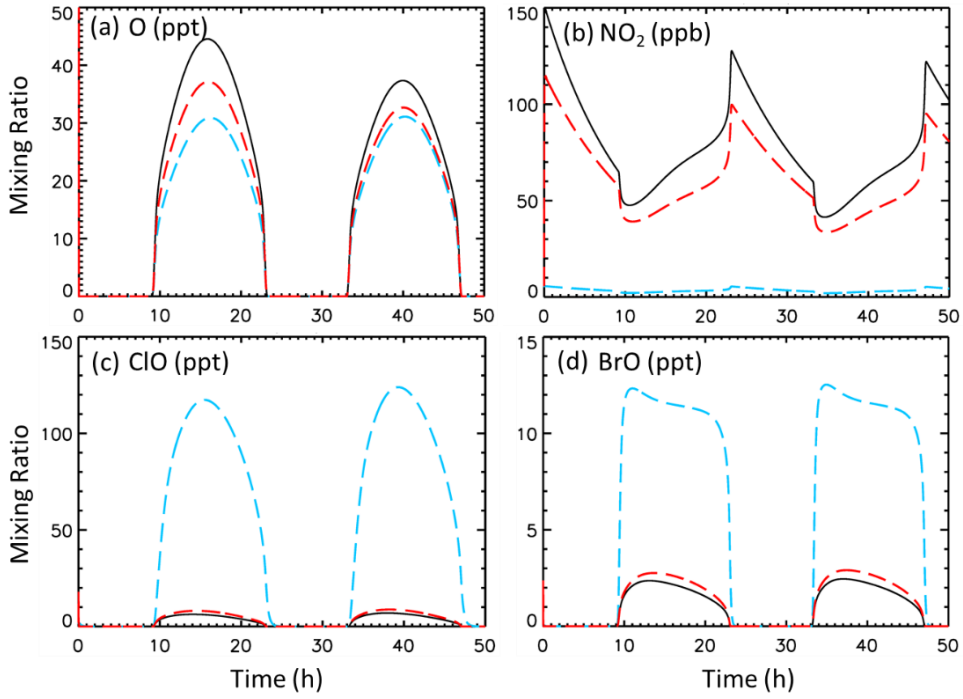

Figure 4-8. Two-day evolutions of VMRs of (a) atomic oxygen, (b) NO_2, (c) ClO and (d) BrO at 27 km with streamer simulation (in black solid line), pulse simulation (in red dashed line) and the no-discharge simulation case (in blue dashed line).

Figure 4-8a shows that the first-day maximum VMR of atomic oxygen with the streamer simulation is 45 ppt v, 37 ppt v for the pulse simulation and 31 ppt v for the

no-discharge simulation case. The additional atomic oxygen VMRs exist in both discharge simulations. On the second day, the atomic oxygen VMRs with streamer and pulse simulations decrease and there are no significant differences with the no-discharge case (streamer simulation ~38 ppt v, pulse simulation ~32 ppt v). Reactive atomic oxygen has a short lifetime and the perturbation of the atomic oxygen VMR time evolution for the streamer simulation is slightly longer than that for the pulse simulation. Figure 4-8b shows that the simulations just after discharge strongly increase the NO_2 VMR (maximum VMR of NO_2 ~150 ppb v by streamer simulation, ~115 ppb v by pulse simulation). The produced NO_2 VMR is 20-30 times higher than that in the no-discharge simulation case (maximum VMR of NO_2 ~5.5 ppb v) and this enhancement of NO_2 VMR is maintained during the two-day simulation. The maximum VMRs of O and NO_2 decrease day by day. The discharge simulations cause non-equilibrium in the neutral gas system (see Figure 4-1). This means that the excess of O and NO_2 VMRs due to discharge are available for chemical reactions.

Figure 4-8c shows that the maximum VMRs at noon (~16 hours after the discharge occurred) of ClO from the discharge simulations (streamer simulation ~7 ppt v, pulse simulation ~9 ppt v) are significantly lower than that in the no-discharge simulation case (~120 ppt v). BrO also showed a lower VMR maximum from the discharge simulations (~2.5 ppt v for streamer simulation and ~2.9 ppt v for pulse simulation) than from the no-discharge simulation (~12.5 ppt v) (Figure 4-8d). There is no significant difference in terms of ClO and BrO VMR values between streamer and pulse simulation results. The difference between discharge simulations and the no-discharge simulation is caused by the excess of NO_2 VMR production (Figure 4-8b), which leads to the production of the reservoir species $ClONO_2$ and $BrONO_2$ through the following reactions:

$$ClO + NO_2 \xrightarrow{M} ClONO_2 \qquad (4\text{-}21)$$

$$BrO + NO_2 \xrightarrow{M} BrONO_2 \qquad (4\text{-}22)$$

The VMRs of $ClONO_2$ and $BrONO_2$ at noon (the maximum value during day-time) in the discharge simulations are larger than those in the no-discharge simulation (~200 ppt v for $ClONO_2$ and ~9 ppt v for $BrONO_2$).

The perturbation in the O_3 VMR during the two-day simulation is shown in Figure 4-9. The variation of O_3 in the streamer simulation case just after the discharge is shown in black, the pulse simulation is in red and the no-discharge case is in blue. The O_3 VMRs at the end of discharge are higher with the streamer simulation (~9.9 ppm v) and the pulse simulation (~8.2 ppm v) than with the no-discharge simulation (~7 ppm v). Due to the discharge, O_3 VMR is increased as a first step.

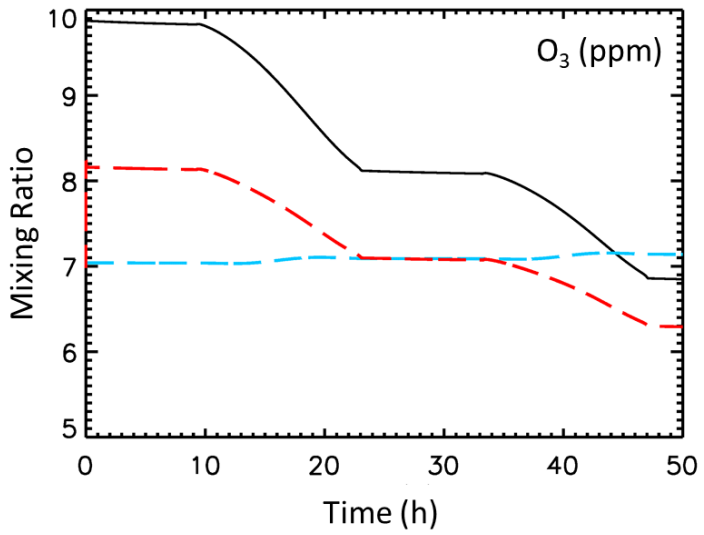

Figure 4-9. The same as Figure 4-8, but for ozone.

Concerning the time evolution during the two-day simulation, O_3 VMRs with streamer and pulse simulations remain constant during the night and decrease during the day. The large amount of NO_x produced by the discharge (Figure 4-8b) leads to the associated catalytic cycle in the stratosphere [*Brasseur and Solomon*, 1986], which is the main mechanism of O_3 destruction in the middle stratosphere (here at 27 km) [*Portmann et al.*, 2012]. Due to the neutral chemistry associated with NO_x production, the enhanced O_3 VMRs caused by the discharge are consumed in the two-day

simulations (45 hours for the streamer simulation, 34 hours for the pulse simulation). After two days, O_3 VMRs in discharge simulations are lower compared to the no-discharge simulation case. The loss of O_3 due to the discharge is slighter for the pulse simulation than that for the streamer simulation.

4.4 Summary and conclusions

A new plasma chemistry model named MiPO-Streamer model is developed. It includes 117 species and 1760 reactions. Simulations were performed at an altitude of 27 km in the middle stratosphere where the maximum O_3 VMR is found.

The neutral chemistry model is validated using rate coefficients with a consistency between initialization and the sets of reactions provided by the JPL. The diurnal variations of reactive species are in equilibrium. The plasma chemistry validation reveals differences in the production of NO and O_3 between the MiPO-Streamer model and W2015. The densities of NO and O_3 depend on the densities of excited states of atomic nitrogen and oxygen, which are mostly produced during the BJ streamer discharge period. Analysis of NO and O_3 production and loss highlights that the major difference is due to the rate coefficient of $N_2 + e^- \rightarrow N + N + e^-$, which produces atomic nitrogen.

The impact of the streamer representation is investigated by using two types of electric field time-profiles, one is a constant field for a limited duration (pulse), which has been previously used in the literature to estimate the chemical impact of TLEs, and the other one is produced through an electrodynamic discharge model. The results on the densities of neutral species through an electrodynamic streamer simulation show an impact of a factor 2 as compared to the pulse-based simulation at 27 km. Analyzing correlations between electrons and $N_2(A^3 \sum_u^+)$, atomic oxygen, and nitrogen species during the discharge process, it is found that the shape of the electric field evolution considered is critical for an accurate estimate of the streamer impact on chemistry.

Higher densities of $N_2(A^3\sum_u^+)$, atomic oxygen, $O(^1S)$, ΔO_3, atomic nitrogen, $N(^2D)$, $N(^2P)$ and NO_x are produced using the more realistic streamer field. Moreover, the higher density of N_2 excited states is directly linked with the light emission density of BJs. This is an important result that could be confirmed by observations. Our results highlight the importance of using a realistic streamer parameterization to model the time-evolution of the electric field.

Looking at neutral chemistry during the first 100 seconds of the simulation, O_3 and NO_x are produced by BJs. Because of the excess of NO_x VMR produced, the two-day simulation reveals that O_3 VMR is destroyed through the NO_x catalytic cycle in the middle stratosphere. The O_3 VMR produced by streamer discharge is consumed in one or two days (depending on the streamer parameterizations considered). After two days, O_3 loss appeared and O_3 VMR decreases to a lower VMR than that in the no-discharge simulation case.

CHAPTER V

CHEMICAL IMPACT OF BJ STREAMER IN THE WHOLE STRATOSPHERE

From 20 km to 50 km

Contents

L'objectif de ce chapitre est d'étudier les perturbations chimiques associées à la décharge d'un BJ streamer en fonction de l'altitude. En effet la Figure 1-4, montre que les taux de perte d'ozone dépendent à la fois de la famille chimique considérée et de l'altitude. Dans cette partie les simulations du modèle MiPO-Streamer sont effectuées tous les 2 km, de 20 km à 50 km. Le cas d'étude considéré est celui de *Chou et al.* [2011] avec une initialisation de nuit. Suite au chapitre précédent, nous utilisons la paramétrisation réaliste de streamer développée pour représenter le champ électrique au cours de la décharge. Dans cette partie, nous analysons les résultats obtenus en comparant systématiquement deux simulations: avec et sans la décharge du streamer de BJ.

The objective of this chapter is to investigate the chemical processes associated with the BJ streamer discharge as a function of altitude. As shown in Figure 1-4, the ozone loss rates depend on both the chemical family considered and the altitude. MiPO-Streamer model simulations are performed every 2 km from 20 km to 50 km, starting during the night as most BJs occur during night-time when thunderstorms are in the mature stage. According to *Mitchell and Hale* [1973] and *MacGorman and Rust* [1998], the initial electron density at night-time is $n_{e^-} = 1.7 \times 10^{13}\ N^{-1}cm^{-3}$, N is the local air density. The initial densities of chemical species are displayed in Figure 3-4. Following on from the previous chapter, the realistic parameterization is used to represent the electric field of the BJ streamer. In this chapter, the results obtained by comparing systematically the two simulations are analysed: with and without the BJ streamer discharge.

5.1 Reduced electric field and electron density

According to *Raizer et al.* [2007], the electron density at the end of the electric field (e_{end}) is on the order of $10^{14}cm^{-3}\left(\frac{N}{N_0}\right)^2$, where N is local air density and N_0 is air density at the Earth's surface. The e_{end} density at each altitude reported in Table 5-1 is deduced from the $e_{\mathrm{end\_27}km}$ density at 27 km by using the scale factor of $(\frac{N_{altitude}}{N_{27km}})^2$. Thus, the e_{end} density decreases as the altitude increases (Table 5-1). This value also constrains the duration of the reduced electric field time evolution at each altitude. Several simulations were performed to adapt both S_i and S_{ii} stages (increase and decrease stages) of the electric field time evolution by successive approximation. The best simulated $e_{\mathrm{s\_end}}$ densities obtained are reported in Table 5-1, as well as the durations of the two field stages.

Table 5-1. The duration times of electric field and maximum electron densities at altitudes from 20 km to 50 km.

Altitude (km)	Reduced electric field duration time (ns)		Calculated maximum electron density ($\times 10^8$ cm^{-3})	Simulated maximum electron density ($\times 10^8$ cm^{-3})
	S_i	S_{ii}		
20	24.3	0.1	8918.85	8536.02
22	34.1	1.9	4478.86	4234.46
24	48.5	2	2233.3	1807.75
26	67.4	3.6	1157.3	1058.36
27	**78.3**	**7.9**	**856.29**	**856.29**
28	91.6	4.8	627.35	623.5
30	125.8	7.2	332	322
32	169.8	8.4	182.4	178.9
34	229.3	10	100	98
36	315.1	11.9	52.96	52.27
38	432.4	14.2	28.11	27.62
40	583.9	16.3	15.42	15.24
42	769.9	18.4	8.87	8.79
44	998.3	20.2	5.27	5.23
46	1284.7	23.9	3.18	3.16
48	1663.3	23.4	1.90	1.88
50	2166.8	24.2	1.12	1.12

Figure 5-1 presents the relative difference between e_{end} (electron density) deduced from the scale factor and simulated electron density $e_{\mathrm{s\_end}}$ at each altitude considered. Most of the relative differences obtained are lower than 10% (absolute value). Note that the increase part of the reduced electric field (S_i) leads to an exponential increase in the electron density (Figure 2-11). This suggests that a small variation in the S_i duration time could lead to a dramatic discrepancy in the $e_{\mathrm{s\_end}}$ value. As shown in Section 4.2.4 above, the decrease part of the reduced electric field (S_{ii}) also contributes to electron production.

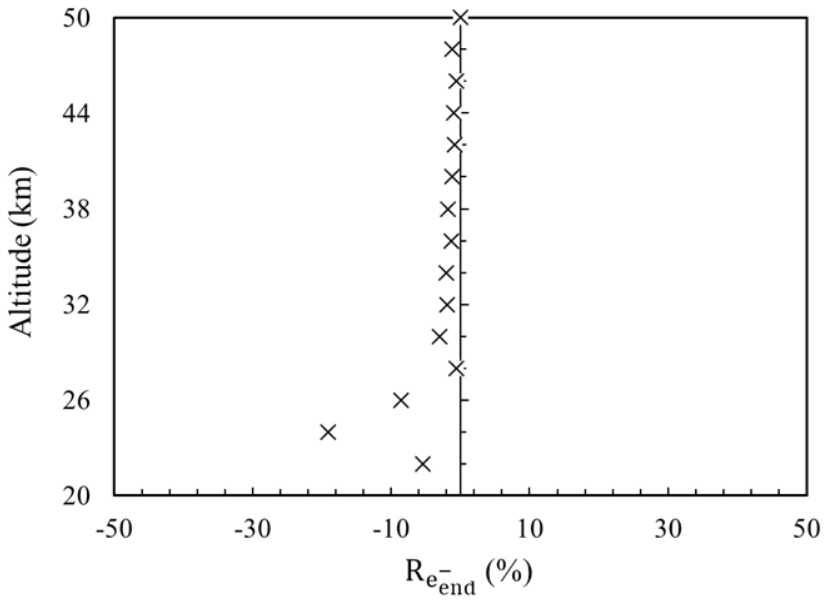

Figure 5-1. Relative differences in the electron densities at the end of the streamer between those deduced from scale factors (calculations) and those obtained from simulations at altitudes of 20-50 km.

The time evolutions of the reduced electrical fields considered and the simulated electron densities at altitudes of 20-50 km are presented in Figures 5-2a and 5-2b, respectively. To obtain the e_{end} at each altitude, the total field duration of both stages at high altitude is longer than those at low altitude. The time evolutions of electron density at all altitudes present the same shape.

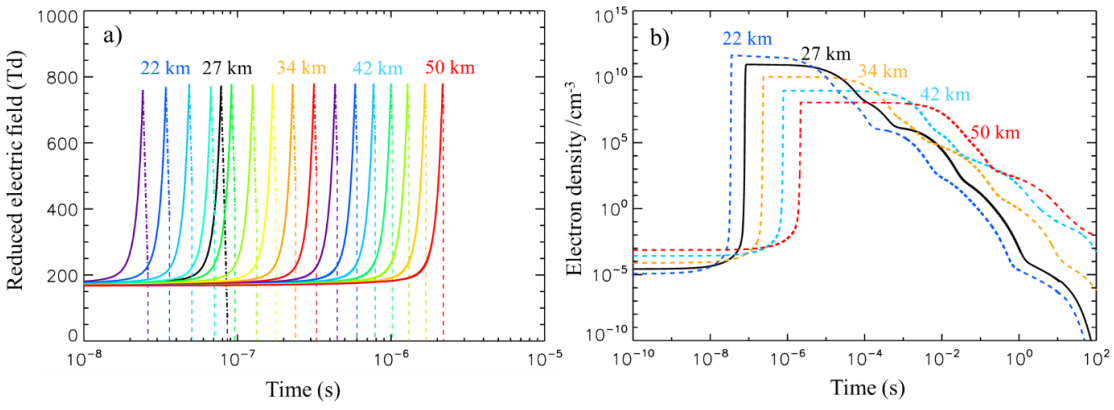

Figure 5-2. Time evolutions of (a) electrodynamic reduced electrical fields (Td), and (b) simulated electron density (cm^{-3}) at altitudes from 20 km to 50 km (every 2 km).

5.2 Impact of BJ streamer on ozone

The impact of the BJ streamer on stratospheric ozone is analyzed by systematically comparing the simulation results obtained with and without discharge at each altitude from 20 km to 50 km (every 2 km). Six time points after the electric breakdown of BJ streamers are selected: 10^{-4} s, 10^{-2} s, 100 s, 12.9 h, 24 h and 48 h. The first three times are selected in order to present the early impacts of BJ streamers, whereas the last three are selected to investigate the interactions between the plasma chemistry induced by the BJ streamers and the neutral chemistry of O_3. Among them, 12.9 h corresponds to daytime (zenith angle is 45°), and 24 h and 48 h to nighttime.

Figure 5-3 shows the vertical profiles of O_3 and atomic oxygen (O) volume mixing ratios (VMR) at the six selected simulation times with and without the BJ streamer discharge (solid lines and dotted lines respectively) at altitudes from 20 km to 50 km.

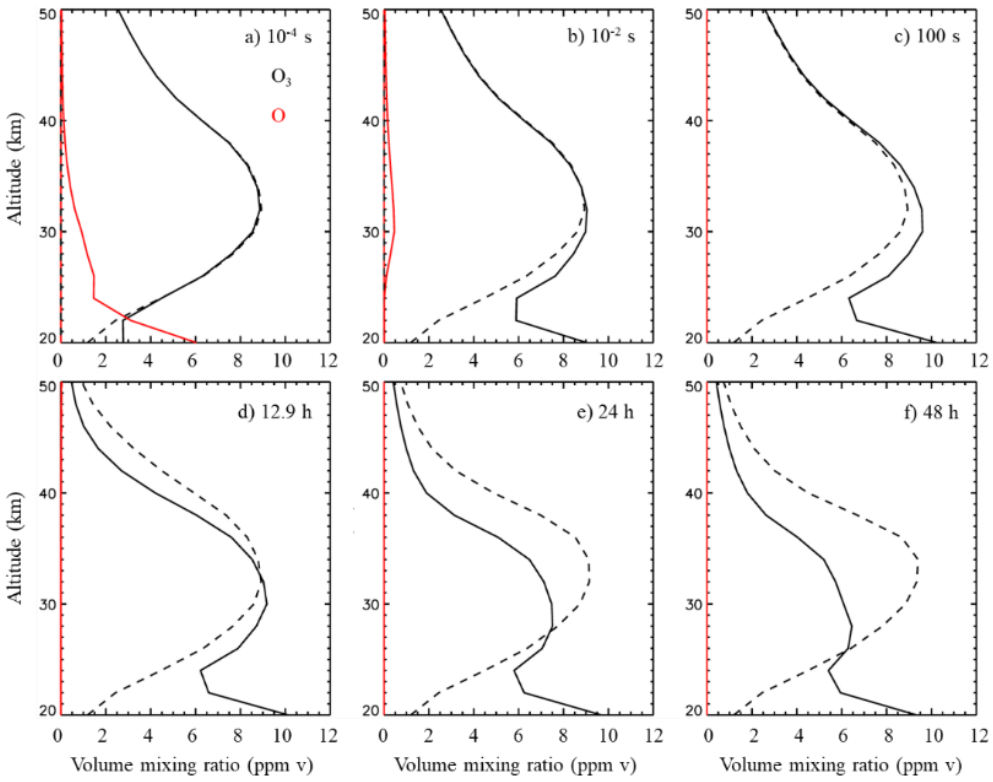

Figure 5-3. Vertical profiles of O_3 (in black) and atomic oxygen (O, in red) volume mixing ratios at altitudes from 20 km to 50 km of six selected simulation times with and without the BJ streamer discharge (solid lines and dotted lines respectively).

Atomic oxygen produced directly by electric driven reactions can be observed at 10^{-4} s and 10^{-2} s. The atomic oxygen VMRs are larger in the lower stratosphere than those in the middle stratosphere, e.g. ~6 ppm v at 20 km and ~1 ppm v at 34 km at 10^{-4} s. No significant production signal of atomic oxygen occurs in the upper stratosphere. Between 10^{-4} s and 10^{-2} s, the O_3 VMRs increase simultaneously with the corresponding atomic oxygen VMR decrease in the low-middle stratosphere (20-40 km). For instance, the consumed atomic oxygen VMR is ~6 ppm v when the O_3 VMR increases from ~3 ppm v to ~9 ppm v at 20 km. This fast conversion of atomic oxygen into O_3 is due to the reaction:

$$O + O_2 \xrightarrow{M} O_3 \qquad (4\text{-}16)$$

At 100 s (Figure 5-3c), compared to the no-discharge simulations, the O_3 VMRs exhibit no obvious perturbations from BJ streamers in the upper stratosphere (~40-50 km), while they are greater in the low and middle stratosphere due to the BJ streamer discharge.

After 12.9 h of simulations (Figure 5-3d, during daytime), O_3 loss appears at the altitudes of ~32-50 km (middle and upper stratosphere). As shown in Figures 5-3e and 5-3f, the O_3 loss at these altitudes increases after 24 h and 48 h of simulation in the middle stratosphere. The excess of O_3 VMRs produced by BJ streamers remains roughly constant after a two-day simulation in the lower stratosphere.

To analyze the O_3 VMR perturbations from the BJ streamer discharge in detail, the O_3 VMR differences (ΔO_3) obtained by simulations with and without discharge as a function of altitude at each selected time are plotted (Figure 5-4).

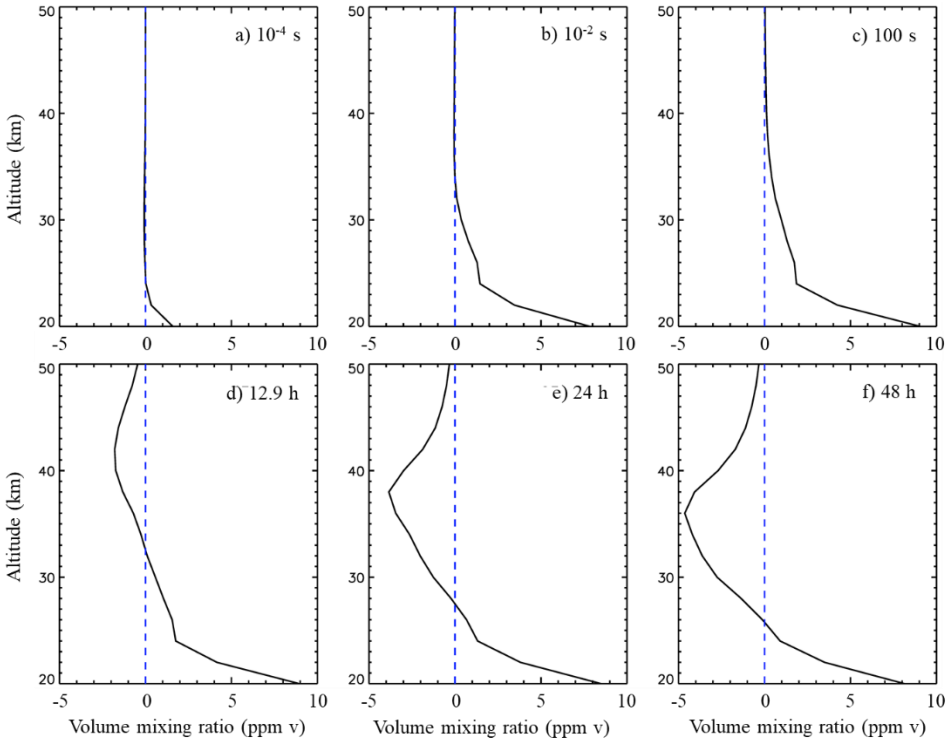

Figure 5-4. Vertical profiles of O_3 VMR differences between with and without discharge of six selected times at altitudes from 20 km to 50 km.

During the first 100 s after the streamer discharge (Figures 5-4a, b, c), the ΔO_3 VMRs are positive at the altitude of 20-40 km, due to the recombination of atomic oxygen produced from discharge processes and the molecular oxygen present. Atomic oxygen can also be formed on account of the atomic nitrogen formed from discharge processes through the sets of reactions:

$$N + NO \rightarrow O + N_2 \qquad (4\text{-}8)$$

$$N + NO_2 \rightarrow O + N_2O \qquad (4\text{-}9)$$

$$N + NO_2 \rightarrow O + O + N_2 \qquad (4\text{-}10)$$

$$N + O_2 \rightarrow NO + O \qquad (4\text{-}11)$$

Negative values of ΔO_3 appear at 12.9 h in the altitude range of 33-50 km. After 24 hours (Figure 5-4e), the maximum O_3 loss is observed at 38 km with a ΔO_3 value of -4 ppm v. After 48 hours (Figure 5-4f), the maximum O_3 loss is located at 36 km with -4.8 ppm v and O_3 loss exists in the altitude range of 26-50 km. This range of

altitude corresponds to the one where O_3 loss by NO_x species is efficient (see Figure 1-4) [*Portmann et al.* 2012]. Note that the O_3 loss rates in Figure 1-4 are based on an ozone layer centered at 28 km, whereas the maximum of ozone is at ~34 km in our study due to the tropical conditions of the case studied. Therefore, all the chemical system in our study, including the efficiency of O_3 loss by NO_x, is shifted to higher altitudes compared to that in Figure 1-4. The O_3 loss caused by BJ streamer in this range of altitude is primarily due to the catalytic cycle with NO_x:

$$O_3 + NO \rightarrow O_2 + NO_2 \quad (1\text{-}8)$$

$$O + NO_2 \rightarrow O_2 + NO \quad (1\text{-}9)$$

$$\text{Net: } O_3 + O \rightarrow 2O_2 \quad (1\text{-}10)$$

5.3 Impact of BJ streamer on the nitrogen family

To better understand the interaction between plasma chemistry and neutral chemistry associated with the nitrogen family, three altitudes at 22 km, 34 km and 42 km are selected. After 48 hours of simulations, O_3 is produced by the BJ streamer at 22 km whereas O_3 is destroyed at 34 km and 42 km. The maximum of ozone is at 34 km in the case studied.

5.3.1 NO_x investigations

The time evolutions of O_3 and NO_x ($NO+NO_2$) at the three selected altitudes are shown in Figure 5-5. The time evolutions of O_3 and NO_x VMRs are very different for the three selected altitudes.

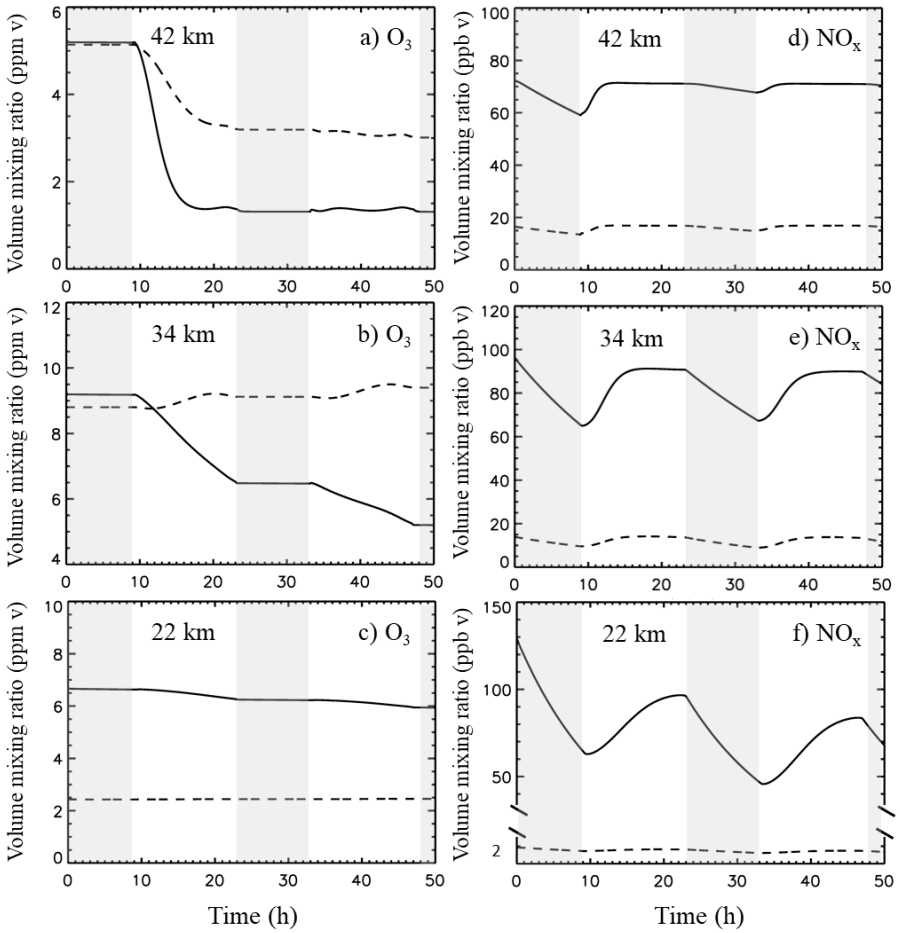

Figure 5-5. Time evolutions of O_3 and NO_x VMRs at 22 km, 34 km and 42 km for BJ streamer simulations (solid lines) and no-discharge simulations (dotted lines). Nighttime periods are in grey.

At 22 km, the O_3 VMR after the BJ streamer discharge is ~6.6 ppm v, while that of the no-discharge simulation is ~2.5 ppm v (Figure 5-5c). The O_3 VMR produced by the BJ streamer decreases slowly down to 6 ppm v during the two-day simulation, while the time evolution of the O_3 VMR from the no-discharge simulation is constant. The NO_x VMR after the discharge is ~130 ppb v, while that of the no-discharge simulation is ~2 ppb v (Figure 5-5f). At this altitude, the NO_x VMRs produced by discharge decrease day by day in the diurnal cycle of the two-day simulation (90 ppb v at the first sunset and 80 ppb v at the second sunset). Clearly, the O_3 and NO_x VMRs produced by the streamer discharge are ~3 times and ~60 times larger than those without discharge at 22 km.

At 34 km, just after the BJ streamer discharge, the O_3 VMR is marginally enhanced from 8.8 ppm v up to 9.2 ppm v (Figure 5-5b). The O_3 VMR time evolution presents a diurnal cycle decreasing during the daytime and unchanging during night-time. The O_3 VMR destroyed during the second daytime is smaller than that during the first daytime, whereas the O_3 VMRs of the no-discharge simulation display enhancements during the two daytimes. Compared to 22 km, the NO_x VMRs at 34 km are consumed less during the diurnal cycle (Figure 5-5e). The level of NO_x produced by the BJ streamer is maintained during the two days of simulation.

At 42 km, the BJ streamer only produces 0.1 ppm v of O_3 VMR (Figure 5-5a). During the first 24 hours, the O_3 VMR decreases to ~3.1 ppm v for the no-discharge simulation, while it decreases to ~1.3 ppm v for the streamer simulation. The NO_x VMRs of the streamer simulation are ~3 times larger (~65 ppb v) than those of the no-discharge simulation (~15 ppb v), and the high NO_x VMRs are maintained during the two-day simulation (Figure 5-5d).

Compared to the no-discharge simulation, the obvious O_3 loss by streamer discharge at 34 km and 42 km is caused by the NO_x catalytic cycle, as the NO_x produced by streamer discharge are maintained. Due to neutral chemistry, the O_3 VMRs decrease critically during the two days of simulations at 34 km and during the first diurnal cycle at 42 km.

5.3.2 Investigations into other chemical species of the NO_y family

To investigate the perturbations induced by the nitrogen oxide family, the time evolutions of N_2O_5 and HNO_3 VMRs are presented in Figure 5-6. These chemical species interact with NO and NO_2 through several sets of chemical reactions (Annex 1), and HNO_3 has longer life time than NO and NO_2 in the stratosphere.

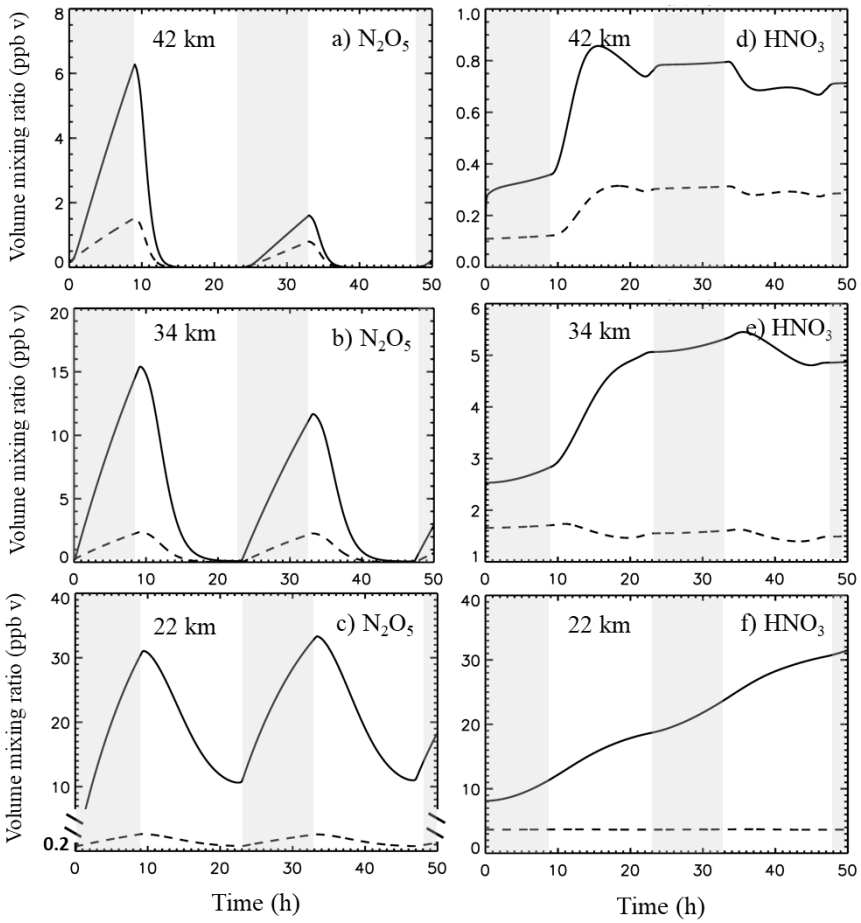

Figure 5-6. As in Figure 5-5, but for N_2O_5 and HNO_3.

Whatever the altitude considered, N_2O_5 and HNO_3 are produced by the BJ streamer discharge. The N_2O_5 production is consumed day after day at 34 km and 42 km, whereas at 22 km the enhancement signal is maintained (Figure 5-6c). At 22 km, HNO_3 increases continuously during both the two daytimes and night-times of simulation (Figure 5-6f). At 34 km and 42 km, the initial production of HNO_3 is strongly enhanced only at the beginning of the first daytime. Then the HNO_3 VMRs stabilize during the night and decrease during the second daytime.

Figure 5-7 presents the changes in the VMRs of O_3, NO_x, N_2O_5 and HNO_3 during the first 24 hours and second 24 hours of streamer simulations at 42 km, 34 km, and 22 km.

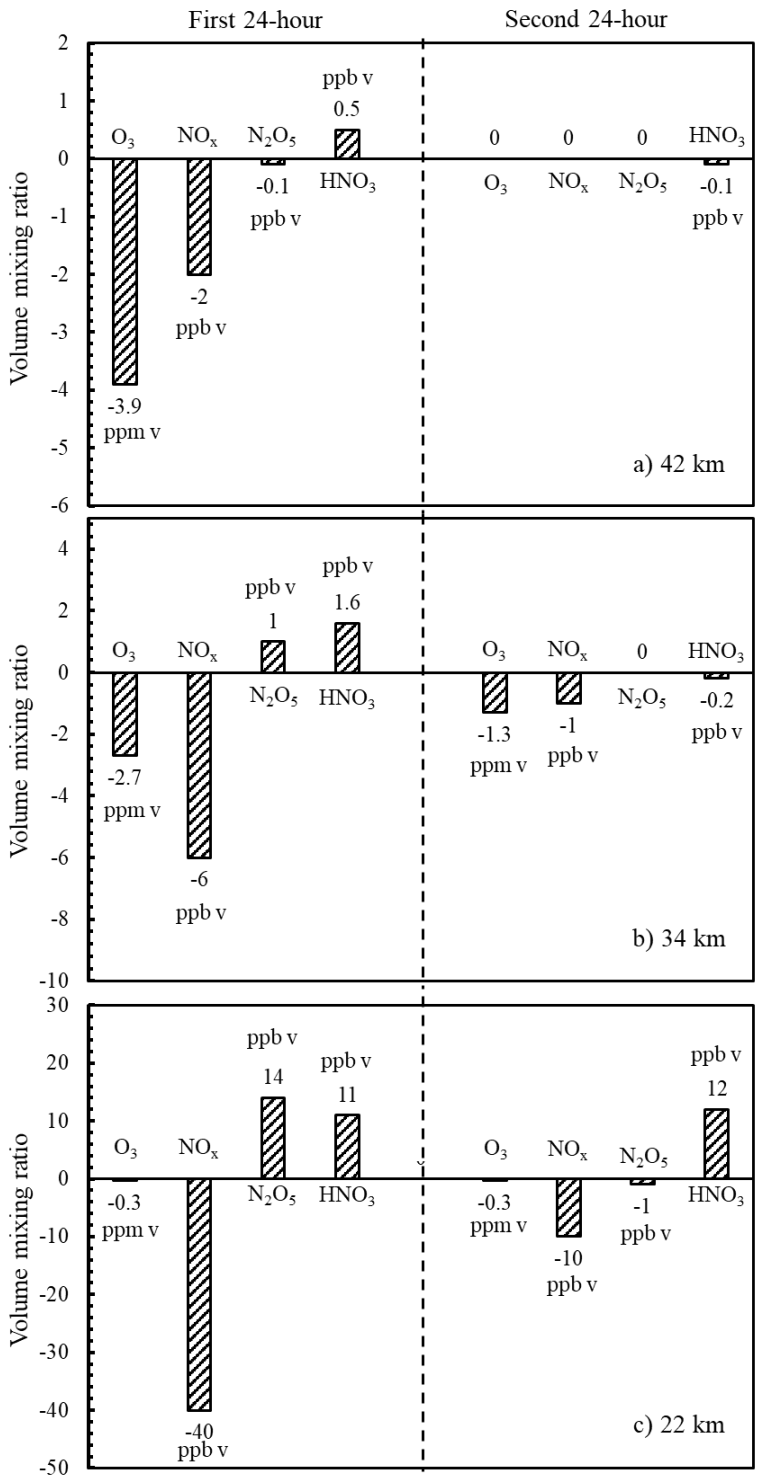

Figure 5-7. Changes in the VMRs of O_3, NO_x, N_2O_5 and HNO_3 during the first 24 hours and second 24 hours of streamer simulations at a) 42 km, b) 34 km, c) 22 km.

At 22 km, during the first 24-hour period (Figure 5-7c), 40 ppb v of NO_x is consumed ($L[NO_x]$). Meanwhile, 14 ppb v of N_2O_5 VMR and 11 ppb v of HNO_3 VMR are produced ($P[N_2O_5]$ and $P[HNO_3]$). As $L[NO_x] \approx 2 \times P[N_2O_5] + P[HNO_3]$， most

of the consumed NO_x are converted into N_2O_5 and HNO_3 through the following reactions:

$$NO_2 + O_3 \rightarrow NO_3 + O_2 \quad \text{only during night-time} \qquad (5\text{-}1)$$

$$NO_2 + NO_3 \xrightarrow{M} N_2O_5 \qquad (1\text{-}22)$$

$$OH + NO_2 \xrightarrow{M} HNO_3 \quad \text{only during day-time} \qquad (5\text{-}2)$$

$$N_2O_5 + H_2O \rightarrow 2\,HNO_3 \qquad (5\text{-}3)$$

The NO_x produced by the BJ streamer discharge are mainly converted to N_2O_5 and HNO_3 at 22 km and they have little impact on O_3.

During the first 24-hour period, at 34 km, $L[NO_x]$ is ~6 ppb v, $P[N_2O_5]$ is ~1 ppb v, and $P[HNO_3]$ is ~1.6 ppb v (Figure 5-7b), and at 42 km, $L[NO_x]$ is ~2 ppb v, $L[N_2O_5]$ is ~0 ppb v, and $P[HNO_3]$ is ~0.5 ppb v (Figure 5-7a). Compared with the results at 22 km, the NO_x are consumed more slowly as the altitude increases. Regarding the budget at these altitudes, $L[NO_x]$ is greater than $2\times P[N_2O_5]+P[HNO_3]$, the excess of NO_x produced by the BJ streamer discharge contributes less to the production of N_2O_5 and HNO_3, and it probably contributes to other reservoirs. At these two altitudes, the production/loss of NO_x, N_2O_5 and HNO_3 during the second 24 hours is very small. This indicates that a new "equilibrium" is reached in the NO_y family with a higher NO_x content from the BJ streamer discharge.

5.4 Impact of BJ streamer on other chemical species

The time evolutions of reactive chlorine ClO_x (=Cl+ClO), bromine BrO_x (=Br+BrO) and hydrogen HO_x (=OH+HO_2) at 22 km, 34 km and 42 km are presented in Figure 5-8. These chemical species present diurnal variations. All the VMRs obtained considering the BJ streamer discharge are smaller than those without discharge, particularly for ClO_x and HO_x chemical species.

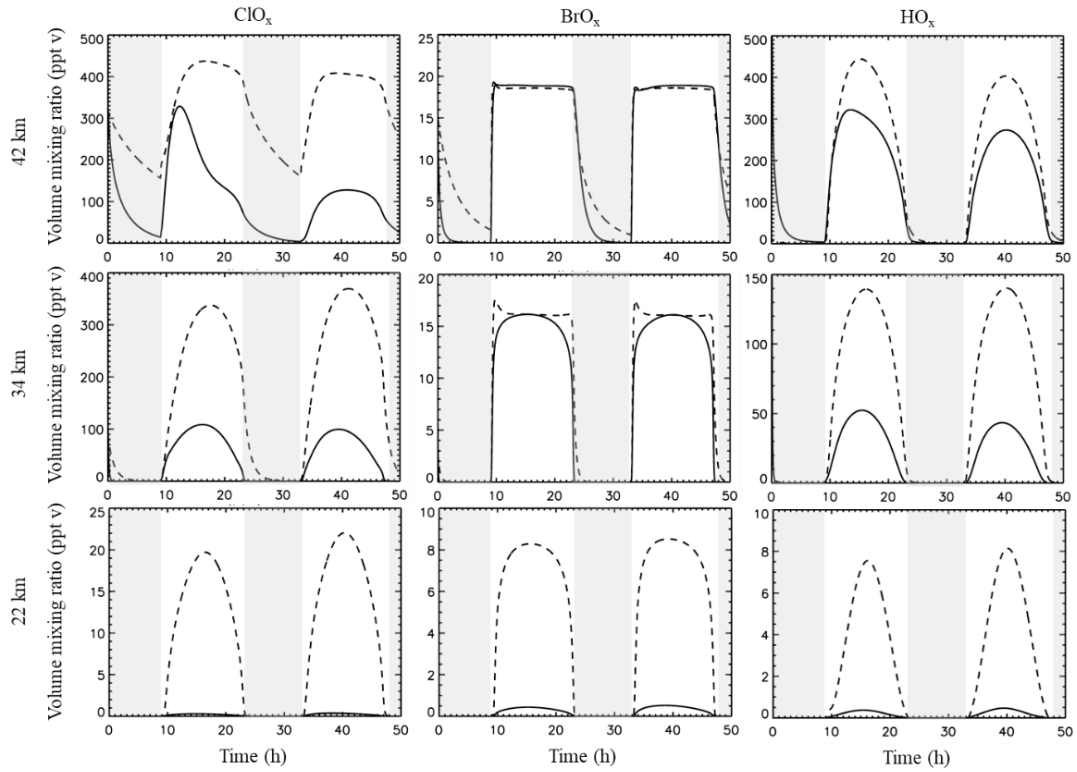

Figure 5-8. As in Figure 5-5, but for ClO_x, BrO_x and HO_x.

The NO_x chemical species interact directly with the reactive chlorine, bromine and hydrogen through the following reactions:

$$ClO_x/BrO_x + NO_x \xrightarrow{M} ClONO_2/BrONO_2 \qquad (5\text{-}4)$$

HO_x in part controls the amount of HCl and HBr through:

$$ClO_x/BrO_x + HO_x \rightarrow HCl/HBr \qquad (5\text{-}5)$$

The chlorine and bromine families interact together through:

$$BrO + ClO \rightarrow Cl + Br + O_2 \qquad (1\text{-}16a)$$

$$BrO + ClO \rightarrow BrCl + O_2 \qquad (1\text{-}16b)$$

$$BrO + ClO \rightarrow OClO + Br \qquad (1\text{-}16c)$$

The VMRs of NO_x chemical species are in ppb v, whereas the VMRs of ClO_x, BrO_x and HO_x reactive species are in ppt v. The excess of NO_x due to the BJ streamer discharge leads to a very fast conversion of ClO_x/BrO_x and HO_x into $ClONO_2/BrONO_2$

and HCl/HBr reservoirs. Figure 5-9 shows the time evolutions of $ClONO_2$ and $BrONO_2$ VMRs at the altitudes selected.

The BJ streamer early impacts on the $ClONO_2$ produced. Then the $ClONO_2$ VMRs produced are destroyed day by day at 42 km (Figure 5-9a) and 34 km (Figure 5-9b), while a very small production occurs at 22 km (Figure 5-9c). However, for $BrONO_2$ VMRs, their loss occurs after the BJ streamer discharge and then they are produced day by day. At 22 km, the diurnal variations of $ClONO_2$ and $BrONO_2$ have almost disappeared due to the BJ streamer discharge. At 34 km and 42 km, the $ClONO_2$ reservoir is reduced and the $BrONO_2$ reservoir is enhanced after two days of simulations.

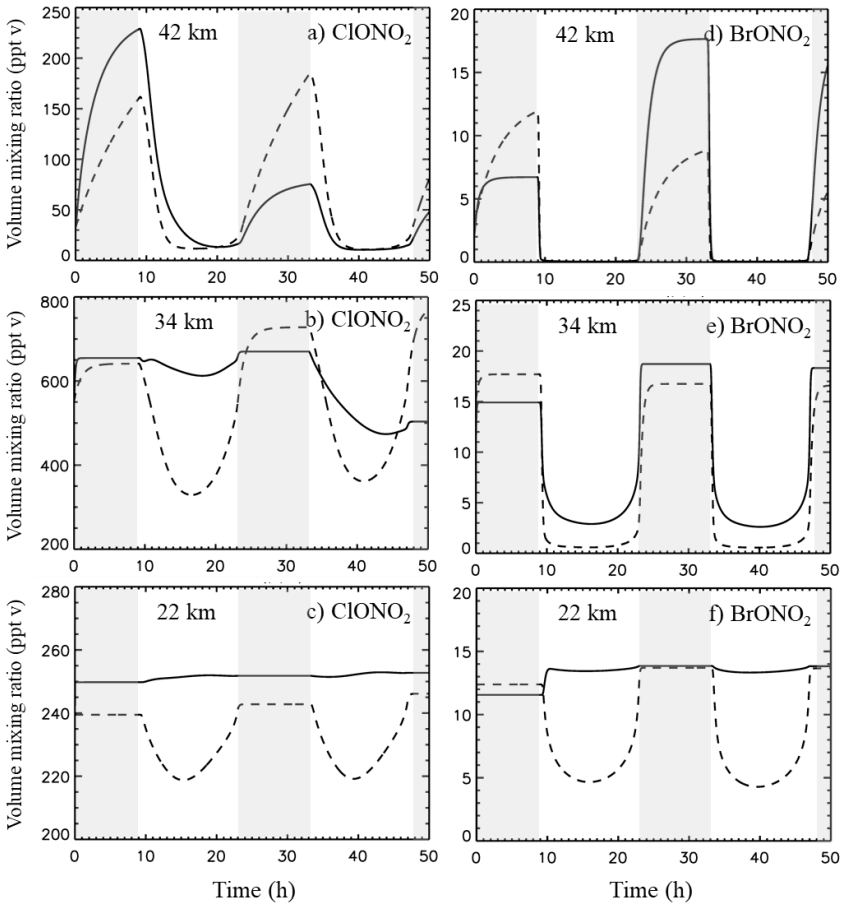

Figure 5-9. As in Figure 5-5, but for $ClONO_2$ and $BrONO_2$.

Figure 5-10 shows the time evolutions of HCl and HBr VMRs at the three selected altitudes. The HCl and HBr abundances are smaller considering the BJ streamer

simulation at 22 km, while those at 34 km and 42 km increase strongly during the first daytime. During the second daytime, the HBr content is reduced at 34 km and 42 km (Figures 5-10d and 5-10e). In the middle and upper stratosphere after two days of simulations, the HCl and HBr VMRs remain greater than those obtained with the no-discharge simulations (Figures 5-10a, b, d, e).

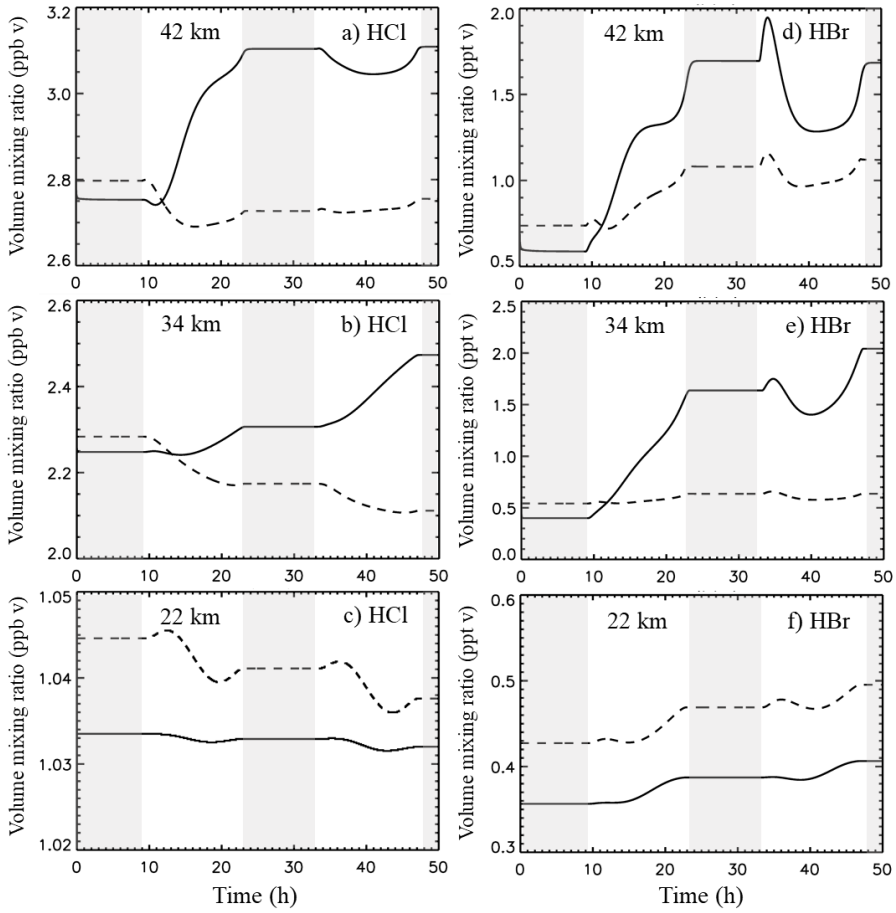

Figure 5-10. As in Figure 5-5, but for HCl and HBr.

Figure 5-11 presents the difference in ClO_x, BrO_x, HO_x, $ClONO_2$, $BrONO_2$, HCl and HBr VMRs between the discharge and the no-discharge simulations at 42 km, 34 km, and 22 km. As the reactive species ClO_x, BrO_x and HO_x are abundant in daytime, the differences at 16 h and 40 h (LT is 12:00) are investigated. Because the chemical processes of the bromine family are the same as those of the chlorine family, and the former is less abundant than the chlorine family in the stratosphere, therefore the chlorine family will be discussed in the following.

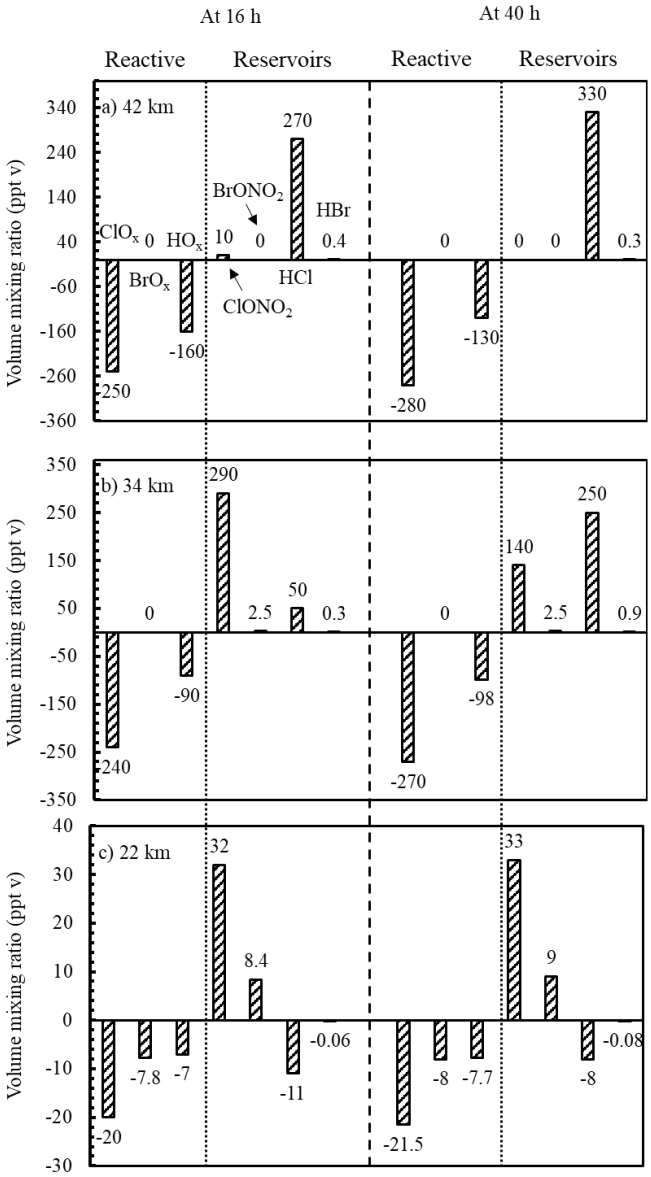

Figure 5-11. The ClO_x, BrO_x, HO_x, $ClONO_2$, $BrONO_2$, HCl and HBr VMRs differences between the discharge and the no-discharge simulations at 16 h and 40 h (corresponding to 12:00 LT) for altitudes of 42 km, 34 km, and 22 km.

Less ClO_x and HO_x exist at both 12:00 LT of the BJ streamer simulation. This is particularly evident in the upper stratosphere.

At 22 km, the $ClONO_2$ reservoir is enhanced by the BJ streamer (Figure 5-11c), while ClO_x and HO_x reactive species are reduced. The ClO_x reactive species are converted into $ClONO_2$ (reaction 5-4) due to the NO_x production associated with the BJ streamer discharge. As large amounts of atomic oxygen are produced by the

discharge at this altitude, the HCl content is reduced by the BJ streamer through the reactions:

$$HCl + O \rightarrow Cl + OH \qquad (5\text{-}6)$$

$$HCl + OH \rightarrow Cl + H_2O \qquad (5\text{-}7)$$

The mechanisms producing $ClONO_2$ and reducing HCl abundance persist at the second daytime.

At 34 km, both $ClONO_2$ and HCl VMRs are enhanced whereas ClO_x and HO_x VMRs are reduced (Figure 5-11b). These reactive species are converted into reservoirs through reactions 5-4 and 5-5 during the two days.

Compared to those at lower altitudes, the smaller values of ClO_x and HO_x VMRs and the higher value of HCl VMR in the streamer simulation at 42 km highlights that ClO_x and HO_x mainly contribute to HCl production by reaction 5-5 (Figure 5-11a). Moreover, the O_3 loss rates due to ClO_x and HO_x at 42 km are very efficient (Figure 1-4), their smaller values in the BJ streamer simulation reduce their contributions to the O_3 loss at this altitude. The conversion of ClO_x and HO_x reactive species into HCl reservoir specie persist during the second day.

These $ClONO_2$, HCl and $BrONO_2$ chemical species enhancements due to the BJ streamer discharge in the middle and upper stratosphere are important, because these reservoir species have long lifetimes (HCl is ~2 years) in the stratosphere and they can be transported over long distances and be reactivated later to destroy ozone.

5.5 Summary and conclusions

The detailed investigations in the whole stratosphere of the BJ streamer discharge impact on the chemical system are performed.

The increased atomic oxygen VMRs by the BJ streamer discharge cause O_3 production during the first 100 s in the low and middle stratosphere. Then the plasma

chemistry perturbations of the chemical system interact strongly with the neutral chemistry during the two days of simulations.

The investigations of streamer simulations at different altitudes reveal that the O_3 losses in the middle and upper stratosphere are mainly due to the NO_x chemical species produced by the discharge through the catalytic cycle. Because the NO_x VMRs produced by the BJ streamer discharge are very efficient for O_3 loss in the middle stratosphere, the O_3 layer after two days of simulation is weaker and appears to "shifted" to lower levels (roughly by 4 km). In the lower stratosphere, the BJ streamer discharge increases O_3 abundance by the very fast conversion of the atomic oxygen produced into O_3 which persists. In the lower stratosphere, the NO_x produced by the BJ streamer discharge is mainly converted into N_2O_5 and HNO_3 and has little impact on O_3.

Whatever the altitude considered, the perturbations on the reactive species ClO_x/BrO_x and HO_x which interact with ozone, lead to the enhancement of chlorine and bromine reservoirs. With their long lifetimes in the stratosphere, they can be transported over long distances and be reactivated later to destroy ozone.

CHAPTER VI

CONCLUSION AND PERSPECTIVES

Contents

6.1 Conclusions

The aim of this thesis is to evaluate the potential impact of blue jet streamer on stratospheric chemistry. To carry out this study, firstly a new detailed ion-neutral chemistry model named MiPO-Streamer model is developed, which based on the MiPLaSMO (Microphysical and Photochemical Lagrangian Stratospheric Model of Ozone) model that has been widely used over the last 20 years to interpret balloon and satellite measurements associated with stratospheric ozone. Compared to the preview study W2015, the MiPO-Streamer model considers in addition the bromine family and more neutral chemistry reactions. There are 117 species and 1760 reactions in the MiPO-Streamer model. The rate coefficients of reactions in the electric field driven processes were calculated with the Bolsig+ solver.

This thesis focused on the event reported by *Chou et al.* [2011]. That event is the first type II gigantic jet to occur over a thunderstorm in the Fujian province of China. It took place on 22th July 2007 and was observed from Lulin Observatory (121°E, 23°N) in Taiwan by three sight-aligned WATEC 100-N cameras. The initial values of temperature, pressure and all gaseous species volume mixing ratios come from a three-

dimensional chemistry-transport model for ruling the Ozone Budget in the Stratosphere (REPROBUS).

As the maximum ozone volume mixing ratio (VMR) is in the middle stratosphere, the MiPO-Streamer model validations, electric field investigation and BJ streamer simulation were first presented at 27 km.

For neutral chemistry validation, the results obtained with the JPL reaction and photolysis rates to those used in W2015 are compared. The results present good agreement. For the plasma chemistry validation, the model considered the BJ streamer discharge as a boxcar field constant pulse, as in W2015. While producing the same maximum electron density as W2015, the plasma chemistry validation revealed differences in the productions of NO and O_3 between the MiPO-Streamer model and W2015. The detailed analysis of NO and O_3 production and loss highlighted that the major difference is due to the rate coefficient of $N_2 + e^- \rightarrow N + N + e^-$, which produces nitrogen atom.

Then the impact of the streamer representation during the first 100 s at 27 km is investigated by using two types of electric field time-profiles: a constant field for a limited duration (pulse), and the electrodynamic simulation of a streamer discharge.

The results on the density of neutral species through the realistic streamer simulation showed an impact of a factor 2 as compared to the pulse-based simulation at 27 km. On analyzing the correlations between electrons and $N_2(A^3\sum_u^+)$, oxygen atom, and nitrogen atom species during the discharge process, it was found that the shape of the electric field evolution considered is critical for an accurate estimate of the streamer impact on chemistry. Higher densities of $N_2(A^3\sum_u^+)$, oxygen atom, $O(^1S)$, ΔO_3, nitrogen atom, $N(^2D)$, $N(^2P)$ and NO_x were produced using the more realistic streamer field. Moreover, the higher density of N_2 excited states is directly linked with the light emission density of the BJ, an important result which could be confirmed by observations. The model results indicated that the impact on both ion and neutral species volume mixing ratios from the realistic streamer (i.e. using a time-varying

electric field) differs from previous model studies considering the streamer electric field as a simple constant pulse. The results pointed out the importance of using a realistic streamer parameterization to model the time-evolution for the electric field.

Moreover, the simulations were performed at an altitude of 27 km in day-time/night-time and over a long-term two-day duration. Among the 117 species considered, this study focused on nitrogen, oxygen, chlorine and bromine species, and ozone perturbation. Looking at neutral chemistry during the first 100 seconds of the simulation, O_3 and NO_x are produced by the BJ. Because of the excess of NO_x VMR produced, the two-day simulation revealed that the O_3 VMR is destroyed through the NO_x catalytic cycle in the middle stratosphere. The O_3 VMR produced by streamer discharge is consumed in one or two days (depending on the streamer parameterizations considered). After two days, O_3 loss appeared and O_3 VMR decreased to a lower VMR than that in the no-discharge simulation case.

Then the impact of the BJ streamer discharge on the chemical system in the whole stratosphere was investigated. The simulations at different altitudes from 20 km to 50 km revealed that the O_3 loss in the middle and upper stratosphere are mainly due to the NO_x chemical species produced by the discharge through the catalytic cycle. Because the NO_x VMRs produced by the BJ streamer discharge are very efficient for O_3 loss in the middle stratosphere, the O_3 layer after two days of simulation is weaker and appears to "shift" to lower levels (roughly by 4 km). In the lower stratosphere, the BJ streamer discharge increases O_3 abundance by the very fast conversion of the atomic oxygen produced into O_3 which persists. In the lower stratosphere, the NO_x produced by the BJ streamer discharge is mainly converted into N_2O_5 and HNO_3 and has little impact on O_3. Whatever the altitude considered, the perturbations on the reactive species ClO_x/BrO_x and HO_x which interact with ozone, lead to the enhancement of the chlorine and bromine reservoirs. With their long lifetimes in the stratosphere, they can be transported over long distances and be reactivated later to destroy ozone.

6.2 Perspectives

As previous studies have indicated, the BJ structure comprises two parts, the streamer and the leader. The leader is caused in the bending point after the largest electric field of the cloud charge appears, then it moves upward and transfers the high electron potential energy outside the cloud top. BJ leaders emit streamers and streamers grow preferentially upward in the exponential atmosphere. Compared to the streamer, the main difference of the leader is its high temperature. It can induce chemical perturbations such as thermal ionization, or the thermal decomposition of nitrogen and oxygen species. This thesis discussed the chemical impacts of BJ streamers. To investigate the realistic impacts of BJ events, a detailed chemical model of the BJ leader is required.

Subsequently, based on the simulation results of the streamer model and the leader model, a macroscopic estimate of the chemical impact of a single blue jet can be investigated. The factors about the density of streamers and leaders, and the real size of streamer and leader in the volume of a single blue jet should be considered. A feasible method is evaluating the electric potential carried by a BJ with the length of the jet (taking the part inside the cloud into account) and an estimate of the ambient field. Then the impacts of BJs on a regional or global scale can be investigated together with BJ frequency. *Perez-Invernon et al.* [2019] conducted this research with the simulation results of W2015, and assumed the production of species in a BJ based on its electrodynamical radius. Since the model used in W2015 is not accurate (no realistic streamer discharge and no bromine chemistry), and the results based on some simplified physical assumptions, it will be interesting to apply the developments of this study on a global scale by considering the electric potential carried by a BJ.

The possibly observable is very interesting for validating the results of model simulations. The variation of ozone vertical mixing ratio by BJ discharge can be validated by satellite chemical measurements, like MIPAS (the Michelson Interferometer for Passive Atmospheric Sounding), GOME (Global Ozone Monitoring

Experiment). Meanwhile, the diffusive mixing and the transport process in the real environment should be taken into account, especially in the long-term (hours, days) simulations. The expected total light output can be compared directly to a spectral ratio measurement or a photometric measurement, if the MiPO-Streamer model considers the excited state distribution ratio, and to couple the results with a light emission model [*Romand et al.*, 2016].

BIBLIOGRAPHY

Anderson, J. G., Brune, W. H., and Proffitt, M. H. (1989), Ozone destruction by chlorine radicals within the Antarctic vortex: The spatial and temporal evolution of ClO-O_3 anticorrelation based on in situ ER-2 data. *Journal of Geophysical Research: Atmospheres, 94*(D9), 11465-11479.

André, P. (1997), Numerical method and composition at and out of chemical equilibrium in a multitemperature plasma. Application to a pure nitrogen plasma. *Contributions to Plasma Physics*, 37(1), 23-40. https://doi.org/10.1002/ctpp.2150370104

Arnone, E., Kero, A., Dinelli, B. M., Enell, C. F., Arnold, N. F. et al. (2008), Seeking sprite-induced signatures in remotely sensed middle atmosphere NO2. *Geophysical Research Letters*, *35*(5).

Arnone, E., Smith, A. K., Enell, C. F., Kero, A., and Dinelli, B. M. (2014), WACCM climate chemistry sensitivity to sprite perturbations. *J. Geophys. Res.: Atmospheres*, *119*(11), 6958-6970.

Austin, J., Butchart, N. and Shine, K. P. (1992), Possibility of an Arctic ozone hole in a doubled-CO_2 climate. Nature360, 221– 225.

Avallone, L. M., and Prather, M. J. (1996), Photochemical evolution of ozone in the lower tropical stratosphere. *J. Geophys. Res.: Atmospheres*, *101*(D1), 1457-1461. https://doi.org/10.1029/95JD03010

Babaeva, N. Y. and Naidis, G. (1996), Two-dimensional modeling of positive streamer dynamics in non-uniform electric fields in air. *J. Phys. D: Appl. Phys.* 29 2423–31.

Baiadze, K. V., Vetsko, V. M., Lopantseva, G. B., Napartovich, A. P., and Pal, A. F. (1985), Properties of a beam-driven discharge in nitrogen with oxygen and water impurities. *Soviet Journal of Plasma Physics*, *11*, 352-360.

Barrington-Leigh, C. P., Inan, U. S., Stanley, M., and Cummer, S. A. (1999), Sprites triggered by negative lightning discharges. *Geophysical Research Letters*, *26*(24), 3605-3608.

Bates, D. R., and Nicolet, M. (1950), The photochemistry of atmospheric water vapor. *J. Geophys. Res.*, *55*(3), 301-327.

Bekki, S., Law, K. S., and Pyle, J. A. (1994), Effect of ozone depletion on atmospheric CH_4 and CO concentrations. *Nature*, *371*(6498), 595.

Bell, T. F., Pasko, V. P., and Inan, U. S. (1995), Runaway electrons as a source of red sprites in the mesosphere. *Geophysical Research Letters*, *22*(16), 2127-2130.

Bell, T. F., Reising, S. C., and Inan, U. S. (1998), Intense continuing currents following positive cloud-to-ground lightning associated with red sprites. *Geophysical Research Letters*, *25*(8), 1285-1288.

Boccippio, D. J., Williams, E. R., Heckman, S. J., Lyons, W. A., Baker, I. T., and Boldi, R. (1995), Sprites, ELF transients, and positive ground strokes. *Science*, *269*(5227), 1088-1091.

Boeck, W. L., Vaughan Jr, O., Blakeslee, R., Vonnegut, B., and Brook, M. (1992), Lightning induced brightening in the airglow layer. *Geophysical research letters*, *19*(2), 99-102.

Brogniez, C., Huret, N., Eckermann, S., Rivière, E. D., Pirre, M., Herman, M., Balois J. Y., Verwaerde C., Larsen N., and Knudsen, B. (2003), Polar stratospheric cloud microphysical properties measured by the microRADIBAL instrument on 25 January 2000 above Esrange and modeling interpretation. *J. Geophys. Res.: Atmospheres*, 108(D6). https://doi.org/10.1029/2001JD001017

Brook, E., Harrison, M. F. A., and Smith, A. C. H. (1978), Measurements of the electron impact ionisation cross sections of He, C, O and N atoms. *Journal of Physics B: Atomic and Molecular Physics*, *11*(17), 3115.

Brunet, H., and Rocca-Serra, J. (1985), Model for a glow discharge in flowing nitrogen. *Journal of applied physics*, *57*(5), 1574-1581.

Callis, L. B., M. Natarajan, and J. D. Lambeth (2002), Observed and Calculated Mesospheric NO, 1992-1997, Geophysical Research Letters, 29, 2.

Capitelli, M., Ferreira, C. M., Gordiets, B. F., and Osipov, A. I. (2000), Plasma kinetics in atmospheric gases (Vol. 31). *Springer Science and Business Media.*

Celestin, S., and Pasko, V. P. (2010), Effects of spatial non-uniformity of streamer discharges on spectroscopic diagnostics of peak electric fields in transient luminous events. *Geophys. Res. Lett.*, 37(7). https://doi.org/10.1029/2010GL042675

Chameides, W. L., Davis, D. D., Bradshaw, J., Rodgers, M., Sandholm, S., and Bai, D. B. (1987), An estimate of the NO_x production rate in electrified clouds based on NO observations from the GTE/CITE 1 fall 1983 field operation. *J. Geophys. Res.: Atmospheres*, 92(D2), 2153-2156. https://doi.org/10.1029/JD092iD02p02153

Chapman, S. (1930), XXXV. On ozone and atomic oxygen in the upper atmosphere. *The London, Edinburgh, and Dublin Philosophical Magazine and Journal of Science*, *10*(64), 369-383.

Chen, A. B., Kuo, C. L., Lee, Y. J., Su, H. T., Hsu, R. R., et al. (2008), Global distributions and occurrence rates of transient luminous events. *J. Geophys. Res.: Space Physics*, *113*(A8).

Chern, J. L., Hsu, R. R., Su, H. T., Mende, S. B., Fukunishi, H., Takahashi, Y., and Lee, L. C. (2003), Global survey of upper atmospheric transient luminous events on the ROCSAT-2 satellite. *Journal of Atmospheric and Solar-Terrestrial Physics*, *65*(5), 647-659.

Chou, J. K., Tsai, L. Y., Kuo, C. L., Lee, Y. J., Chen, C. M., Chen, A. B., Su H. T., Hsu R. R., Chang P. L. and Lee, L. C. (2011), Optical emissions and behaviors of the blue starters, blue jets, and gigantic jets observed in the Taiwan transient luminous event ground campaign. *J. Geophys. Res.: Space Physics*, 116(A7). https://doi.org/10.1029/2010JA016162

Christophorou, L. G. (1984). Electron-Molecule Interactions and their Applications vol 1 (New York: Academic).

Cohen, R. C., and Murphy, J. G. (2003), Photochemistry of NO_2 in Earth's stratosphere: Constraints from observations. *Chemical reviews*, 103(12), 4985-4998. https://doi.org/10.1021/cr020647x

Cosby, P. C. (1993a), Electron-impact dissociation of nitrogen. *The Journal of chemical physics*, *98*(12), 9544-9553.

Cosby, P. C. (1993b), Electron-impact dissociation of oxygen. *The Journal of chemical physics*, *98*(12), 9560-9569.

Croizé, L., Payan, S., Bureau, J., Duruisseau, F., Thiéblemont, R., and Huret, N. (2015), Effect of blue jets on atmospheric composition: feasibility of measurement from a stratospheric balloon. *IEEE Journal of Selected Topics in Applied Earth Observations and Remote Sensing*, 8(6), 3183-3192. DOI: 10.1109/JSTARS.2014.2381556

Crutzen, P. J. (1970), The influence of nitrogen oxides on the atmospheric ozone content. *Quarterly Journal of the Royal Meteorological Society*, *96*(408), 320-325.

Daniel, J. S., Solomon, S., Portmann, R. W., and Garcia, R. R. (1999), Stratospheric ozone destruction: The importance of bromine relative to chlorine. J. Geophys. Res.: Atmospheres, 104(D19), 23871-23880.

DeMore, W. B., Sander, S. P., Golden, D. M., Hampson, R. F., Kurylo, et al. (1997), Chemical kinetics and photochemical data for use in stratospheric modeling, JPL Publication 97-4. *Jet Propulsion Laboratory, Pasadena, CA*.

Dyakonov, M. I. and Kachorovsky, V. Yu. (1989), Streamer discharge in a homogeneous field, Zh. Eksp. Teor. Fiz., vol. 95, pp. 1850–1859, 1989 (Engl. transl.: Sov. Phys. JETP, vol. 68, pp. 1070–1075, 1989).

Eliasson, B. (1986), Basic data for modeling of electrical discharges in gases: oxygen. *Asea Brown Boveri Corporate Research Report*, KLR86-11C.

Enell, C. F., Arnone, E., Adachi, T., Chanrion, O. A., Verronen, P. T., et al. (2008), Parameterisation of the chemical effects of sprites in the middle atmosphere. In *Annales Geophysicae* (Vol. 26, No. 1, pp. 13-27). Copernicus GmbH.

Evtushenko, A. A., Kuterin, F. A., and Mareev, E. A. (2013), A model of sprite influence on the chemical balance of mesosphere. *Journal of Atmospheric and Solar-Terrestrial Physics*, *102*, 298-310.

Franz, R. C., Nemzek, R. J., and Winckler, J. R. (1990), Television image of a large upward electrical discharge above a thunderstorm system. *Science*, *249*(4964), 48-51.

Fukunishi, H., Takahashi, Y., Kubota, M., Sakanoi, K., Inan, U. S., and Lyons, W. A. (1996), Elves: Lightning-induced transient luminous events in the lower ionosphere. *Geophysical Research Letters*, *23*(16), 2157-2160.

Goldenbaum, G. C., and Dickerson, R. R. (1993), Nitric oxide production by lightning discharges. *J. Geophys. Res.: Atmospheres*, *98*(D10), 18333-18338.

Gordillo-Vázquez, F. J. (2008), Air plasma kinetics under the influence of sprites. *Journal of Physics D: Applied Physics*, 41(23), 234016.

Griffing, G. W. (1977), Ozone and oxides of nitrogen production during thunderstorms. *J. Geophys. Res.*, 82(6), 943-950. https://doi.org/10.1029/JC082i006p00943

Grossel, A., Huret, N., Catoire, V., Berthet, G., Renard, J. B., Robert, C., and Gaubicher, B. (2010), In situ balloon-borne measurements of HNO_3 and HCl stratospheric vertical profiles influenced by polar stratospheric cloud formation during the 2005–2006 Arctic winter. *J. Geophys. Res.: Atmospheres*, 115(D21). https://doi.org/10.1029/2009JD012947

Hagelaar, G. J. M., and Pitchford, L. C. (2005), Solving the Boltzmann equation to obtain electron transport coefficients and rate coefficients for fluid models. *Plasma Sources Science and Technology*, 14(4), 722.

Haigh, J. D. (1994), The role of stratospheric ozone in modulating the solar radiative forcing of climate. Nature, 370(6490), 544.

Harder, H., Bösch, H., Camy-Peyret, C., Chipperfield, M. P., Fitzenberger, R., et al. (2000), Comparison of measured and modeled stratospheric BrO: Implications for the total amount of stratospheric bromine. *Geophysical research letters*, *27*(22), 3695-3698.

Hayashi, M., Capitelli, M., and Bardsley, J. N. (1990), Nonequilibrium processes in partially ionized gases. *NATO ASI series*, *220*.

Heavner, M. J. (2000), Optical spectroscopic observations of sprites, blue jets, and elves: Inferred microphysical processes and their macrophysical implications (Doctoral dissertation, University of Alaska Fairbanks).

Heckendorn, P., Weisenstein, D., Fueglistaler, S., Luo, B. P., Rozanov, E., et al. (2009), The impact of geoengineering aerosols on stratospheric temperature and ozone. *Environmental Research Letters*, *4*(4), 045108.

Hiraki, Y., Tong, L., Fukunishi, H., Nanbu, K., Kasai, Y., and Ichimura, A. (2004), Generation of metastable oxygen atom $O(^1D)$ in sprite halos. *Geophysical research letters*, *31*(14).

Hiraki, Y., Kasai, Y., and Fukunishi, H. (2008), Chemistry of sprite discharges through ion-neutral reactions. *Atmospheric Chemistry and Physics*, *8*(14), 3919-3928.

Huret, N., Pommereau, J. P., Dudok de Witt, T., and Pirre, M. (2003, April), Modeling study of NO_x species in the lower tropical stratosphere over Brazil on February 2001. In EGS-AGU-EUG Joint Assembly.

Ihaddadene, M. A., and Celestin, S. (2017), Determination of sprite streamers altitude based on N_2 spectroscopic analysis. *J. Geophys. Res.: Space Physics*, 122(1), 1000-1014. https://doi.org/10.1002/2016JA023111

Inan, U. S., Bell, T. F., and Rodriguez, J. V. (1991), Heating and ionization of the lower ionosphere by lightning. *Geophysical Research Letters*, *18*(4), 705-708.

Inan, U. S., Barrington-Leigh, C., Hansen, S., Glukhov, V. S., Bell, T. F., and Rairden, R. (1997), Rapid lateral expansion of optical luminosity in lightning-induced ionospheric flashes referred to as ‘elves'. *Geophysical Research Letters*, *24*(5), 583-586.

IPCC (2007) Climate Change 2007: Synthesis Report. Fourth Assessment Report. Geneva, Switzerland: Intergovernmental Panel on Climate Change

Itikawa, Y., and Mason, N. (2005), Cross sections for electron collisions with water molecules. *Journal of Physical and Chemical reference data*, *34*(1), 1-22.

Itikawa, Y. (2006), Cross sections for electron collisions with nitrogen molecules. *Journal of physical and chemical reference data*, *35*(1), 31-53.

Itikawa, Y. (2009), Cross sections for electron collisions with oxygen molecules. *Journal of Physical and Chemical Reference Data*, *38*(1), 1-20.

Johnston, H. (1971), Reduction of stratospheric ozone by nitrogen oxide catalysts from supersonic transport exhaust. *Science*, 173(3996), 517-522. DOI: 10.1126/science.173.3996.517

Kirk-Davidoff, D. B., Hintsa, E. J., Anderson, J. G., and Keith, D. W. (1999), The effect of climate change on ozone depletion through changes in stratospheric water vapour. *Nature*, *402*(6760), 399.

Kopp, E., and Fritzenwallner, J. (1997), Chlorine and bromine ions in the D-region. *Advances in Space Research*, *20*(11), 2111-2115.

Kossyi, I. A., Kostinsky, A. Y., Matveyev, A. A., and Silakov, V. P. (1992), Kinetic scheme of the non-equilibrium discharge in nitrogen-oxygen mixtures. *Plasma Sources Science and Technology*, 1(3), 207.

Krehbiel, P. R., Riousset, J. A., Pasko, V. P., Thomas, R. J., Rison, W., Stanley, M. A., and Edens, H. E. (2008), Upward electrical discharges from thunderstorms. *Nature Geoscience*, 1(4), 233. https://doi.org/10.1038/ngeo162

Krueger, A. J., and Minzner, R. A. (1976), A mid-latitude ozone model for the 1976 US Standard Atmosphere. *J. Geophys. Res.*, *81*(24), 4477-4481.

Langematz, U. (2000), An estimate of the impact of observed ozone losses on stratospheric temperature. *Geophysical Research Letters*, *27*(14), 2077-2080.

LeClair, L. R., and McConkey, J. W. (1993), Selective detection of $O(^1S_0)$ following electron impact dissociation of O_2 and N_2O using a XeO^* conversion technique. *The Journal of chemical physics*, *99*(6), 4566-4577.

Lee, A. M., Roscoe, H. K., Jones, A. E., Haynes, P. H., Shuckburgh, E. F., Morrey, M. W., and Pumphrey, H. C. (2001), The impact of the mixing properties within the Antarctic stratospheric vortex on ozone loss in spring. *J. Geophys. Res.: Atmospheres*, *106*(D3), 3203-3211.

Lefèvre, F., Brasseur, G. P., Folkins, I., Smith, A. K., and Simon, P. (1994), Chemistry of the 1991-1992 stratospheric winter: Three-dimensional model simulations. *J. Geophys. Res.: Atmospheres*, 99(D4), 8183-8195. https://doi.org/10.1029/93JD03476

Lefèvre, F., Figarol F., Carslaw K.S., and Peter T. (1998), The 1997 Arctic ozone depletion quantified from three-dimensional model simulations, *Geophys. Res. Lett.*, 25, 2425-2428, 1998. https://doi.org/10.1029/98GL51812

Luque, A., and Gordillo-Vázquez, F. J. (2012), Mesospheric electric breakdown and delayed sprite ignition caused by electron detachment. *Nature Geoscience*, *5*(1), 22.

Lyons, W. A. (1994), Low-light video observations of frequent luminous structures in the stratosphere above thunderstorms. *Monthly Weather Review*, *122*(8), 1940-1946.

Lyons, W. A. (1996), Sprite observations above the US High Plains in relation to their parent thunderstorm systems. *J. Geophys. Res.: Atmospheres*, *101*(D23), 29641-29652.

Lyons, W. A., Nelson, T. E., Armstrong, R. A., Pasko, V. P., and Stanley, M. A. (2003), Upward electrical discharges from thunderstorm tops. *Bulletin of the American Meteorological Society*, *84*(4), 445-454.

MacGorman, D. R., MacGorman, P. S. D. R., Rust, W. D., and Rust, W. D. (1998), The electrical nature of storms. Oxford University Press on Demand.

Majeed, T., and Strickland, D. J. (1997), New survey of electron impact cross sections for photoelectron and auroral electron energy loss calculations. *Journal of Physical and Chemical Reference Data*, *26*(2), 335-349.

Mishin, E. V. (1997), Ozone layer perturbation by a single blue jet. *Geophys. Res. Lett.*, 24(15), 1919-1922. https://doi.org/10.1029/97GL01890

Mishin, E. V., and Milikh, G. M. (2008), Blue jets: Upward lightning. *Space Science Reviews*, 137(1-4), 473. https://doi.org/10.1007/s11214-008-9346-z

Mitchell, J. D., and Hale, L. C. (1973), Observations of the lowest ionosphere. *Space Res*, 13, 471-476.

Molina, M. J., and Rowland, F. S. (1974), Stratospheric sink for chlorofluoromethanes: chlorine atom-catalysed destruction of ozone. *Nature*, *249*(5460), 810.

Murphy, D. M., Fahey, D. W., Proffitt, M. H., Liu, S. C., Chan, K. R., Eubank, C. S., Kawa, S. R., and Kelly, K. K. (1993), Reactive nitrogen and its correlation with ozone in the lower stratosphere and upper troposphere. *J. Geophys. Res.: Atmospheres*, 98(D5), 8751-8773. https://doi.org/10.1029/92JD00681

Naidis, G. V. (2009), Positive and negative streamers in air: Velocity- diameter relation, *Phys. Rev. E*, 79, 057401. DOI: 10.1103/PhysRevE.79.057401

Neubert, T., Mandea, M., Hulot, G., Von Frese, R., Primdahl, F., et al. (2001), Ørsted satellite captures high-precision geomagnetic field data. *Eos, Transactions American Geophysical Union*, *82*(7), 81-88.

Neubert, T. (2003), On sprites and their exotic kin. *Science*, *300*(5620), 747-749.

Neubert, T., Rycroft, M., Farges, T., Blanc, E., Chanrion, O., Arnone, E., Odzimek A., Arnold N., Enell C.-F., Turunen E., Bösinger T., Mika Á., Haldoupis C., et al., (2008), Recent results from studies of electric discharges in the mesosphere. *Surveys in geophysics*, 29(2), 71-137. DOI: 10.1007/s10712-008-9043-1

Parra-Rojas, F. C., Luque, A., and Gordillo-Vázquez, F. J. (2013), Chemical and electrical impact of lightning on the Earth mesosphere: The case of sprite halos. *J. Geophys. Res.: Space Physics*, *118*(8), 5190-5214.

Pasko, V. P., Inan, U. S., Taranenko, Y. N., and Bell, T. F. (1995), Heating, ionization and upward discharges in the mesosphere, due to intense quasi-electrostatic thundercloud fields. *Geophysical Research Letters*, *22*(4), 365-368.

Pasko, V. P., Inan, U. S., and Bell, T. F. (1996), Sprites as luminous columns of ionization produced by quasi-electrostatic thundercloud fields. *Geophys. Res. Lett.*, 23(6), 649-652. https://doi.org/10.1029/96GL00473

Pasko, V. P., Inan U. S., and Bell T. F. (1998), Spatial structure of sprites, *Geophys. Res. Lett.*, 25, 2123–2126. https://doi.org/10.1029/98GL01242

Pasko, V. P., Stanley, M. A., Mathews, J. D., Inan, U. S., and Wood, T. G. (2002), Electrical discharge from a thundercloud top to the lower ionosphere. *Nature*, 416(6877), 152. https://doi.org/10.1038/416152a

Pasko, V. P. (2003), Atmospheric physics: Electric jets. *Nature*, *423*(6943), 927.

Peterson, H., Bailey, M., Hallett, J., and Beasley, W. (2009), NO_x production in laboratory discharges simulating blue jets and red sprites. *J. Geophys. Res.: Space Physics*, 114(A12). https://doi.org/10.1029/2009JA014489

Pasko, V. P., Yair, Y., and Kuo, C. L. (2012), Lightning related transient luminous events at high altitude in the Earth's atmosphere: Phenomenology, mechanisms and effects. *Space science reviews*, *168*(1-4), 475-516.

Pérez-Invernón, F. J., Gordillo-Vázquez, F. J., Smith, A. K., Arnone, E., and Winkler, H. (2019), Global occurrence and chemical impact of stratospheric Blue Jets modeled with WACCM4. *J. Geophys. Res.: Atmospheres*, *124*(5), 2841-2864.

Petrov, N. I., and Petrova, G. N. (1999), Physical mechanisms for the development of lightning discharges between a thundercloud and the ionosphere. *Technical Physics*, 44(4), 472-475. https://doi.org/10.1134/1.1259327

Pitari, G., Mancini, E., Rizi, V., and Shindell, D. T. (2002), Impact of future climate and emission changes on stratospheric aerosols and ozone. *Journal of the Atmospheric Sciences*, *59*(3), 414-440.

Popov, N. A. (2002), Spatial structure of the branching streamer channels in a corona discharge. *Plasma Physics Reports*, 28(7), 615-622. https://doi.org/10.1134/1.1494061

Popov, N. A., Shneider, M. N., and Milikh, G. M. (2016), Similarity analysis of the streamer zone of Blue jets. *Journal of Atmospheric and Solar-Terrestrial Physics*, 147, 121-125. https://doi.org/10.1016/j.jastp.2016.07.003

Portmann, R. W., Daniel, J. S., and Ravishankara, A. R. (2012), Stratospheric ozone depletion due to nitrous oxide: influences of other gases. Philosophical Transactions of the Royal Society B: *Biological Sciences*, 367(1593), 1256-1264. https://doi.org/10.1098/rstb.2011.0377

Prather, M., and Jaffe, A. H. (1990), Global impact of the Antarctic ozone hole: Chemical propagation. *J. Geophys. Res.: Atmospheres*, *95*(D4), 3473-3492.

Prather, M. J. and Watson, R. T. (1990), Stratospheric ozone depletion and future levels of atmospheric chlorine and bromine. *Nature*, 344(6268), 729. https://doi.org/10.1038/344729a0

Prather, M. (1992), Catastrophic loss of stratospheric ozone in dense volcanic clouds. *J. Geophys. Res.: Atmospheres*, *97*(D9), 10187-10191.

Raizer, Y. P., Milikh, G. M., and Shneider, M. N. (2006), On the mechanism of blue jet formation and propagation. *Geophys. Res. Lett.*, 33(23). https://doi.org/10.1029/2006GL027697

Raizer, Y. P., Milikh, G. M., and Shneider, M. N. (2007), Leader–streamers nature of blue jets. *Journal of atmospheric and solar-terrestrial physics*, 69(8), 925-938. https://doi.org/10.1016/j.jastp.2007.02.007

Raizer, Y. P., Milikh, G. M., and Shneider, M. N. (2010), Streamer-and leader-like processes in the upper atmosphere: Models of red sprites and blue jets. *J. Geophys. Res.: Space Physics*, *115*(A7).

Ramaroson, R. (1989), Local, one and three dimensional modelling of chemical processes in the middle atmosphere (Doctoral dissertation, Ph. D. thesis, Univ. Paris VI, Paris, France).

Ramaroson, R., Pirre, M., and Cariolle, D. (1992, June), A box model for on-line computations of diurnal variations in a 1-D model-Potential for application in multidimensional cases. *In Annales geophysicae* (Vol. 10, pp. 416-428).

Riviere, E. D., Huret, N., Taupin, F. G., Renard, J. B., Pirre, M., Eckermann, S. D., Larsen, N., Deshler, T., Lefevre, F., Payan, S., and Camy-Peyret, C. (2000), Role of lee waves in the formation of solid polar stratospheric clouds: Case studies from February 1997. *J. Geophys. Res.: Atmospheres*, 105(D5), 6845-6853. https://doi.org/10.1029/1999JD900908

Riviere, E. D., Pirre, M., Berthet, G., Renard, J. B., Taupin, F. G., Huret, N., Chartier, M., Knudsen, B., and Lefevre, F. (2002), On the interaction between nitrogen and

halogen species in the Arctic polar vortex during THESEO and THESEO 2000. *J. Geophys. Res.: Atmospheres*, 107(D5). https://doi.org/10.1029/2002JD002087

Roussel-Dupré, R., and Gurevich, A. V. (1996), On runaway breakdown and upward propagating discharges. *J. Geophys. Res.: Space Physics*, 101(A2), 2297-2311. https://doi.org/10.1029/95JA03278

Salawitch, R. J., Wofsy, S. C., Gottlieb, E. W., Lait, L. R., Newman, P. A., et al. (1993), Chemical loss of ozone in the Arctic polar vortex in the winter of 1991-1992. *Science*, *261*(5125), 1146-1149.

Sander, S. P., Golden, D. M., Kurylo, M. J., Moortgat, G. K., Wine, P. H., Ravishankara, A. R., Kolb, C. E., Molina, M. J., Finlayson-Pitts, B. J., and Orkin, V. L. (2006), Chemical kinetics and photochemical data for use in atmospheric studies evaluation number 15. Pasadena, CA: Jet Propulsion Laboratory, National Aeronautics and Space Administration, 2006. http://hdl.handle.net/2014/41648

Sander, S. P., Friedl, R. R., Barker, J. R., Golden, D. M., et al. (2011), Chemical kinetics and photochemical data for use in atmospheric studies, evaluation number 14. *JPL publication*, 10-6.

Sentman, D. D., and Wescott, E. M. (1993), Observations of upper atmospheric optical flashes recorded from an aircraft. *Geophysical Research Letters*, *20*(24), 2857-2860.

Sentman, D. D., Wescott, E. M., Osborne, D. L., Hampton, D. L., and Heavner, M. J. (1995), Preliminary results from the Sprites94 aircraft campaign: 1. Red sprites. *Geophysical Research Letters*, *22*(10), 1205-1208.

Sentman, D. D., Stenbaek-Nielsen, H. C., McHarg, M. G., and Morrill, J. S. (2008), Plasma chemistry of sprite streamers. *J. Geophys. Res.: Atmospheres*, 113(D11). https://doi.org/10.1029/2007JD008941

Sentman, D. D., and Stenbaek-Nielsen, H. C. (2009), Chemical effects of weak electric fields in the trailing columns of sprite streamers. *Plasma Sources Science and Technology*, *18*(3), 034012.

Shindell, D. T., Rind, D. and Lonergan, P (1998), Increased polar stratospheric ozone losses and delayed eventual recovery owing to increasing greenhouse-gas concentrations. Nature392, 589– 592.

Skalny, J. D., Matejcik, S., Kiendler, A., Stamatovic, A., and Märk, T. D. (1996), Dissociative electron attachment to ozone using a high-resolution crossed beams technique. *Chemical physics letters*, *255*(1-3), 112-118.

Smirnova, N. V., Lyakhov, A. N., and Kozlov, S. I. (2003), Lower stratosphere response to electric field pulse. *Int. J. Geomagn. Aeron*, 3(3), 281-287.

Solomon, S. (1999), Stratospheric ozone depletion: A review of concepts and history. *Reviews of Geophysics*, *37*(3), 275-316.

Soula, S., Van Der Velde, O., Montanya, J., Huet, P., Barthe, C., and Bór, J. (2011), Gigantic jets produced by an isolated tropical thunderstorm near Réunion Island. *J. Geophys. Res.: Atmospheres*, *116*(D19).

Stolarski, R. S., and Cicerone, R. J. (1974), Stratospheric chlorine: a possible sink for ozone. *Canadian journal of Chemistry*, *52*(8), 1610-1615.

Stolzenbach, A. (2016), Etude de la photochimie de Vénus à l'aide d'un modèle de circulation générale (Doctoral dissertation, Paris 6).

Su, H. T., Hsu, R. R., Chen, A. B., Wang, Y. C., Hsiao, W. S., Lai, W. C., et al. (2003), Gigantic jets between a thundercloud and the ionosphere. *Nature*, *423*(6943), 974.

Sukhorukov, A. I., and Stubbe, P. (1997), Excitation of the ionospheric Alfven resonator by strong lightning discharges. *Geophys. Res. Lett.*, 24(8), 829-832. https://doi.org/10.1029/97GL00807

Takahashi, Y., Kubota, M., Sakanoi, K., Fukunishi, H., Inan, U. S., and Lyons, W. A. (1995), Spatial and temporal relationship between lower ionospheric flashes and sprites. *EOS*, *76*, 106.

Wescott, E. M., Sentman, D., Osborne, D., Hampton, D., and Heavner, M. (1995), Preliminary results from the Sprites94 aircraft campaign: 2. Blue jets. *Geophysical research letters*, *22*(10), 1209-1212.

Wescott, E. M., Sentman, D. D., Heavner, M. J., Hampton, D. L., Osborne, D. L., and Vaughan Jr, O. H. (1996), Blue starters:: Brief upward discharges from an intense Arkansas thunderstorm. *Geophys. Res. Lett.*, 23(16), 2153-2156. https://doi.org/10.1029/96GL01969

Wescott, E. M., Sentman, D. D., Heavner, M. J., Hampton, D. L., Lyons, W. A., and Nelson, T. (1998), Observations of 'Columniform' sprites. *Journal of atmospheric and solar-terrestrial physics*, *60*(7-9), 733-740.

Wescott, E. M., Stenbaek-Nielsen, H. C., Sentman, D. D., Heavner, M. J., Moudry, D. R., and Sabbas, F. S. (2001), Triangulation of sprites, associated halos and their possible relation to causative lightning and micrometeors. *J. Geophys. Res.: Space Physics*, *106*(A6), 10467-10477.

Wiesmann, H. J., and Pietronero, L. (1986), Properties of Laplacian fractals for dielectric breakdown in 2 and 3 dimensions. *In Fractals in Physics* (pp. 151-157). https://doi.org/10.1016/B978-0-444-86995-1.50030-5

Winckler, J. R., Franz, R. C., and Nemzek, R. J. (1993), Fast low-level light pulses from the night sky observed with the SKYFLASH program. *J. Geophys. Res.: Atmospheres*, *98*(D5), 8775-8783.

Winkler, H., and Notholt, J. (2014), The chemistry of daytime sprite streamers–a model study. *Atmospheric Chemistry and Physics*, 14(7), 3545-3556. https://doi.org/10.5194/acp-14-3545-2014

Winkler, H., and Notholt, J. (2015), A model study of the plasma chemistry of stratospheric Blue Jets. *Journal of Atmospheric and Solar-Terrestrial Physics*, 122, 75-85. https://doi.org/10.1016/j.jastp.2014.10.015

WMO (World Meteorological Organization), Scientific Assessment of Ozone Depletion: 1994, Rep. 37, WMO Global Ozone Res. and Monit. Proj., Geneva, 1995

WMO (World Meteorological Organization), Assessment for Decision-Makers: Scientific Assessment of Ozone Depletion: 2014, 88 pp., Global Ozone Research and Monitoring Project-Report No. 56, Geneva, Switzerland, 2014. https://www.esrl.noaa.gov/csd/assessments/ozone/2014/

WMO (World Meteorological Organization), Scientific Assessment of Ozone Depletion: 2018, Global Ozone Res. and Monit. Proj., No. 58, 588 pp., Geneva, Switzerland, 2018. https://www.esrl.noaa.gov/csd/assessments/ozone/2018/

Yousfi, M., and Benabdessadok, M. D. (1996), Boltzmann equation analysis of electron-molecule collision cross sections in water vapor and ammonia. *Journal of applied physics*, *80*(12), 6619-6630.

Yung, Y. L., Pinto, J. P., Watson, R. T., and Sander, S. P. (1980), Atmospheric bromine and ozone perturbations in the lower stratosphere. *Journal of the Atmospheric Sciences*, 37(2), 339-353. https://doi.org/10.1175/1520-0469(1980)037<0339:ABAOPI>2.0.CO;

Zipf, E. C., Espy, P. J., and Boyle, C. F. (1980), The excitation and collisional deactivation of metastable N(²P) atoms in auroras. *J. Geophys. Res.: Space Physics*, *85*(A2), 687-694.

ANNEX 1

Sets of chemical reactions

The sets of chemical reactions considered in the MiPO-Streamer model are presented below.

The reactions that have different coefficient rates from *Winkler et al.* [2015] are in blue. The reactions that are not considered in *Winkler et al.* [2015] are in red.

The rate coefficients are in units of S^{-1} for unimolecular, cm^3s^{-1} for two-body, and cm^6s^{-1} for three-body reactions. T is the gas temperature in Kelvin. M stands for N_2 and O_2 molecule.

	Reaction	Rate coefficient	Reference
Electron attachment			
1	$e^- + O_2 + O_2 \rightarrow O_2^- + O_2$	$1.4 \times 10^{-29} \times (T/300)^{-1} \times \exp(-600/T)$	15
2	$e^- + O_2 + N_2 \rightarrow O_2^- + N_2$	$1.07 \times 10^{-31} \times (T/300)^{-2} \times \exp(-70/T)$	15
3	$e^- + O + O_2 \rightarrow O^- + O_2$	10^{-31}	9
4	$e^- + O + O_2 \rightarrow O^- + O_2$	10^{-31}	9
5	$e^- + O_3 \rightarrow O_2^- + O$	10^{-9}	9
6	$e^- + O_3 \rightarrow O^- + O_2$	10^{-11}	9
7	$e^- + O_3 + O_2 \rightarrow O_3^- + O_2$	10^{-31}	3
8	$e^- + NO \xrightarrow{M} NO^-$	10^{-30}	9
9	$e^- + NO_2 \rightarrow NO_2^-$	3×10^{-11}	9
10	$e^- + NO_2 \rightarrow O^- + NO$	10^{-11}	9
11	$e^- + H_2O + O_2 \rightarrow O_2^- + H_2O$	1.4×10^{-29}	3
Electron detachment			
1	$O_2^- + N_2 \rightarrow e^- + O_2 + N_2$	$1.9 \times 10^{-12} \times (T/300)^{0.5} \times \exp(-4990/T)$	9
2	$O_2^- + O_2 \rightarrow e^- + O_2 + O_2$	$2.7 \times 10^{-10} \times (T/300)^{0.5} \times \exp(-5990/T)$	9

3	$O_2^- + O_2(a) \rightarrow e^- + O_2 + O_2$	2×10^{-10}	9
4	$O_2^- + O_2(b) \rightarrow e^- + O_2 + O_2$	3.6×10^{-10}	9
5	$O_2^- + N_2(A) \rightarrow e^- + O_2 + N_2$	2.1×10^{-9}	9
6	$O_2^- + N_2(B) \rightarrow e^- + O_2 + N_2$	2.5×10^{-9}	9
7	$O_2^- + O \rightarrow e^- + O_3$	1.5×10^{-10}	9
8	$O_2^- + N \rightarrow e^- + NO_2$	5×10^{-10}	9
9	$O_2^- + H_2O \rightarrow e^- + O_2 + H_2O$	$5 \times 10^{-9} \times \exp(-5000/T)$	3
10	$O^- + O_2(a) \rightarrow e^- + O_3$	3×10^{-10}	9
11	$O^- + O_2(b) \rightarrow e^- + O + O_2$	6.9×10^{-10}	9
12	$O^- + N_2(A) \rightarrow e^- + O + N_2$	2.2×10^{-9}	9
13	$O^- + N_2(B) \rightarrow e^- + O + N_2$	1.9×10^{-9}	9
14	$O^- + N_2 \rightarrow e^- + N_2O$	10^{-12}	3
15	$O^- + H_2 \rightarrow e^- + H_2O$	7×10^{-10}	3
16	$O^- + O \rightarrow e^- + O_2$	5×10^{-10}	9
17	$O^- + N \rightarrow e^- + NO$	2.6×10^{-10}	9
18	$O^- + O_2 \rightarrow e^- + O_3$	5×10^{-15}	9
19	$O^- + NO \rightarrow e^- + NO_2$	2.6×10^{-10}	9
20	$O^- + O_3 \rightarrow e^- + O_2 + O_2$	$5 \times 10^{-10} \times (T/300)^{0.5}$	15
21	$O_3^- + O \rightarrow e^- + O_2 + O_2$	3×10^{-10}	9
22	$O_3^- + O_3 \rightarrow e^- + 3O_2$	10^{-10}	3
23	$NO^- + CO_2 \rightarrow e^- + NO + CO_2$	8.3×10^{-12}	3
24	$NO^- + N_2O \rightarrow e^- + NO + N_2O$	5.1×10^{-12}	3
25	$NO^- + NO \rightarrow e^- + NO + NO$	5×10^{-12}	3
26	$NO_2^- + O \rightarrow e^- + NO_3$	10^{-12}	9
27	$OH^- + O \rightarrow e^- + HO_2$	$4 \times 10^{-10} \times (T/300)^{0.5}$	15
28	$Cl^- + H \rightarrow e^- + HCl$	$9.3 \times 10^{-10} \times (T/300)^{0.5}$	15
Associative and Penning ionization			
1	$N_2(a'^1) + N_2(A) \rightarrow e^- + N_4^+$	1.5×10^{-11}	3
2	$N_2(a'^1) + N_2(a'^1) \rightarrow e^- + N_4^+$	10^{-11}	3
3	$N_2(a^1) + N_2(a^1) \rightarrow e^- + N_2^+$	2×10^{-10}	3
4	$N(^2P) + N(^2P) \rightarrow e^- + N_2^+$	10^{-11}	12
5	$N(^2P) + O \rightarrow e^- + NO^+$	10^{-11}	12

6	$N(^2P) + N(^2D) \rightarrow e^- + N_2^+$	10^{-12}	9
Positive ion chemistry			
1	$N_2^+ + N + N_2 \rightarrow N_3^+ + N_2$	$9 \times 10^{-30} \times \exp(400/T)$	9
2	$N_2^+ + O_2 \rightarrow O_2^+ + N_2$	$6 \times 10^{-11} \times (T/300)^{-0.5}$	9
3	$N_2^+ + O \rightarrow NO^+ + N$	$1.3 \times 10^{-10} \times (T/300)^{-0.5}$	9
4	$N_2^+ + O \rightarrow O^+ + N_2$	$10^{-11} \times (T/300)^{-0.2}$	9
5	$N_2^+ + O_3 \rightarrow O_2^+ + O + N_2$	10^{-10}	9
6	$N_2^+ + N_2O \rightarrow N_2O^+ + N_2$	5×10^{-10}	9
7	$N_2^+ + N_2O \rightarrow NO^+ + N + N_2$	4×10^{-10}	9
8	$N_2^+ + NO \rightarrow NO^+ + N_2$	3.3×10^{-10}	9
9	$N_2^+ + N_2 + N_2 \rightarrow N_4^+ + N_2$	$5.2 \times 10^{-29} \times (T/300)^{-2.2}$	3
10	$N_2^+ + N_2(A) \rightarrow N_3^+ + N$	3×10^{-10}	9
11	$N_2^+ + N \rightarrow N^+ + N_2$	$2.4 \times 10^{-15} \times T$	9
12	$N_3^+ + O_2 \rightarrow NO_2^+ + N_2$	4.4×10^{-11}	9
13	$N_3^+ + O_2 \rightarrow O_2^+ + N + N_2$	2.3×10^{-11}	9
14	$N_3^+ + NO \rightarrow N_2O^+ + N_2$	$7 \times 10^{-11} \times (T/300)^{0.5}$	15
15	$N_3^+ + N_2(A) \rightarrow N_3^+ + N_2$	3×10^{-10}	3
16	$N_3^+ + N \rightarrow N_2^+ + N_2$	6.6×10^{-11}	9
17	$N_3^+ + NO \rightarrow NO^+ + N + N_2$	7×10^{-11}	9
18	$N_3^+ + NO \rightarrow N_2O^+ + N_2$	7×10^{-11}	9
19	$N_3^+ + O_2 \rightarrow O_2^+ + N + N_2$	2.3×10^{-11}	3
20	$N_4^+ + N_2 \rightarrow N_2^+ + N_2 + N_2$	$2.1 \times 10^{-16} \times (T/300)^{0.5}$	15
21	$N_4^+ + O_2 \rightarrow O_2^+ + N_2 + N_2$	2.5×10^{-10}	15
22	$N_4^+ + O \rightarrow O^+ + N_2 + N_2$	2.5×10^{-10}	9
23	$N_4^+ + N \rightarrow N^+ + N_2 + N_2$	10^{-11}	9
24	$N_4^+ + NO \rightarrow NO^+ + N_2 + N_2$	4×10^{-10}	9
25	$N^+ + N_2 + N_2 \rightarrow N_3^+ + N_2$	$9 \times 10^{-30} \times \exp(400/T)$	9
26	$N^+ + N \overset{M}{\rightarrow} N_2^+$	10^{-29}	9
27	$N^+ + O \overset{M}{\rightarrow} NO^+$	10^{-29}	9
28	$N^+ + O \rightarrow O^+ + N$	10^{-12}	9
29	$N^+ + O_3 \rightarrow NO^+ + O_2$	5×10^{-10}	9
30	$N^+ + O_2 \rightarrow O_2^+ + N$	$2 \times 10^{-10} \times (T/300)^{0.5}$	15

31	$N^+ + O_2 \rightarrow O_2^+ + N(^2D)$	$8.4 \times 10^{-11} \times (T/300)^{0.5}$	15
32	$N^+ + O_2 \rightarrow NO^+ + O$	$5 \times 10^{-11} \times (T/300)^{0.5}$	15
33	$N^+ + O_2 \rightarrow NO^+ + O(^1D)$	$2 \times 10^{-10} \times (T/300)^{0.5}$	15
34	$N^+ + O_2 \rightarrow O^+ + NO$	2.8×10^{-11}	9
35	$N^+ + NO \rightarrow NO^+ + N$	8×10^{-10}	9
36	$N^+ + NO \rightarrow N_2^+ + O$	3×10^{-12}	9
37	$N^+ + NO \rightarrow O^+ + N_2$	10^{-12}	9
38	$N^+ + N_2O \rightarrow NO^+ + N_2$	5.5×10^{-10}	9
39	$O_2^+ + O_2 + O_2 \rightarrow O_4^+ + O_2$	$2.4 \times 10^{-30} \times (T/300)^{-3.2}$	9
40	$O_2^+ + N_2 + N_2 \rightarrow N_2O_2^+ + N_2$	$9 \times 10^{-31} \times (T/300)^{-2}$	9
41	$O_2^+ + N_2 \rightarrow NO^+ + NO$	$4 \times 10^{-21} \times (T/300)^{-2}$	16
42	$O_2^+ + N \rightarrow NO^+ + O$	1.2×10^{-10}	9
43	$O_2^+ + NO \rightarrow NO^+ + O_2$	4.4×10^{-10}	9
44	$O_2^+ + NO_2 \rightarrow NO_2^+ + O_2$	6.6×10^{-10}	9
45	$O_2^+ + NO_2 \rightarrow NO^+ + O_3$	10^{-11}	9
46	$O_2^+ + N_2O_5 \rightarrow NO_2^+ + NO_3 + O_2$	8.8×10^{-10}	9
47	$O_4^+ + O_2 \rightarrow O_2^+ + O_2 + O_2$	$3.3 \times 10^{-6} \times (T/300)^{-4} \times \exp(-5030/T)$	9
48	$O_4^+ + O_2(a) \rightarrow O_2^+ + O_2 + O_2$	10^{-10}	9
49	$O_4^+ + O_2(b) \rightarrow O_2^+ + O_2 + O_2$	10^{-10}	9
50	$O_4^+ + O \rightarrow O_2^+ + O_3$	3×10^{-10}	9
51	$O_4^+ + NO \rightarrow NO^+ + O_2 + O_2$	10^{-10}	9
52	$O_4^+ + N_2 \rightarrow N_2O_2^+ + O_2$	$4.61 \times 10^{-12} \times (T/300)^{2.5} \times \exp(-2650/T)$	9
53	$N_2O_2^+ + N_2 \rightarrow O_2^+ + 2N_2$	$1.1 \times 10^{-6} \times (T/300)^{-5.3} \times \exp(-2357/T)$	9
54	$N_2O_2^+ + O_2 \rightarrow O_4^+ + N_2$	10^{-9}	9
55	$N_2O_2^+ + H_2O \rightarrow O_2^+(H_2O) + N_2$	4×10^{-9}	4
56	$O^+ + O \xrightarrow{M} O_2^+$	10^{-29}	9
57	$O^+ + N \xrightarrow{M} NO^+$	10^{-29}	9
58	$O^+ + O_2 \rightarrow O_2^+ + O$	$2 \times 10^{-11} \times (T/300)^{-0.4}$	15
59	$O^+ + N_2 \rightarrow NO^+ + N$	$1.2 \times 10^{-12} \times (T/300)^{-1}$	15
60	$O^+ + N_2 \xrightarrow{M} NO^+ + N$	$6 \times 10^{-29} \times (T/300)^{-2}$	9
61	$O^+ + NO_2 \rightarrow NO_2^+ + O$	1.6×10^{-9}	9
62	$O^+ + NO \rightarrow NO^+ + O$	2.4×10^{-11}	9

63	$O^+ + NO \rightarrow O_2^+ + N$	3×10^{-12}	9
64	$O^+ + N(^2D) \rightarrow N^+ + O$	1.3×10^{-10}	9
65	$O^+ + N_2O \rightarrow N_2O^+ + O$	4×10^{-10}	9
66	$O^+ + N_2O \rightarrow NO^+ + NO$	2.3×10^{-10}	9
67	$O^+ + N_2O \rightarrow O_2^+ + N_2$	2×10^{-11}	9
68	$O^+ + O_3 \rightarrow O_2^+ + O_2$	10^{-10}	9
69	$NO_2^+ + NO \rightarrow NO^+ + NO_2$	2.9×10^{-10}	9
70	$N_2O^+ + NO \rightarrow NO^+ + N_2O$	2.9×10^{-10}	9
71	$NO^+ + N_2 + N_2 \rightarrow NO^+(N_2) + N_2$	$2 \times 10^{-31} \times (T/300)^{-4.4}$	9
72	$NO^+ + O_2 + N_2 \rightarrow NO^+(O_2) + N_2$	3×10^{-31}	9
73	$NO^+ + O_2 + O_2 \rightarrow NO^+(O_2) + O_2$	9×10^{-32}	9
74	$NO^+ + O_3 \rightarrow NO_2^+ + O_2$	10^{-15}	9
75	$NO^+ + N_2O_5 \rightarrow NO_2^+ + 2NO_2$	5.9×10^{-10}	9
76	$O^+ + H_2 \rightarrow OH^+ + H$	1.62×10^{-9}	3
77	$O^+ + H_2O \rightarrow H_2O^+ + O$	2.6×10^{-9}	3
78	$H_2O^+ + O_2 \rightarrow O_2^+ + H_2O$	3.3×10^{-10}	3
79	$H_2O^+ + NO_2 \rightarrow NO_2^+ + H_2O$	1.2×10^{-9}	3
80	$H_2O^+ + NO \rightarrow NO^+ + H_2O$	4.6×10^{-9}	3
81	$OH^+ + O_2 \rightarrow O_2^+ + OH$	3.8×10^{-10}	3
82	$N_4^+ + H_2O \rightarrow H_2O^+ + 2N_2$	3×10^{-9}	3
83	$N_2^+ + H_2O \rightarrow H_2O^+ + N_2$	2.4×10^{-9}	3
84	$N^+ + H_2O \rightarrow H_2O^+ + N$	2.7×10^{-9}	6
85	$H_2O^+ + H_2O \rightarrow H^+(H_2O) + OH$	1.85×10^{-9}	3
86	$H_2O^+ + H_2O \rightarrow H^+(H_2O) + H$	7.6×10^{-10}	6
87	$H^+(H_2O) + H_2O \xrightarrow{M} H^+(H_2O)_2$	$4.6 \times 10^{-27} \times (T/300)^{-4}$	6
88	$H^+(H_2O)_2 + H_2O \xrightarrow{M} H^+(H_2O)_3$	$8.6 \times 10^{-27} \times (T/300)^{-7.5}$	6
89	$H^+(H_2O)_3 + H_2O \xrightarrow{M} H^+(H_2O)_4$	$3.6 \times 10^{-27} \times (T/300)^{-8.1}$	6
90	$H^+(H_2O)_4 + H_2O \xrightarrow{M} H^+(H_2O)_5$	$4.6 \times 10^{-28} \times (T/300)^{-14}$	6
91	$H^+(H_2O)_5 + H_2O \xrightarrow{M} H^+(H_2O)_6$	$5.8 \times 10^{-29} \times (T/300)^{-15.3}$	6
92	$H^+(H_2O)_6 + H_2O \xrightarrow{M} H^+(H_2O)_7$	$5.74 \times 10^{-29} \times (T/300)^{-15.3}$	6
93	$H^+(H_2O)_2 \xrightarrow{M} H^+(H_2O) + H_2O$	$2.5 \times 10^{-2} \times (T/300)^{-5} \times \exp(-15900/T)$	6

94	$H^+(H_2O)_3 \xrightarrow{M} H^+(H_2O)_2 + H_2O$	$1.2 \times 10^{-2} \times (T/300)^{-8.5} \times \exp(-9800/T)$	6
95	$H^+(H_2O)_4 \xrightarrow{M} H^+(H_2O)_3 + H_2O$	$1.5 \times 10^{-1} \times (T/300)^{-9.1} \times \exp(-9000/T)$	6
96	$H^+(H_2O)_5 \xrightarrow{M} H^+(H_2O)_4 + H_2O$	$1.7 \times 10^{-3} \times (T/300)^{-15} \times \exp(-6400/T)$	6
97	$H^+(H_2O)_6 \xrightarrow{M} H^+(H_2O)_5 + H_2O$	$4 \times 10^{-3} \times (T/300)^{-16.3} \times \exp(-5800/T)$	6
98	$H^+(H_2O)_7 \xrightarrow{M} H^+(H_2O)_6 + H_2O$	$7.17 \times 10^{-4} \times (T/300)^{-16.3} \times \exp(-5390/T)$	6
99	$O_4^+ + H_2O \rightarrow O_2^+(H_2O) + O_2$	$1.5 \times 10^{-9} \times (T/300)^{0.5}$	15
100	$O_2^+(H_2O) + H_2O \rightarrow H^+(H_2O) + OH + O_2$	$2 \times 10^{-10} \times (T/300)^{0.5}$	15
101	$O_2^+(H_2O) + H_2O \rightarrow H^+(H_2O)OH + O_2$	$10^{-9} \times (T/300)^{0.5}$	15
102	$H^+(H_2O)OH + H_2O \rightarrow H^+(H_2O)_2 + OH$	$1.4 \times 10^{-9} \times (T/300)^{0.5}$	15
103	$O_2^+ + H_2O + N_2 \rightarrow O_2^+(H_2O) + N_2$	2.5×10^{-28}	6
104	$O_2^+ + H_2O + O_2 \rightarrow O_2^+(H_2O) + O_2$	2.6×10^{-28}	6
105	$NO^+ + H_2O \xrightarrow{M} NO^+(H_2O)$	$1.8 \times 10^{-28} \times (T/300)^{-4.7}$	15
106	$NO^+(H_2O) + H_2O \xrightarrow{M} NO^+(H_2O)_2$	$10^{-27} \times (T/300)^{-4.7}$	15
107	$NO^+(H_2O)_2 + H_2O \xrightarrow{M} NO^+(H_2O)_3$	$10^{-27} \times (T/300)^{-4.7}$	15
108	$NO^+(H_2O)_3 + H_2O \rightarrow H^+(H_2O)_3 + HNO_2$	7×10^{-11}	6
109	$NO^+ + CO_2 \xrightarrow{M} NO^+(CO_2)$	$7 \times 10^{-30} \times (T/300)^{-3}$	15
110	$NO^+(CO_2) + H_2O \rightarrow NO^+(H_2O) + CO_2$	$10^{-9} \times (T/300)^{0.5}$	15
111	$NO^+(CO_2) \xrightarrow{M} NO^+ + CO_2$	$6.2 \times 10^{-7} \times (T/300)^{-5} \times \exp(-4590/T)$	6
112	$NO^+(H_2O) + CO_2 \xrightarrow{M} NO^+(H_2O)(CO_2)$	$7 \times 10^{-30} \times (T/300)^{-3}$	15
113	$NO^+(H_2O)(CO_2) + H_2O \rightarrow NO^+(H_2O)_2 + CO_2$	$10^{-9} \times (T/300)^{0.5}$	15
114	$NO^+(H_2O)_2 + CO_2 \xrightarrow{M} NO^+(H_2O)_2(CO_2)$	$7 \times 10^{-30} \times (T/300)^{-3}$	15
115	$NO^+(H_2O)_2(CO_2) + H_2O \rightarrow NO^+(H_2O)_3 + CO_2$	$10^{-9} \times (T/300)^{-3}$	15
116	$NO^+(H_2O)_2(CO_2) \xrightarrow{M} NO^+(H_2O)_2 + CO_2$	$3.8 \times 10^{-6} \times (T/300)^{-5} \times \exp(-3335/T)$	6
117	$NO^+(H_2O)(CO_2) \xrightarrow{M} NO^+(H_2O) + CO_2$	$3.8 \times 10^{-6} \times (T/300)^{-5} \times \exp(-4025/T)$	6
118	$NO^+(H_2O)_2 + N_2 \xrightarrow{M} NO^+(H_2O)_2(N_2)$	$2 \times 10^{-31} \times (T/300)^{-4.4}$	15
119	$NO^+(H_2O)(N_2) + CO_2 \rightarrow NO^+(H_2O)(CO_2) + N_2$	$10^{-9} \times (T/300)^{0.5}$	15
120	$NO^+(H_2O)_2(N_2) + CO_2 \rightarrow NO^+(H_2O)_2(CO_2) + N_2$	$10^{-9} \times (T/300)^{0.5}$	15
121	$NO^+(H_2O) + N_2 \xrightarrow{M} NO^+(H_2O)(N_2)$	$2 \times 10^{-31} \times (T/300)^{-4.4}$	6
122	$NO^+(H_2O)(N_2) \xrightarrow{M} NO^+(H_2O) + N_2$	$6.3 \times 10^{-8} \times (T/300)^{-5.4} \times \exp(-2150/T)$	6

123	$NO^+(H_2O)_2(N_2) \xrightarrow{M} NO^+(H_2O)_2 + N_2$	$6.3 \times 10^{-8} \times (T/300)^{-5.4} \times \exp(-1800/T)$	6
124	$NO^+(N_2) + CO_2 \rightarrow NO^+(CO_2) + N_2$	7.99×10^{-10}	6
125	$NO^+(N_2) + H_2O \rightarrow NO^+(H_2O) + N_2$	$2.35 \times 10^{-9} \times (T/300)^{-0.5} + 2.41 \times 10^{-10}$	6
126	$NO^+(N_2) \xrightarrow{M} NO^+ + N_2$	$1.5 \times 10^{-8} \times (T/300)^{-5.3} \times \exp(-2093/T)$	6
127	$NO^+(N_2) + O_2 \rightarrow NO^+ + N_2$	10^{-9}	16
128	$NO^+(O_2) + N_2 \rightarrow NO^+ + O_2$	10^{-9}	16
129	$H^+(H_2O) + CO_2 \xrightarrow{M} H^+(H_2O)(CO_2)$	$8.5 \times 10^{-28} \times (T/300)^{-4}$	6
130	$H^+(H_2O) + N_2 \xrightarrow{M} H^+(H_2O)(N_2)$	$3.5 \times 10^{-31} \times (T/300)^{-4}$	6
131	$H^+(H_2O)(CO_2) + H_2O \rightarrow H^+(H_2O)_2 + CO_2$	$2.33 \times 10^{-9} \times (T/300)^{-0.5} + 2.39 \times 10^{-10}$	6
132	$H^+(H_2O)(CO_2) \xrightarrow{M} H^+(H_2O) + CO_2$	$5.5 \times 10^{-3} \times (T/300)^{-5} \times \exp(-7700/T)$	6
133	$H^+(H_2O)(N_2) + CO_2 \rightarrow H^+(H_2O)(CO_2) + N_2$	8.38×10^{-10}	6
134	$H^+(H_2O)(N_2) + H_2O \rightarrow H^+(H_2O)_2 + N_2$	2.6×10^{-9}	6
135	$H^+(H_2O)(N_2) \xrightarrow{M} H^+(H_2O) + N_2$	$10^{-8} \times (T/300)^{-5.4} \times \exp(-2800/T)$	6
136	$H^+(H_2O)_2 + CO_2 \xrightarrow{M} H^+(H_2O)_2(CO_2)$	$8.5 \times 10^{-28} \times (T/300)^{-4}$	6
137	$H^+(H_2O)_2 + N_2 \xrightarrow{M} H^+(H_2O)_2(N_2)$	$3.5 \times 10^{-31} \times (T/300)^{-4}$	6
138	$H^+(H_2O)_2(CO_2) + H_2O \rightarrow H^+(H_2O)_3 + CO_2$	$2.27 \times 10^{-9} \times (T/300)^{-0.5} + 2.33 \times 10^{-10}$	6
139	$H^+(H_2O)_2(CO_2) \xrightarrow{M} H^+(H_2O)_2 + CO_2$	$10^{-3} \times (T/300)^{-5} \times \exp(-6200/T)$	6
140	$H^+(H_2O)_2(N_2) + CO_2 \rightarrow H^+(H_2O)_2(CO_2) + N_2$	7.8×10^{-10}	6
141	$H^+(H_2O)_2(N_2) \xrightarrow{M} H^+(H_2O)_2 + N_2$	$1.2 \times 10^{-8} \times (T/300)^{-5.4} \times \exp(-2700/T)$	6
Negative ion chemistry			
1	$e^- + O_3 \rightarrow e^- + O_2 + O$	10^{-8}	3
2	$O^- + O_2 \rightarrow O_3^- + O$	5.3×10^{-10}	9
3	$O^- + O_2 \xrightarrow{M} O_3^-$	$1.1 \times 10^{-30} \times (T/300)^{-1}$	9
4	$O^- + O_2(a) \rightarrow O_2^- + O$	10^{-10}	9
5	$O_2^- + O \rightarrow O^- + O_2$	3.3×10^{-10}	9
6	$O_2^- + O_2 \xrightarrow{M} O_4^-$	$3.5 \times 10^{-31} \times (T/300)^{-1}$	9
7	$O_2^- + O_3 \rightarrow O_3^- + O_2$	4×10^{-10}	9
8	$O_3^- + O \rightarrow O_2^- + O_2$	3.2×10^{-10}	9
9	$O_4^- \xrightarrow{M} O_2^- + O_2$	$10^{-10} \times \exp(-1044/T)$	9

10	$O_4^- + O \rightarrow O_3^- + O_2$	4×10^{-10}	9
11	$O_4^- + O \rightarrow O^- + 2O_2$	3×10^{-10}	9
12	$O_4^- + O_2(a) \rightarrow O_2^- + 2O_2$	10^{-10}	9
13	$O_4^- + O_2(b) \rightarrow O_2^- + 2O_2$	10^{-10}	9
14	$O^- + CO_2 \overset{M}{\rightarrow} CO_3^-$	$3.1 \times 10^{-28} \times (T/300)^{0.5}$	15
15	$O_2^- + CO_2 \overset{M}{\rightarrow} CO_4^-$	4.7×10^{-29}	6
16	$O_3^- + CO_2 \rightarrow CO_3^- + O_2$	$5.5 \times 10^{-10} \times (T/300)^{0.5}$	15
17	$O_4^- + CO_2 \rightarrow CO_4^- + O_2$	$4.3 \times 10^{-10} \times (T/300)^{0.5}$	15
18	$O^- + NO \overset{M}{\rightarrow} NO_2^-$	10^{-29}	9
19	$O^- + NO_2 \rightarrow NO_2^- + O$	1.2×10^{-9}	9
20	$O^- + N_2O \rightarrow NO^- + NO$	2×10^{-10}	9
21	$O_2^- + NO_2 \rightarrow NO_2^- + O_2$	8×10^{-10}	9
22	$O_2^- + NO_3 \rightarrow NO_3^- + O_2$	5×10^{-10}	9
23	$O_3^- + NO \rightarrow NO_2^- + O_2$	2.6×10^{-12}	9
24	$O_3^- + NO \rightarrow NO_3^- + O$	10^{-11}	9
25	$O_3^- + NO_2 \rightarrow NO_2^- + O_3$	7×10^{-10}	9
26	$O_3^- + NO_2 \rightarrow NO_3^- + O_2$	2×10^{-11}	9
27	$O_3^- + NO_3 \rightarrow NO_3^- + O_3$	5×10^{-10}	9
28	$NO^- + O_2 \rightarrow O_2^- + NO$	5×10^{-10}	9
29	$NO^- + NO_2 \rightarrow NO_2^- + NO$	7.4×10^{-16}	9
30	$NO^- + N_2O \rightarrow NO_2^- + N_2$	2.8×10^{-14}	9
31	$NO_2^- + O_3 \rightarrow NO_3^- + O_2$	1.8×10^{-11}	9
32	$NO_2^- + NO_2 \rightarrow NO_3^- + NO$	4×10^{-12}	9
33	$NO_2^- + NO_3 \rightarrow NO_3^- + NO_2$	5×10^{-10}	9
34	$NO_3^- + NO \rightarrow NO_2^- + NO_2$	3×10^{-15}	9
35	$NO_2^- + N_2O_5 \rightarrow NO_3^- + NO_3 + NO$	7×10^{-10}	9
36	$CO_3^- + O \rightarrow O_2^- + CO_2$	$1.1 \times 10^{-10} \times (T/300)^{0.5}$	15
37	$CO_3^- + NO \rightarrow NO_2^- + CO_2$	$1.1 \times 10^{-10} \times (T/300)^{0.5}$	15
38	$CO_3^- + NO_2 \rightarrow NO_3^- + CO_2$	$2 \times 10^{-10} \times (T/300)^{0.5}$	15
39	$CO_4^- + O \rightarrow CO_3^- + O_2$	$1.4 \times 10^{-10} \times (T/300)^{0.5}$	15
40	$CO_4^- + O_3 \rightarrow O_3^- + CO_2 + O_2$	$1.3 \times 10^{-10} \times (T/300)^{0.5}$	15
41	$CO_4^- + NO \rightarrow NO_3^- + CO_2$	4.8×10^{-11}	3

42	$O^- + H_2O \overset{M}{\rightarrow} O^-(H_2O)$	1.3×10^{-28}	3
43	$O_2^- + H_2O \overset{M}{\rightarrow} O_2^-(H_2O)$	2.2×10^{-28}	3
44	$O_3^- + H_2O \overset{M}{\rightarrow} O_3^-(H_2O)$	2.7×10^{-28}	3
45	$O^-(H_2O) + O_2 \rightarrow O_3^- + H_2O$	6.2×10^{-11}	3
46	$O_2^- + HNO_3 \rightarrow NO_3^- + HO_2$	2.9×10^{-9}	3
47	$O_2^-(H_2O) + NO_2 \rightarrow NO_2^- + H_2O + O_2$	9×10^{-10}	3
48	$O_2^-(H_2O) + NO \rightarrow NO_3^- + H_2O$	3.1×10^{-10}	3
49	$O_2^-(H_2O) + O_3 \rightarrow O_3^- + H_2O + O_2$	8×10^{-10}	3
50	$O_3^-(H_2O) + CO_2 \rightarrow CO_3^- + H_2O + O_2$	1.8×10^{-10}	3
51	$O_2^-(H_2O) + CO_2 \rightarrow CO_4^- + H_2O$	5.8×10^{-10}	3
52	$CO_3^- + HNO_3 \rightarrow NO_3^- + OH + CO_2$	3.51×10^{-10}	3
53	$NO_2^- + H \rightarrow OH^- + NO$	$3 \times 10^{-10} \times (T/300)^{0.5}$	15
54	$OH^- + O_3 \rightarrow O_3^- + OH$	$9 \times 10^{-10} \times (T/300)^{0.5}$	15
55	$OH^- + CO_2 \overset{M}{\rightarrow} HCO_3^-$	$7.6 \times 10^{-28} \times (T/300)^{0.5}$	15
56	$O^- + HCl \rightarrow Cl^- + OH$	$2 \times 10^{-9} \times (T/300)^{0.5}$	15
57	$O_2^- + HCl \rightarrow Cl^- + HO_2$	$1.6 \times 10^{-9} \times (T/300)^{0.5}$	15
58	$O_2^- + HBr \rightarrow Br^- + HO_2$	5.2×10^{-10}	8
59	$CO_3^- + H \rightarrow OH^- + CO_2$	1.7×10^{-10}	6
60	$OH^- + HCl \rightarrow Cl^- + H_2O$	10^{-10}	8
61	$OH^- + HBr \rightarrow Br^- + H_2O$	1.5×10^{-9}	8
62	$NO_2^- + HCl \rightarrow Cl^- + HNO_2$	1.4×10^{-9}	8
63	$NO_3^- + HCl \rightarrow Cl^- + HNO_3$	10^{-12}	8
64	$NO_3^- + HBr \rightarrow Br^- + HNO_3$	3.3×10^{-10}	8
65	$CO_3^- + HCl \rightarrow Cl^- + OH + CO_2$	3×10^{-11}	7
66	$Cl^- + NO_2 \rightarrow NO_2^- + Cl$	6×10^{-12}	7
67	$Cl^- + HNO_3 \rightarrow NO_3^- + HCl$	1.6×10^{-9}	8
68	$Br^- + HNO_3 \rightarrow NO_3^- + HBr$	7.0×10^{-10}	8
69	$Cl^- + O_3 \rightarrow ClO^- + O_2$	5×10^{-13}	8
70	$Br^- + O_3 \rightarrow BrO^- + O_2$	5.0×10^{-13}	8
71	$ClO^- + O_3 \rightarrow Cl^- + 2O_2$	6×10^{-11}	8
72	$BrO^- + O_3 \rightarrow Br^- + 2O_2$	6.0×10^{-11}	8
73	$ClO^- + O_3 \rightarrow O_3^- + ClO + O_2$	10^{-11}	8

74	$ClO^- + NO \rightarrow NO_2^- + Cl$	2.9×10^{-11}	8
75	$Cl^- + H_2O \overset{M}{\rightarrow} Cl^-(H_2O)$	$2 \times 10^{-29} \times (T/300)^{-2}$	8
76	$Cl^-(H_2O) \overset{M}{\rightarrow} Cl^- + H_2O$	$9.2 \times 10^{-6} \times (T/300)^{-3} \times \exp(-7450/T)$	8
77	$Cl^-(H_2O) + H \rightarrow e^- + HCl + H_2O$	8×10^{-11}	8
78	$Br^- + H \rightarrow e^- + HBr$	9.6×10^{-10}	8
79	$Cl^- + CO_2 \overset{M}{\rightarrow} Cl^-(CO_2)$	$6 \times 10^{-29} \times (T/300)^{-2}$	8
80	$Cl^-(CO_2) \overset{M}{\rightarrow} Cl^- + CO_2$	$2.6 \times 10^{-5} \times (T/300)^{-3} \times \exp(-4000/T)$	8
81	$Cl^- + HCl \overset{M}{\rightarrow} Cl^-(HCl)$	10^{-27}	6
82	$Cl^-(H_2O) + HCl \rightarrow Cl^-(HCl) + H_2O$	1.3×10^{-9}	6
83	$Cl^-(HCl) \overset{M}{\rightarrow} Cl^- + HCl$	$3.33 \times 10^{-3} \times (T/300)^{-1} \times \exp(-11926/T)$	6
Electron-ion recombination			
1	$e^- + N_2^+ \rightarrow N + N$	$2.8 \times 10^{-7} \times (T/300)^{-0.5}$	9
2	$e^- + N_2^+ \rightarrow N + N(^2D)$	$2 \times 10^{-7} \times (T/300)^{-0.5}$	9
3	$e^- + O_2^+ \rightarrow O + O$	$3.84 \times 10^{-8} \times (T/300)^{-0.7}$	15
4	$e^- + O_2^+ \rightarrow O + O(^1D)$	$1.13 \times 10^{-7} \times (T/300)^{-0.7}$	15
5	$e^- + O_2^+ \rightarrow O(^1D) + O(^1D)$	$8.88 \times 10^{-8} \times (T/300)^{-0.7}$	15
6	$e^- + O_2^+ \overset{M}{\rightarrow} O_2$	$6 \times 10^{-27} \times (T/300)^{-1.5}$	9
7	$e^- + N_2^+ \overset{M}{\rightarrow} N_2$	$6 \times 10^{-27} \times (T/300)^{-1.5}$	9
8	$e^- + NO^+ \overset{M}{\rightarrow} NO$	$6 \times 10^{-27} \times (T/300)^{-1.5}$	9
9	$e^- + N^+ \overset{M}{\rightarrow} N$	$6 \times 10^{-27} \times (T/300)^{-1.5}$	9
10	$e^- + O^+ \overset{M}{\rightarrow} O$	$6 \times 10^{-27} \times (T/300)^{-1.5}$	9
11	$e^- + N_4^+ \rightarrow N_2 + N_2$	$2 \times 10^{-6} \times (T/300)^{-0.5}$	9
12	$e^- + N_4^+ \rightarrow 2N + N_2$	$1.4 \times 10^{-6} \times (T/300)^{-0.41}$	3
13	$e^- + O_4^+ \rightarrow O_2 + O_2$	$1.4 \times 10^{-6} \times (T/300)^{-0.5}$	9
14	$e^- + O_4^+ \rightarrow 2O + O_2$	1.7×10^{-7}	10
15	$e^- + NO^+ \rightarrow N + O$	$4 \times 10^{-7} \times (T/300)^{-1.5}$	9
16	$e^- + NO^+ \rightarrow N(^2D) + O$	$3 \times 10^{-7} \times (T/300)^{-1}$	9
17	$e^- + N^+ \rightarrow N$	$4 \times 10^{-12} \times (T/300)^{-0.58}$	6
18	$e^- + O^+ \rightarrow O$	$3.24 \times 10^{-12} \times (T/300)^{-0.66}$	6
19	$e^- + NO^+(N_2) \rightarrow NO + N_2$	$1.3 \times 10^{-6} \times (T/300)^{-0.5}$	9

20	$e^- + NO^+(O_2) \rightarrow NO + O_2$	$1.3 \times 10^{-6} \times (T/300)^{-0.5}$	9
21	$e^- + N_2O_2^+ \rightarrow O_2 + N_2$	$1.3 \times 10^{-6} \times (T/300)^{-0.5}$	9
22	$e^- + NO_2^+ \rightarrow NO + O$	$2 \times 10^{-7} \times (T/300)^{-0.5}$	9
23	$e^- + N_2O^+ \rightarrow O + N_2$	$1.3 \times 10^{-6} \times (T/300)^{-0.5}$	9
24	$e^- + N_3^+ \rightarrow N + N_2$	$3.5 \times 10^{-6} \times (T/300)^{-0.5}$	3
25	$e^- + N_3^+ \rightarrow N + N_2(A)$	$4.3 \times 10^{-7} \times (T/300)^{-0.5}$	3
26	$e^- + N_3^+ \rightarrow N + N_2(B)$	$4.3 \times 10^{-7} \times (T/300)^{-0.5}$	3
27	$e^- + H_2O^+ \rightarrow O + 2H$	$3.05 \times 10^{-7} \times (T/300)^{-0.5}$	17
28	$e^- + H_2O^+ \rightarrow OH + H$	$8.6 \times 10^{-8} \times (T/300)^{-0.5}$	17
29	$e^- + H_2O^+ \rightarrow O + H_2$	$3.9 \times 10^{-8} \times (T/300)^{-0.5}$	17
30	$e^- + OH^+ \rightarrow O + H$	$3.75 \times 10^{-8} \times (T/300)^{-0.5}$	17
31	$e^- + H^+(H_2O) \rightarrow OH + 2H$	$2.58 \times 10^{-7} \times (T/300)^{-0.5}$	17
32	$e^- + H^+(H_2O) \rightarrow H + H_2O$	$1.08 \times 10^{-7} \times (T/300)^{-0.5}$	17
33	$e^- + H^+(H_2O) \rightarrow OH + H_2$	$6.02 \times 10^{-8} \times (T/300)^{-0.5}$	17
34	$e^- + H^+(H_2O) \rightarrow O + H + H_2$	$5.6 \times 10^{-9} \times (T/300)^{-0.5}$	17
35	$e^- + H^+(H_2O)_2 \rightarrow H + 2H_2O$	$2.6 \times 10^{-6} \times (T/300)^{-0.5}$	6
36	$e^- + H^+(H_2O)_3 \rightarrow H + 3H_2O$	$3.8 \times 10^{-6} \times (T/300)^{-0.5}$	6
37	$e^- + H^+(H_2O)_4 \rightarrow H + 4H_2O$	$4.9 \times 10^{-6} \times (T/300)^{-0.5}$	6
38	$e^- + H^+(H_2O)_5 \rightarrow H + 5H_2O$	$5 \times 10^{-6} \times (T/300)^{-0.5}$	6
39	$e^- + H^+(H_2O)_6 \rightarrow H + 6H_2O$	$6.2 \times 10^{-6} \times (T/300)^{-0.5}$	6
40	$e^- + H^+(H_2O)_7 \rightarrow H + 7H_2O$	$8.27 \times 10^{-6} \times (T/300)^{-0.5}$	6
41	$e^- + H^+(H_2O)(OH) \rightarrow H + H_2O + OH$	$1.5 \times 10^{-6} \times (T/300)^{-0.5}$	6
42	$e^- + H^+(H_2O)(CO_2) \rightarrow H + H_2O + CO_2$	$2 \times 10^{-6} \times (T/300)^{-0.5}$	6
43	$e^- + H^+(H_2O)_2(CO_2) \rightarrow H + 2H_2O + CO_2$	$3 \times 10^{-6} \times (T/300)^{-0.5}$	6
44	$e^- + H^+(H_2O)(N_2) \rightarrow H + H_2O + N_2$	$1.5 \times 10^{-6} \times (T/300)^{-0.5}$	6
45	$e^- + H^+(H_2O)_2(N_2) \rightarrow H + 2H_2O + N_2$	$1.5 \times 10^{-6} \times (T/300)^{-0.5}$	6
46	$e^- + O_2^+(H_2O) \rightarrow H_2O + O_2$	$2 \times 10^{-6} \times (T/300)^{-0.5}$	6
47	$e^- + NO^+(H_2O) \rightarrow NO + H_2O$	$1.5 \times 10^{-6} \times (T/300)^{-0.5}$	6
48	$e^- + NO^+(H_2O)_2 \rightarrow NO + 2H_2O$	$2 \times 10^{-6} \times (T/300)^{-0.5}$	6
49	$e^- + NO^+(H_2O)_3 \rightarrow NO + 3H_2O$	$2 \times 10^{-6} \times (T/300)^{-0.5}$	6
50	$e^- + NO^+(CO_2) \rightarrow NO + CO_2$	$1.5 \times 10^{-6} \times (T/300)^{-0.5}$	6
51	$e^- + NO^+(H_2O)(CO_2) \rightarrow NO + H_2O + CO_2$	$2 \times 10^{-6} \times (T/300)^{-0.5}$	6
52	$e^- + NO^+(H_2O)_2(CO_2) \rightarrow NO + 2H_2O + CO_2$	$2 \times 10^{-6} \times (T/300)^{-0.5}$	6

53	$e^- + NO^+(H_2O)(N_2) \rightarrow NO + H_2O + N_2$	$2 \times 10^{-6} \times (T/300)^{-0.5}$	6
54	$e^- + NO^+(H_2O)_2(N_2) \rightarrow NO + 2H_2O + N_2$	$2 \times 10^{-6} \times (T/300)^{-0.5}$	6
Ion-ion recombination			
1	$A^- + B^+ \rightarrow A + B$	$2 \times 10^{-7} \times (T/300)^{-0.5}$	9
	For $A^- = [O^-, O_2^-, O_3^-, NO^-, NO_2^-, NO_3^-]$		
	And $B^+ = [O^+, O_2^+, N^+, N_2^+, NO^+, NO_2^+, N_2O^+]$		
2	$A^- + (BC)^+ \rightarrow A + B + C$	10^{-7}	9
	For $A^- = [O^-, O_2^-, O_3^-, NO^-, NO_2^-, NO_3^-]$		
	And $(BC)^+ = [O_2^+, N_2^+, NO^+, NO_2^+, N_2O^+, N_3^+, N_4^+, NO^+(N_2), NO^+(O_2), N_2O_2^+]$		
3	$O_3^- + A^+ \rightarrow 2O_2 + A$	10^{-7}	9
	For $A^+ = [O^+, O_2^+, N^+, N_2^+, NO^+, NO_2^+, N_2O^+]$		
4	$O_4^- + (AB)^+ \rightarrow 2O_2 + A + B$	10^{-7}	9
	For $(AB)^+ = [N_3^+, N_4^+, O_4^+, NO^+(N_2), NO^+(O_2), N_2O_2^+]$		
5	$A^- + B^+ \xrightarrow{M} A + B$	$2 \times 10^{-25} \times (T/300)^{-2.5}$	9
	For $A^- = [O^-, O_2^-]$		
	And $B^+ = [O^+, O_2^+, N^+, N_2^+, NO^+]$		
6	$A^- + B^+ \xrightarrow{M} AB$	$2 \times 10^{-25} \times (T/300)^{-2.5}$	9
	For $A^- = O_2^-$		
	And $B^+ = [O^+, N^+, NO^+]$		
7	$A^- + B^+ \xrightarrow{M} AB$	$2 \times 10^{-25} \times (T/300)^{-2.5}$	9
	For $A^- = O^-$		
	And $B^+ = [O^+, O_2^+, N^+, N_2^+, NO^+]$		
8a	$X^- + Y^+ \rightarrow X + Y$	$6 \times 10^{-8} \times (T/300)^{-0.5}$	1
8b	$X^- + Y^+ \xrightarrow{M} X + Y$	$1.25 \times 10^{-25} \times (T/300)^{-4}$	1
	For all X^-/Y^+ combinations not included in 1-7		
Neutral chemistry			
1	$N + O_2 \rightarrow NO + O$	$1.5 \times 10^{-11} \times \exp(-3600/T)$	14
2	$N + O_3 \rightarrow NO + O_2$	10^{-16}	14
3	$N + NO \rightarrow N_2 + O$	$2.1 \times 10^{-11} \times \exp(-100/T)$	14
4	$N + NO_2 \rightarrow N_2O + O$	3×10^{-12}	9
5	$N + NO_2 \rightarrow NO + NO$	2.3×10^{-12}	9

6	$N + NO_2 \rightarrow N_2 + 2O$	9.1×10^{-13}	9
7	$N + NO_2 \rightarrow N_2 + O_2$	7×10^{-13}	9
8	$N + N \xrightarrow{M} N_2$	$8.27 \times 10^{-34} \times \exp(500/T)$	9
9	$N + O \xrightarrow{M} NO$	$1.76 \times 10^{-31} \times T^{-0.5}$	9
10	$O + O_3 \rightarrow O_2 + O_2$	$8 \times 10^{-12} \times \exp(-2060/T)$	14
11	$O + NO_2 \rightarrow NO + O_2$	$5.1 \times 10^{-12} \times \exp(210/T)$	14
12	$O + NO_3 \rightarrow NO_2 + O_2$	10^{-11}	14
13	$O + O + N_2 \rightarrow O_2 + N_2$	$2.76 \times 10^{-34} \times \exp(720/T)$	15
14	$O + O + O_2 \rightarrow O_2 + O_2$	$3.81 \times 10^{-33} \times (T/300)^{-0.63}$	15
15	$O + O_2 \xrightarrow{M} O_3$	$6 \times 10^{-34} \times (T/300)^{-2.4}$	14
16	$O + NO \xrightarrow{M} NO_2$	$9 \times 10^{-32} \times (T/300)^{-1.5}$	14
17	$O + O_3 + O_2 \rightarrow O_3 + O_3 + O_2$	$1.5 \times 10^{-34} \times \exp(750/T)$	3
18	$O + O + O_2 \rightarrow O_2 + O_3 + O$	$2.15 \times 10^{-34} \times \exp(345/T)$	3
19	$O + NO_2 \xrightarrow{M} NO_3$	$2.5 \times 10^{-31} \times (T/300)^{-1.8}$	14
20	$O + NO \rightarrow NO_2$	$3.02 \times 10^{-11} \times (T/300)^{-0.75}$	3
21	$NO + NO_3 \rightarrow NO_2 + NO_2$	$1.5 \times 10^{-11} \times \exp(170/T)$	14
22	$NO + O_3 \rightarrow NO_2 + O_2$	$3 \times 10^{-12} \times \exp(-1500/T)$	14
23	$NO_2 + O_3 \rightarrow NO_3 + O_2$	$1.2 \times 10^{-13} \times \exp(-2450/T)$	14
24	$NO_2 + NO_3 \rightarrow NO + NO_2 + O_2$	$2.3 \times 10^{-13} \times \exp(-1600/T)$	9
25	$NO_2 + NO_3 \xrightarrow{M} N_2O_5$	$2.4 \times 10^{-30} \times (T/300)^{-3}$	14
26	$NO_3 + NO_3 \rightarrow NO_2 + NO_2 + O_2$	$8.5 \times 10^{-13} \times \exp(-2450/T)$	14
27	$H + O_2 \xrightarrow{M} HO_2$	$4.4 \times 10^{-32} \times (T/300)^{-1.3}$	14
28	$H + H_2 + O_2 \rightarrow HO_2 + H_2 + O_2$	$5.79 \times 10^{-32} \times (T/300)^{-0.8}$	3
29	$H + OH \xrightarrow{M} H_2O$	$6.88 \times 10^{-31} \times (T/300)^{-2}$	3
30	$H + NO_2 \rightarrow NO + OH$	$2.2 \times 10^{-10} \times \exp(-182/T)$	3
31	$H + O_3 \rightarrow OH(v) + O_2$	$1.4 \times 10^{-10} \times \exp(-470/T)$	15
32	$O + HO_2 \rightarrow OH(v) + O_2$	$3 \times 10^{-11} \times (1. - 0.52)$	18
33	$O + HO_2 \rightarrow OH + O_2$	$3 \times 10^{-11} \times \exp(200/T)$	14
34	$OH(v) + O \rightarrow H + O_2$	$2.5 \times 10^{-10} \times (T/300)^{0.5}$	15
35	$OH(v) \xrightarrow{M} OH$	$10^{-13} \times (T/300)^{0.5}$	15
36	$H + O_3 \rightarrow HO_2 + O$	7.5×10^{-13}	3

37	$H + HO_2 \rightarrow OH + OH$	7.2×10^{-11}	14
38	$H + HO_2 \rightarrow O + H_2O$	1.6×10^{-12}	14
39	$H + HO_2 \rightarrow H_2 + O_2$	6.9×10^{-12}	14
40	$H + NO_3 \rightarrow NO_2 + OH$	$5.8 \times 10^{-10} \times \exp(-750/T)$	3
41	$OH + OH \rightarrow H_2O + O$	1.8×10^{-12}	14
42	$OH + O \rightarrow H + O_2$	$1.8 \times 10^{-11} \times \exp(180/T)$	14
43	$OH + H_2 \rightarrow H_2O + H$	$2.8 \times 10^{-12} \times \exp(-1800/T)$	14
44	$OH + O_3 \rightarrow HO_2 + O_2$	$1.7 \times 10^{-12} \times \exp(-940/T)$	14
45	$OH + HO_2 \rightarrow H_2O + O_2$	$4.8 \times 10^{-11} \times \exp(250/T)$	14
46	$OH + HNO_2 \rightarrow H_2O + NO_2$	$1.8 \times 10^{-11} \times \exp(-390/T)$	3
47	$OH + N \rightarrow NO + H$	$3.92 \times 10^{-11} \times \exp(72.3/T)$	3
48	$OH + NO \xrightarrow{M} HNO_2$	$7.4 \times 10^{-31} \times (T/300)^{-2.4}$	3
49	$OH + NO_2 \xrightarrow{M} HNO_3$	$1.8 \times 10^{-30} \times (T/300)^{-3}$	14
50	$OH + NO_3 \rightarrow HO_2 + NO_2$	2.2×10^{-11}	3
51	$OH + HNO_3 \rightarrow H_2O + NO_3$	$7.2 \times 10^{-15} \times \exp(785/T)$	3
52	$OH + HO_2 \rightarrow H_2O + O_2$	$1.7 \times 10^{-11} \times \exp(416/T)$	15
53	$HO_2 + O_3 \rightarrow OH + O_2 + O_2$	$1 \times 10^{-14} \times \exp(-490/T)$	14
54	$HO_2 + NO \rightarrow NO_2 + OH$	$3.3 \times 10^{-12} \times \exp(270/T)$	14
55	$HO_2 + NO_2 \rightarrow HNO_2 + O_2$	5×10^{-16}	14
56	$HO_2 + NO_3 \rightarrow HNO_3 + O_2$	9.21×10^{-13}	3
57	$HO_2 + N \rightarrow OH + NO$	2.19×10^{-11}	3
58	$N_2O_5 + H_2O \rightarrow HNO_3 + HNO_3$	5×10^{-19}	3
59	$N_2O_5 + O \rightarrow N_2 + 3O_2$	$3 \times 10^{-16} \times (T/300)^{0.5}$	3
60	$HNO_2 + O \rightarrow OH + NO_2$	$10^{-12} \times \exp(-2000/T)$	3
61	$HNO_2 + NO_3 \rightarrow HNO_3 + NO_2$	2×10^{-15}	3
62	$H + NO \xrightarrow{M} HNO$	$7.32 \times 10^{-32} \times (T/300)^{-1.318} \times \exp(-184.3/T)$	3
63	$HO_2 + NO \rightarrow O_2 + HNO$	$9.1 \times 10^{-19} \times (T/300) \times \exp(2819/T)$	3
64	$HNO + H \rightarrow H_2 + NO$	$2.35 \times 10^{-11} \times (T/300)^{0.94} \times \exp(-249/T)$	3
65	$HNO + OH \rightarrow H_2O + NO$	$1.26 \times 10^{-11} \times (T/300)^{0.99} \times \exp(-334.2/T)$	3
66	$OH + OH \xrightarrow{M} H_2O_2$	$6.9 \times 10^{-31} \times (T/300)^{-1}$	14
67	$HO_2 + HO_2 \rightarrow H_2O_2 + O_2$	$3 \times 10^{-13} \times \exp(460/T)$	14
68	$HO_2 + HO_2 \xrightarrow{M} H_2O_2 + O_2$	$2.1 \times 10^{-33} \times \exp(920/T)$	14

69	$H_2O_2 + H \rightarrow H_2O + OH$	$4 \times 10^{-11} \times \exp(-2000/T)$	3
70	$H_2O_2 + H \rightarrow HO_2 + H_2$	$8 \times 10^{-11} \times \exp(-4000/T)$	3
71	$H_2O_2 + OH \rightarrow HO_2 + H_2O$	1.8×10^{-12}	14
72	$H_2O_2 + O \rightarrow HO_2 + OH$	$1.79 \times 10^{-13} \times (T/300)^{2.92} \times \exp(-1394/T)$	3
73	$H_2O_2 + NO_3 \rightarrow HO_2 + HNO_3$	4.1×10^{-16}	3
74	$Cl + O_3 \rightarrow ClO + O_2$	$2.3 \times 10^{-11} \times \exp(-200/T)$	14
75	$Cl + H_2O_2 \rightarrow HCl + HO_2$	$1.1 \times 10^{-11} \times \exp(-980/T)$	14
76	$Cl + H_2 \rightarrow HCl + H$	$3.05 \times 10^{-11} \times \exp(-2270/T)$	14
77	$Cl + HO_2 \rightarrow HCl + O_2$	$1.4 \times 10^{-11} \times \exp(270/T)$	14
78	$Cl + HO_2 \rightarrow ClO + OH$	$3.6 \times 10^{-11} \times \exp(-375/T)$	14
79	$ClO + O \rightarrow Cl + O_2$	$2.8 \times 10^{-11} \times \exp(85/T)$	14
80	$ClO + HO_2 \rightarrow HOCl + O_2$	$2.6 \times 10^{-10} \times \exp(290/T)$	14
81	$ClO + NO \rightarrow Cl + NO_2$	$6.4 \times 10^{-12} \times \exp(290/T)$	14
82	$ClO + NO_2 \xrightarrow{M} ClONO_2$	$1.8 \times 10^{-29} \times (T/300)^{-3.4}$	14
83	$ClONO_2 + O \rightarrow ClO + NO_3$	$3.6 \times 10^{-10} \times \exp(-840/T)$	14
84	$ClO + OH \rightarrow Cl + HO_2$	$7.4 \times 10^{-12} \times \exp(-270/T)$	14
85	$ClO + OH \rightarrow HCl + O_2$	$6 \times 10^{-13} \times \exp(-230/T)$	14
86	$HCl + OH \rightarrow HCl + O_2$	$1.8 \times 10^{-12} \times \exp(-250/T)$	14
87	$HCl + O \rightarrow Cl + OH$	$10^{-11} \times \exp(-3300/T)$	14
88	$ClO + ClO \xrightarrow{M} Cl_2O_2$	$1.9 \times 10^{-30} \times (T/300)^{-3.6}$	14
89	$HOCl + OH \rightarrow ClO + H_2O$	$3 \times 10^{-10} \times \exp(-500/T)$	14
90	$HOCl + O \rightarrow ClO + OH$	1.7×10^{-11}	14
91	$Cl + CH_4 \rightarrow HCl + CH_3$	$7.1 \times 10^{-10} \times \exp(-1270/T)$	14
92	$BrO + HO_2 \rightarrow HOBr + O_2$	$4.5 \times 10^{-10} \times \exp(460/T)$	14
93	$BrO + NO_2 \xrightarrow{M} BrONO_2$	$5.4 \times 10^{-29} \times (T/300)^{-3.1}$	14
94	$BrONO_2 + O \rightarrow BrO + NO_3$	$1.9 \times 10^{-9} \times \exp(215/T)$	14
95	$Br + CH_2O \rightarrow HBr + CHO$	$1.7 \times 10^{-9} \times \exp(-800/T)$	14
96	$BrO + ClO \rightarrow Br + OClO$	$9.5 \times 10^{-11} \times \exp(550/T)$	14
97	$BrO + ClO \rightarrow Br + Cl + O_2$	$2.3 \times 10^{-10} \times \exp(260/T)$	14
98	$BrO + ClO \rightarrow BrCl + O_2$	$4.1 \times 10^{-11} \times \exp(290/T)$	14
99	$BrO + BrO \rightarrow 2Br + O_2$	$1.5 \times 10^{-10} \times \exp(230/T)$	14
100	$HBr + O \rightarrow Br + OH$	$5.8 \times 10^{-10} \times \exp(-1500/T)$	14

101	$Br_2 + OH \rightarrow Br + HOBr$	$2.1 \times 10^{-9} \times \exp(240/T)$	14
102	$CO + OH \rightarrow H + CO_2$	1.505×10^{-11}	14
103	$OH + CH_4 \rightarrow H_2O + CH_3$	$2.45 \times 10^{-10} \times \exp(-1775/T)$	14
104	$O_2 + CH_3 \xrightarrow{M} CH_3O_2$	$4 \times 10^{-29} \times (T/300)^{-4.7}$	14
105	$O + CH_3 \rightarrow CH_2O$	1.1×10^{-8}	14
106	$NO + CH_3O_2 \rightarrow NO_2 + CH_3O$	$2.8 \times 10^{-10} \times \exp(300/T)$	14
107	$HO_2 + CH_3O_2 \rightarrow O_2 + CH_3OOH$	$4.1 \times 10^{-11} \times \exp(750/T)$	14
108	$CH_3O_2 + CH_3O_2 \rightarrow CH_3O + CH_3O + O_2$	$9.5 \times 10^{-12} \times \exp(390/T)$	14
109	$CH_3O + O_2 \rightarrow HO_2 + CH_2O$	$3.9 \times 10^{-12} \times \exp(-900/T)$	14
110	$OH + CH_3OOH \rightarrow H_2O + CH_3O_2$	$3.8 \times 10^{-10} \times \exp(200/T)$	14
111	$OH + CH_2O \rightarrow H_2O + CHO$	$5.5 \times 10^{-10} \times \exp(125/T)$	14
112	$O + CH_2O \rightarrow OH + CHO$	$3.4 \times 10^{-9} \times \exp(-1600/T)$	14
113	$CHO + O_2 \rightarrow HO_2 + CO$	5.2×10^{-10}	14
114	$O_3 + CH_3 \rightarrow CH_3O_3$	$5.4 \times 10^{-10} \times \exp(-220/T)$	14
115	$HO_2 + CH_2O \rightarrow H_2O_2$	$6.7 \times 10^{-13} \times \exp(600/T)$	14
116	$NO_2 + CH_3O_2 \xrightarrow{M} HNO_3 + CH_2O$	$1 \times 10^{-28} \times (T/300)^{-4.8}$	14
117	$N(^2D) + O_2 \rightarrow NO + O$	$1.5 \times 10^{-12} \times (T/300)^{0.5}$	9
118	$N(^2D) + O_2 \rightarrow NO + O(^1D)$	$6 \times 10^{-12} \times (T/300)^{0.5}$	9
119	$N(^2D) + N_2 \rightarrow N + N_2$	6×10^{-15}	9
120	$N(^2D) + O \rightarrow N + O(^1D)$	$4 \times 10^{-13} \times (T/300)^{0.5}$	15
121	$N(^2D) + O \rightarrow N + O$	$4.5 \times 10^{-13} \times (T/300)^{0.5}$	15
122	$N(^2D) + N_2O \rightarrow NO + N_2$	3.5×10^{-12}	3
123	$N(^2D) + NO \rightarrow N_2 + O$	1.8×10^{-10}	3
124	$N(^2D) + NO \rightarrow N_2O$	6×10^{-11}	9
125	$N(^2P) + O_2 \rightarrow NO + O$	2.6×10^{-12}	9
126	$N(^2P) + N_2 \rightarrow N(^2D) + N_2$	2×10^{-18}	9
127	$N(^2P) + N \rightarrow N(^2D) + N$	1.8×10^{-12}	9
128	$N(^2P) + NO \rightarrow O + N_2$	3×10^{-11}	3
129	$O(^1D) + N_2 \rightarrow O + N_2$	$2.15 \times 10^{-11} \times \exp(110/T)$	14
130	$O(^1D) + O_2 \rightarrow O + O_2$	$3.3 \times 10^{-11} \times \exp(55/T)$	14
131	$O(^1D) + O_2 \rightarrow O + O_2(a)$	$3.3 \times 10^{-11} \times \exp(55/T)$	14
132	$O(^1D) + O_2 \rightarrow O + O_2(b)$	$3.3 \times 10^{-11} \times \exp(55/T)$	14
133	$O(^1D) + O_3 \rightarrow 2O + O_2$	2.4×10^{-10}	14

134	$O(^1D) + O_3 \rightarrow O_2 + O_2$	2.4×10^{-10}	4
135	$O(^1D) + O_3 \rightarrow O + O_3$	2.4×10^{-10}	14
136	$O(^1D) + N_2O \rightarrow NO + NO$	$1.19 \times 10^{-10} \times \exp(20/T)$	14
137	$O(^1D) + N_2O \rightarrow N_2 + O_2$	$1.19 \times 10^{-10} \times \exp(20/T)$	14
138	$O(^1D) + N_2O \rightarrow O + N_2O$	$1.19 \times 10^{-10} \times \exp(20/T)$	14
139	$O(^1D) + NO \rightarrow N + O_2$	1.7×10^{-10}	9
140	$O(^1D) + NO_2 \rightarrow NO + O_2$	3×10^{-10}	3
141	$O(^1D) + H_2O \rightarrow OH + OH$	$1.63 \times 10^{-10} \times \exp(60/T)$	14
142	$O(^1D) + H_2O \rightarrow H_2 + O_2$	$1.63 \times 10^{-10} \times \exp(60/T)$	14
143	$O(^1D) + H_2 \rightarrow OH + H$	1.2×10^{-10}	14
144	$O(^1D) + H_2O_2 \rightarrow H_2O + O_2$	5.2×10^{-10}	3
145	$O(^1D) + CH_4 \rightarrow OH + CH_3$	1.75×10^{-8}	14
146	$O(^1D) + CH_4 \rightarrow H + CH_3O$	1.75×10^{-8}	14
147	$O(^1S) + H_2O \rightarrow OH + OH$	5×10^{-10}	3
148	$O(^1S) + H_2O \rightarrow H_2 + O_2$	5×10^{-10}	3
149	$O(^1S) + H_2O \rightarrow O + H_2O$	3×10^{-10}	3
150	$O(^1S) + O_2 \rightarrow O + O_2$	$4.3 \times 10^{-12} \times \exp(-850/T) \times 0.69$	9
151	$O(^1S) + O_2 \rightarrow O(^1D) + O_2$	$4.3 \times 10^{-12} \times \exp(-850/T) \times 0.31$	15
152	$O(^1S) + N_2 \rightarrow O + N_2$	5×10^{-17}	15
153	$O(^1S) + O_3 \rightarrow O(^1D) + O + O_2$	2.9×10^{-10}	9
154	$O(^1S) + O_3 \rightarrow O_2 + O_2$	2.9×10^{-10}	9
155	$O(^1S) + O \rightarrow O(^1D) + O$	$5 \times 10^{-11} \times \exp(-301/T)$	9
156	$O(^1S) + NO \rightarrow NO + O$	1.8×10^{-10}	9
157	$O(^1S) + NO \rightarrow O(^1D) + NO$	3.2×10^{-10}	9
158	$O(^1S) + N_2O \rightarrow N_2O + O$	6.3×10^{-12}	9
159	$O(^1S) + N_2O \rightarrow O(^1D) + N_2O$	3.1×10^{-12}	9
160	$O(^1S) + O_2(a) \rightarrow O(^1D) + O_2(b)$	3.6×10^{-11}	9
161	$O(^1S) + O_2(a) \rightarrow O + O + O$	3.4×10^{-11}	9
162	$O_2(a) + N_2 \rightarrow N_2 + O_2$	1.4×10^{-19}	3
163	$O_2(a) + O_2 \rightarrow O_2 + O_2$	$3.6 \times 10^{-18} \times \exp(-220/T)$	14
164	$O_2(a) + O \rightarrow O + O_2$	7×10^{-16}	9
165	$O_2(a) + N \rightarrow O + NO$	$2 \times 10^{-14} \times \exp(-600/T)$	9
166	$O_2(a) + NO \rightarrow O + NO_2$	4.88×10^{-18}	3

167	$O_2(a) + NO \rightarrow NO + O_2$	2.48×10^{-17}	18
168	$O_2(a) + O_3 \rightarrow O(^1D) + O_2 + O_2$	$5.2 \times 10^{-11} \times \exp(-2840/T)$	15
169	$O_2(a) + O_3 \rightarrow O + O_2 + O_2$	$5.2 \times 10^{-11} \times \exp(-2840/T)$	14
170	$O_2(a) + O_2(a) + O_2 \rightarrow O_3 + O_3 + O_2$	$10^{-31} \times (T/300)^{0.5}$	15
171	$O_2(a) + H_2O \rightarrow H_2O + O_2$	3×10^{-18}	3
172	$O_2(b) + N_2 \rightarrow N_2 + O_2(a)$	$1.8 \times 10^{-15} \times \exp(45/T)$	14
173	$O_2(b) + O_2 \rightarrow O_2 + O_2(a)$	$3.73 \times 10^{-16} \times (T/300)^{2.4} \times \exp(-241/T)$	3
174	$O_2(b) + O \rightarrow O_2 + O_2(a)$	8×10^{-14}	9
175	$O_2(b) + O \rightarrow O(^1D) + O_2$	$3.39 \times 10^{-11} \times (T/300)^{-0.1} \times \exp(-4201/T)$	9
176	$O_2(b) + O_3 \rightarrow 2O_2(a) + O$	$3.5 \times 10^{-11} \times \exp(-135/T)$	14
177	$O_2(b) + NO \rightarrow O_2(a) + NO$	4×10^{-14}	9
178	$O_2(b) + H_2O \rightarrow H_2O + O_2$	$3.9 \times 10^{-12} \times \exp(125/T)$	14
179	$N_2(A) + N_2 \rightarrow N_2 + N_2$	3×10^{-18}	9
180	$N_2(A) + O_2 \rightarrow N_2 + 2O$	$1.63 \times 10^{-12} \times (T/300)^{0.55}$	15
181	$N_2(A) + O_2 \rightarrow N_2O + O$	7.8×10^{-14}	9
182	$N_2(A) + O_2 \rightarrow N_2 + O_2(a)$	1.29×10^{-12}	15
183	$N_2(A) + O_2 \rightarrow N_2 + O_2(b)$	1.29×10^{-12}	15
184	$N_2(A) + O \rightarrow O(^1S) + N_2$	2.1×10^{-11}	9
185	$N_2(A) + O \rightarrow N(^2D) + NO$	7×10^{-12}	9
186	$N_2(A) + N \rightarrow N(^2P) + N_2$	5×10^{-11}	9
187	$N_2(A) + N \rightarrow N_2 + N$	2×10^{-11}	3
188	$N_2(A) + NO \rightarrow N_2 + NO$	7×10^{-11}	9
189	$N_2(A) + N_2O \rightarrow N_2 + N + NO$	10^{-11}	9
190	$N_2(A) + N_2(A) \rightarrow N_2(B) + N_2$	$3 \times 10^{-10} \times (T/300)^{0.5}$	15
191	$N_2(A) + N_2(A) \rightarrow N_2(C) + N_2$	$1.5 \times 10^{-10} \times (T/300)^{0.5}$	15
192	$N_2(A) + H_2O \rightarrow H + OH + N_2$	5×10^{-14}	3
193	$N_2(A) + O_2(a) \rightarrow N_2(B) + O_2$	$10^{-10} \times (T/300)^{0.5}$	15
194	$N_2(B) + O_2 \rightarrow N_2 + O + O$	3×10^{-10}	9
195	$N_2(B) + N_2 \rightarrow N_2(A) + N_2$	3×10^{-11}	3
196	$N_2(B) + N_2 \rightarrow N_2 + N_2$	2×10^{-12}	3
197	$N_2(B) + NO \rightarrow N_2(A) + NO$	2.4×10^{-10}	9
198	$N + N \xrightarrow{M} N_2(B)$	$2.4 \times 10^{-33} \times (T/300)^{0.5}$	15
199	$N_2(C) + O_2 \rightarrow O(^1S) + O + N_2$	3×10^{-10}	9

200	$N_2(C) + N_2 \rightarrow N_2(a'^1) + N_2$	10^{-11}	9
201	$N_2(a'^1) + O_2 \rightarrow N_2 + O + O$	2.8×10^{-11}	9
202	$N_2(a'^1) + N_2 \rightarrow N_2(B) + N_2$	4×10^{-15}	5
203	$N_2(a'^1) + NO \rightarrow N_2 + N + O$	3.6×10^{-10}	9
204	$N_2(a^1) + O_2 \rightarrow N_2 + O + O$	2.8×10^{-11}	3
205	$N_2(a^1) + N_2 \rightarrow N_2 + N_2$	2×10^{-13}	3
206	$N_2(a^1) + NO \rightarrow N_2 + N + O$	3.6×10^{-10}	3
207	$N_2(a^1) + H_2O \rightarrow N_2 + OH + H$	5×10^{-14}	3
208	$O_2 \xrightarrow{h\nu} O + O$	$f(h\nu)$	2
209	$O_3 \xrightarrow{h\nu} O_2 + O$	$f(h\nu)$	2
210	$O_3 \xrightarrow{h\nu} O_2 + O(^1D)$	$f(h\nu)$	2
211	$NO \xrightarrow{h\nu} N + O$	$f(h\nu)$	2
212	$NO_2 \xrightarrow{h\nu} NO + O$	$f(h\nu)$	2
213	$NO_3 \xrightarrow{h\nu} NO_2 + O$	$f(h\nu)$	2
214	$HNO_3 \xrightarrow{h\nu} NO_2 + OH$	$f(h\nu)$	2
215	$N_2O \xrightarrow{h\nu} O(^1D) + N_2$	$f(h\nu)$	2
216	$N_2O_5 \xrightarrow{h\nu} NO_2 + NO_3$	$f(h\nu)$	2
217	$N_2O_5 \xrightarrow{h\nu} O + NO + NO_2$	$f(h\nu)$	2
218	$H_2O \xrightarrow{h\nu} H + OH$	$f(h\nu)$	2
219	$HO_2 \xrightarrow{h\nu} O + OH$	$f(h\nu)$	2
220	$H_2O_2 \xrightarrow{h\nu} OH + OH$	$f(h\nu)$	2
221	$HCl \xrightarrow{h\nu} H + Cl$	$f(h\nu)$	2
222	$ClO \xrightarrow{h\nu} Cl + O$	$f(h\nu)$	2
223	$HO_2NO_2 \xrightarrow{h\nu} HO_2 + NO_2$	$f(h\nu)$	2
224	$HO_2NO_2 \xrightarrow{h\nu} OH + NO_3$	$f(h\nu)$	2
225	$HOCl \xrightarrow{h\nu} OH + Cl$	$f(h\nu)$	2
226	$HOBr \xrightarrow{h\nu} OH + Br$	$f(h\nu)$	2
227	$ClONO_2 \xrightarrow{h\nu} Cl + NO_3$	$f(h\nu)$	2
228	$BrONO_2 \xrightarrow{h\nu} Br + NO_3$	$f(h\nu)$	2

229	$Cl_2O_2 \xrightarrow{h\nu} 2Cl + O_2$	$f(h\nu)$	2
230	$Cl_2 \xrightarrow{h\nu} Cl + Cl$	$f(h\nu)$	2
231	$ClNO_2 \xrightarrow{h\nu} Cl + NO_2$	$f(h\nu)$	2
232	$OClO \xrightarrow{h\nu} ClO + O$	$f(h\nu)$	2
233	$BrONO_2 \xrightarrow{h\nu} BrO + NO_2$	$f(h\nu)$	2
234	$BrO \xrightarrow{h\nu} Br + O$	$f(h\nu)$	2
235	$BrCl \xrightarrow{h\nu} Cl + Br$	$f(h\nu)$	2
236	$CH_3OOH \xrightarrow{h\nu} OH + CH_3O$	$f(h\nu)$	2
237	$CH_2O \xrightarrow{h\nu} CHO + H$	$f(h\nu)$	2
238	$CH_2O \xrightarrow{h\nu} H_2 + CO$	$f(h\nu)$	2
239	$CH_4 \xrightarrow{h\nu} H + CH_3$	$f(h\nu)$	2
240	$Cl_2O_2 \xrightarrow{h\nu} ClO + ClO$	$f(h\nu)$	2
Radiative de-excitation			
1	$O(^1D) \rightarrow O + h\nu$	9.1×10^{-3}	15
2	$O(^1S) \rightarrow O(^1D) + h\nu$	1.43	15
3	$O_2(a) \rightarrow O_2 + h\nu$	2.22×10^{-4}	15
4	$O_2(b) \rightarrow O_2 + h\nu$	7.7×10^{-2}	15
5	$OH(v) \rightarrow OH + h\nu$	218	15
6	$N_2(B) \rightarrow N_2(A) + h\nu$	1.5×10^5	9
7	$N_2(C) \rightarrow N_2(B) + h\nu$	3×10^7	9
8	$N_2(a^1) \rightarrow N_2 + h\nu$	8.55×10^3	3
9	$N(^2D) \rightarrow N + h\nu$	1.06×10^{-5}	13
10	$N(^2P) \rightarrow N(^2D) + h\nu$	7.9×10^{-2}	13

References

[1] Arijs, E., Nevejans, D., and Ingels, J. (1987), Stratospheric positive ion composition measurements and acetonitrile detection: a consistent picture?. *International journal of mass spectrometry and ion processes*, *81*, 15-31.

[2] Chipperfield, M. P. (1999), Multiannual simulations with a three-dimensional chemical transport model. *J. Geophys. Res.: Atmospheres*, *104*(D1), 1781-1805.

[3] Gordillo-Vázquez, F. J. (2008), Air plasma kinetics under the influence of sprites. *Journal of Physics D: Applied Physics*, *41*(23), 234016.

[4] Howard, C. J., Bierbaum, V. M., Rundle, H. W., and Kaufman, F. (1972), Kinetics and mechanism of the formation of water cluster ions from O_2^+ and H_2O. *The Journal of Chemical Physics*, *57*(8), 3491-3497.

[5] Kamaratos, E. (2009), Comment on "Plasma chemistry of sprite streamers" by DD Sentman, HC Stenbaek-Nielsen, MG McHarg, and JS Morrill. *J. Geophys. Res.: Atmospheres*, *114*(D8).

[6] Kazil, J. (2002), The University of Bern atmospheric ion model: Time-dependent ion modeling in the stratosphere, mesosphere and lower thermosphere. *PhD thesis, University of Bern, Switzerland*.

[7] Kopp, E. (1996), Electron and ion densities in the upper atmosphere: data analysis and interpretation (Dieminger, W. and Hartmann, G.K. and Leitinger, R.). *Springer*.

[8] Kopp, E., and Fritzenwallner, J. (1997), Chlorine and bromine ions in the D-region. *Advances in Space Research*, *20*(11), 2111-2115.

[9] Kossyi, I. A., Kostinsky, A. Y., Matveyev, A. A., and Silakov, V. P. (1992), Kinetic scheme of the non-equilibrium discharge in nitrogen-oxygen mixtures. *Plasma Sources Science and Technology*, *1*(3), 207.

[10] Kruger, V. R., and Olander, D. R. (1976), Oxygen radiolysis by modulated molecular beam mass spectrometry. *The Journal of Physical Chemistry*, *80*(15), 1676-1684.

[11] Makhlouf, U., Picard, R. H., and Winick, J. R. (1995), Photochemical-dynamical modeling of the measured response of airglow to gravity waves: 1. Basic model for OH airglow. *J. Geophys. Res.: Atmospheres*, *100*(D6), 11289-11311.

[12] Popov, N. A. (2009), Associative ionization reactions involving excited atoms in nitrogen plasma. *Plasma physics reports*, *35*(5), 436-449.

[13] Rees, M. H., and Rees, N. H. (1989), *Physics and chemistry of the upper atmosphere* (Vol. 1). Cambridge University Press.

[14] Sander, S. P., Golden, D. M., Kurylo, M. J., Moortgat, G. K., Wine, P. H., Ravishankara, A. R., Kolb, C. E., Molina, M. J., Finlayson-Pitts, B. J., and Orkin, V. L. (2006), Chemical kinetics and photochemical data for use in atmospheric studies evaluation number 15. Pasadena, CA: Jet Propulsion Laboratory, National Aeronautics and Space Administration, 2006.

[15] Sentman, D. D., Stenbaek-Nielsen, H. C., McHarg, M. G., and Morrill, J. S. (2008), Correction to "Plasma chemistry of sprite streamers". *J. Geophys. Res.: Atmospheres, 113*(D14).

[16] Viggiano, A. A. (2006), Much improved upper limit for the rate constant for the reaction of O_2^+ with N_2. *The Journal of Physical Chemistry A*, *110*(41), 11599-11601.

[17] Woodall, J., Agúndez, M., Markwick-Kemper, A. J., and Millar, T. J. (2007), The UMIST database for astrochemistry 2006. *Astronomy and Astrophysics*, *466*(3), 1197-1204.

[18] Yaron, M., Von Engel, A., and Vidaud, P. H. (1976), The collisional quenching of $O_2^*(^1\Delta_g)$ by NO and CO_2. *Chemical Physics Letters*, *37*(1), 159-161.

ANNEX 2

Cross-section data

The cross-sections used for the calculations of reaction rate coefficients during electric-field-driven processes with the BOLSIG+ solver are listed below.

Ionization

$e + N_2 \rightarrow N_2^+ + 2e$ threshold energy: 15.6 eV [1,2]	
Energy (eV)	Cross section (m^2)
15.6	0.0000e+0
16	1.9500e-22
16.5	4.2800e-22
17	6.6000e-22
17.5	9.1100e-22
18	1.2000e-21
18.5	1.5160e-21
19	1.8410e-21
19.5	2.1300e-21
20	2.5020e-21
21	3.1810e-21
22	3.8690e-21
23	4.5570e-21
25	5.9240e-21
30	9.5790e-21
34	1.1718e-20
45	1.6461e-20
60	2.0181e-20
75	2.2134e-20
100	2.3436e-20
150	2.2692e-20
200	2.1018e-20
300	1.7763e-20
500	1.3485e-20
700	1.0788e-20
1000	8.5560e-21
1500	7.4400e-21

$e + N_2 \rightarrow N^+ + N + 2e$ threshold energy: 30 eV [2,3]	
Energy (eV)	Cross section (m^2)
29.5	0.000000e+0
30	3.250000e-22
35	9.040000e-22
40	1.660000e-21
45	2.450000e-21
50	3.190000e-21
55	3.900000e-21
60	4.380000e-21
65	4.820000e-21
70	5.230000e-21
75	5.610000e-21
80	5.870000e-21
85	6.050000e-21
90	6.320000e-21
95	6.450000e-21
100	6.560000e-21
110	6.600000e-21
120	6.610000e-21
140	6.520000e-21
160	6.330000e-21
180	5.950000e-21
200	5.660000e-21
225	5.160000e-21
250	4.930000e-21
275	4.580000e-21
300	4.380000e-21
350	3.930000e-21
400	3.510000e-21
450	3.240000e-21
500	2.990000e-21
550	2.740000e-21
600	2.480000e-21
650	2.340000e-21
700	2.170000e-21
750	2.050000e-21
800	2.000000e-21
850	1.920000e-21
900	1.830000e-21
950	1.760000e-21
1000	1.670000e-21

$e + N_2 \rightarrow N^+ + N(^2D) + 2e$ threshold energy: 30 eV [3]	
Energy (eV)	Cross section (m^2)
30	9.750000e-23
33	2.050000e-22
36	3.750000e-22
39	5.400000e-22
42	7.850000e-22
45	9.600000e-22
50	1.350000e-21
55	1.700000e-21
60	1.950000e-21
70	2.350000e-21
80	2.650000e-21
90	2.900000e-21
100	3.050000e-21
120	3.150000e-21
140	3.100000e-21
160	3.030000e-21
180	2.920000e-21
200	2.800000e-21
250	2.480000e-21
300	2.220000e-21
350	1.980000e-21
400	1.830000e-21

$e + O_2 \rightarrow O_2^+ + 2e$ threshold energy: 13 eV [5]	
Energy (eV)	Cross section (m^2)
13	1.1700e-22
15.5	7.3000e-22
18	1.6400e-21
23	3.6600e-21
28	5.6300e-21
33	7.5800e-21
38	9.2900e-21
43	1.0800e-20
48	1.1900e-20
53	1.2900e-20
58	1.3600e-20
63	1.4200e-20
68	1.4700e-20
73	1.5000e-20
78	1.5100e-20
83	1.5300e-20
88	1.5500e-20
93	1.5600e-20
98	1.5600e-20
108	1.5400e-20
118	1.5300e-20
138	1.5000e-20
158	1.4800e-20
178	1.4300e-20
198	1.3900e-20
223	1.3700e-20
248	1.3100e-20
273	1.2400e-20
298	1.2000e-20
348	1.1300e-20
398	1.0500e-20
448	9.8300e-21
498	9.2300e-21
548	8.8200e-21
598	8.2700e-21
648	8.0000e-21
698	7.6100e-21
748	7.2000e-21
798	6.8600e-21
848	6.7100e-21
898	6.4300e-21
948	6.1700e-21
998	5.9700e-21

$e + O_2 \rightarrow O^+ + O + 2e$ threshold energy: 23 eV [5]	
Energy (eV)	Cross section (m^2)
23	1.670000e-22
28	7.810000e-22
33	1.690000e-21
38	2.580000e-21
43	3.330000e-21
48	4.190000e-21
53	4.900000e-21
58	5.530000e-21
63	6.210000e-21
68	6.790000e-21
73	7.170000e-21
78	7.510000e-21
83	8.010000e-21
88	8.270000e-21
93	8.550000e-21
98	8.710000e-21
108	9.000000e-21
118	9.100000e-21
138	9.130000e-21
158	9.050000e-21
178	8.910000e-21
198	8.640000e-21
223	8.300000e-21
248	7.940000e-21
273	7.550000e-21
298	7.210000e-21
348	6.590000e-21
398	6.110000e-21
448	5.620000e-21
498	5.260000e-21
548	4.870000e-21
598	4.570000e-21
648	4.320000e-21
698	4.150000e-21
748	3.880000e-21
798	3.690000e-21
848	3.550000e-21
898	3.360000e-21
948	3.260000e-21
998	3.170000e-21

Attachment

$e + O_2 \rightarrow O^- + O$ [1] threshold energy: 5.38 eV	
Energy (eV)	Cross section (m^2)
4.4	0.0000e+0
4.9	0.0000e+0
5.38	2.3000e-23
5.86	7.2000e-23
6.1	1.0800e-22
6.48	1.3800e-22
6.77	1.5200e-22
7.05	1.5600e-22
7.3	1.4800e-22
7.53	1.3100e-22
7.77	1.1000e-22
8	8.4000e-23
8.25	5.4000e-23
8.73	2.8000e-23
9.2	1.4000e-23
9.68	8.0000e-24
10.15	8.0000e-24
11.35	8.0000e-24
10000	0.0000e+0

Dissociation

$e + N_2 \rightarrow N + N + e$ threshold energy: 13.5 eV [3,4]	
Energy (eV)	Cross section (m^2)
13.5	4.000000e-22
14	8.600000e-22
14.5	1.250000e-21
15	1.670000e-21
15.5	2.040000e-21
16	2.420000e-21
17	3.120000e-21
18	3.750000e-21
19	4.370000e-21
20	4.910000e-21
22	5.850000e-21
24	6.670000e-21
26	7.350000e-21
28	7.820000e-21
30	8.230000e-21
33	8.730000e-21
36	9.120000e-21
39	9.420000e-21
42	9.700000e-21
45	9.900000e-21
50	1.020000e-20
55	1.030000e-20
60	1.040000e-20
70	1.060000e-20
80	1.080000e-20
90	1.070000e-20
100	1.050000e-20
120	1.010000e-20
140	9.600000e-21
160	9.100000e-21
180	8.650000e-21
200	8.230000e-21
250	7.250000e-21
300	6.500000e-21
350	5.850000e-21
400	5.320000e-21

$e + N_2 \rightarrow N + N(^2D) + e$ threshold energy: 13.5 eV [3]	
Energy (eV)	Cross section (m^2)
13.5	4.000000e-22
14	8.600000e-22
14.5	1.250000e-21
15	1.670000e-21
15.5	2.040000e-21
16	2.420000e-21
17	3.120000e-21
18	3.750000e-21
19	4.370000e-21
20	4.910000e-21
22	5.850000e-21
24	6.670000e-21
26	7.350000e-21
28	7.820000e-21
30	8.330000e-21
33	8.940000e-21
36	9.500000e-21
39	9.960000e-21
42	1.050000e-20
45	1.090000e-20
50	1.160000e-20
55	1.200000e-20
60	1.240000e-20
70	1.300000e-20
80	1.350000e-20
90	1.360000e-20
100	1.360000e-20
120	1.330000e-20
140	1.270000e-20
160	1.210000e-20
180	1.160000e-20
200	1.100000e-20
250	9.730000e-21
300	8.720000e-21
350	7.830000e-21
400	7.150000e-21

$e + N_2 \rightarrow N + N(^2P) + e$ threshold energy: 14.5 eV [3]	
Energy (eV)	Cross section (m^2)
14.5	2.200000e-22
15	3.500000e-22
15.5	5.400000e-22
16	8.000000e-22
17	1.270000e-21
18	1.830000e-21
19	2.380000e-21
20	2.900000e-21
22	3.920000e-21
24	4.780000e-21
26	5.560000e-21
28	6.220000e-21
30	6.750000e-21
33	7.220000e-21
36	7.570000e-21
39	7.770000e-21
42	7.900000e-21
45	8.000000e-21
50	8.100000e-21
55	8.070000e-21
60	8.050000e-21
70	7.950000e-21
80	7.700000e-21
90	7.420000e-21
100	7.170000e-21
120	6.630000e-21
140	6.220000e-21
160	5.850000e-21
180	5.530000e-21
200	5.250000e-21
250	4.700000e-21
300	4.300000e-21
350	3.950000e-21
400	3.700000e-21

$e + O_2 \rightarrow O + O + e$ threshold energy: 6.12 eV [6]	
Energy (eV)	Cross section (m^2)
6.12	0.000000e+0
13.5	2.200000e-21
18.5	5.290000e-21
21	5.650000e-21
23.5	5.250000e-21
28.5	5.870000e-21
33.5	6.630000e-21
38.5	6.100000e-21
48.5	5.340000e-21
58.5	4.440000e-21
73.5	3.660000e-21
98.5	3.310000e-21
148.5	2.960000e-21
198.5	2.910000e-21

$e + O_2 \rightarrow O + O(^1D) + e$ threshold energy: 8.4 eV [9]	
Energy (eV)	Cross section (m^2)
8.4	0.000000e+0
9.4	1.000000e-20
30	1.200000e-20
50	1.170000e-20
100	9.400000e-21
1000	0.000000e+0
1100	0.000000e+0

$e + O_2 \rightarrow O + O(^1S) + e$ threshold energy: 15.6 eV [7]	
Energy (eV)	Cross section (m^2)
16	3.500000e-23
20	9.200000e-23
24	1.260000e-22
28	1.470000e-22
32	1.610000e-22
36	1.730000e-22
40	1.820000e-22
45	1.920000e-22
50	1.970000e-22
60	2.040000e-22
70	2.070000e-22
80	2.080000e-22
90	2.060000e-22
100	2.040000e-22
120	1.980000e-22
140	1.900000e-22
160	1.820000e-22
180	1.750000e-22
200	1.670000e-22
250	1.530000e-22
300	1.390000e-22
350	1.260000e-22
400	1.160000e-22
450	1.080000e-22
500	1.020000e-22
600	9.200000e-23
700	8.200000e-23
800	7.500000e-23
900	6.900000e-23
1000	6.500000e-23

Excitation

$e + N_2 \rightarrow N_2(A) + e$ threshold energy: 6.17 eV [1]	
Energy (eV)	Cross section (m^2)
6.17	0.0000e+0
7	1.0000e-23
7.8	2.8000e-23
8.5	4.3000e-23
9	5.7000e-23
10	8.2000e-23
11	1.0000e-22
12	1.2000e-22
13	1.3000e-22
14	1.4000e-22
16	1.5000e-22
17	1.5000e-22
18	1.4000e-22
20	1.2000e-22
22	1.0000e-22
24	8.9000e-23
26	7.6000e-23
30	5.9000e-23
34	4.9000e-23
40	3.9000e-23
50	3.4000e-23
70	7.0000e-24
150	0.0000e+0

$e + N_2 \rightarrow N_2(B) + e$ threshold energy: 7.35 eV [1]	
Energy (eV)	Cross section (m^2)
7.35	0.0000e+0
8	3.6200e-22
9	9.3800e-22
10	1.5080e-21
11	1.8630e-21
12	2.0030e-21
13	1.9900e-21
14	1.8160e-21
15	1.6150e-21
16	1.4470e-21
17	1.3070e-21
18	1.1990e-21
20	1.1120e-21
22	9.5100e-22
26	8.0400e-22
30	6.7700e-22
34	5.6300e-22
40	4.2900e-22
50	2.6800e-22
70	6.7000e-23
150	0.0000e+0

$e + N_2 \rightarrow N_2(C) + e$ threshold energy: 11.03 eV [1]	
Energy (eV)	Cross section (m^2)
11.03	0.0000e+0
11.5	2.7000e-22
12	6.2000e-22
12.5	1.3100e-21
13	2.9000e-21
13.5	4.9000e-21
13.8	6.2000e-21
14	6.5000e-21
14.2	6.4000e-21
14.5	6.3000e-21
15	5.5000e-21
16	4.3000e-21
17	3.5000e-21
18	3.0000e-21
19	2.7000e-21
20	2.5000e-21
22	2.1000e-21
24	1.7700e-21
26	1.5000e-21
28	1.2800e-21
30	1.1100e-21
36	7.8000e-22
40	6.3000e-22
50	3.9000e-22
70	1.5000e-22
100	1.5000e-23
150	0.0000e+0

$e + N_2 \rightarrow N_2(a^1) + e$ threshold energy: 8.55 eV [1]	
Energy (eV)	Cross section (m^2)
8.55	0.0000e+0
9	1.2700e-22
14	1.4740e-21
15	1.7150e-21
16	1.9160e-21
17	2.0230e-21
18	1.9900e-21
19	1.9230e-21
20	1.8490e-21
24	1.6210e-21
26	1.5280e-21
30	1.3670e-21
40	1.0650e-21
50	8.5100e-22
70	6.0300e-22
100	4.0200e-22
150	2.6800e-22
200	2.0100e-22
250	1.6100e-22
300	1.3400e-22
500	8.2000e-23
700	6.0000e-23
1000	4.2000e-23

$e + O_2 \rightarrow O_2(a) + e$ threshold energy: 0.977 eV [1]	
Energy (eV)	Cross section (m^2)
0.977	0.0000e+0
1.5	5.8000e-23
2	1.5300e-22
3	3.8000e-22
3.5	4.9000e-22
4	5.7000e-22
5	7.4000e-22
5.62	8.2500e-22
5.91	8.6200e-22
6.19	8.8800e-22
6.53	9.0800e-22
6.99	9.1400e-22
7.61	8.9100e-22
7.89	8.6300e-22
8.96	7.6800e-22
1.004	6.7900e-22
1.3	5.2700e-22
1.51	4.5500e-22
1.75	3.8700e-22
2.05	3.2400e-22
2.49	2.5600e-22
3.09	1.9600e-22
4.1	1.3700e-22
4.5	1.2000e-22
10000	0.0000e+0

$e + N_2 \rightarrow N_2(a'^1) + e$ threshold energy: 8.4 eV [1]	
Energy (eV)	Cross section (m^2)
8.4	0.0000e+0
9	6.7000e-23
11	3.0100e-22
13	5.3600e-22
14	6.4300e-22
15	6.9700e-22
16	5.7000e-22
17	4.2900e-22
18	3.4800e-22
19	3.0800e-22
20	2.7500e-22
24	2.0100e-22
30	1.5400e-22
40	1.2400e-22
50	1.2100e-22
70	1.0000e-22
150	6.7000e-23
500	0.0000e+0

$e + O_2 \rightarrow O_2(b) + e$ threshold energy: 1.627 eV [1]	
Energy (eV)	Cross section (m^2)
1.627	0.0000e+0
2	2.6000e-23
3	9.7000e-23
3.5	1.3300e-22
4	1.4900e-22
5	1.8200e-22
5.69	1.9400e-22
6.54	1.9400e-22
7.34	1.9100e-22
8.41	1.8300e-22
9.26	1.7400e-22
10	1.6000e-22
13	1.3000e-22
14.9	1.3000e-22
17	1.3000e-22
19.4	1.2500e-22
20.7	1.2500e-22
22.5	1.1000e-22
24	1.0000e-22
28	8.0000e-23
35.1	6.3000e-23
41.9	1.8000e-23
45.1	5.0000e-24
1000	0.0000e+0

References

[1] http://jila.colorado.edu/~avp/collision_data/ (download 3 January 2012)

[2] Itikawa, Y. (2006), Cross sections for electron collisions with nitrogen molecules. *Journal of physical and chemical reference data*, *35*(1), 31-53.

[3] Zipf, E. C., Espy, P. J., and Boyle, C. F. (1980), The excitation and collisional deactivation of metastable N (²P) atoms in auroras. *J. Geophys. Res.: Space Physics*, *85*(A2), 687-694.

[4] Cosby, P. C. (1993a), Electron-impact dissociation of nitrogen. *The Journal of chemical physics*, *98*(12), 9544-9553.

[5] Itikawa, Y. (2009), Cross sections for electron collisions with oxygen molecules. *Journal of Physical and Chemical Reference Data*, *38*(1), 1-20.

[6] Cosby, P. C. (1993b), Electron-impact dissociation of oxygen. *The Journal of chemical physics*, *98*(12), 9560-9569.

[7] LeClair, L. R., and McConkey, J. W. (1993), Selective detection of $O(^1S_0)$ following electron impact dissociation of O_2 and N_2O using a XeO^* conversion technique. *The Journal of chemical physics*, *99*(6), 4566-4577.

[8] Luque, A., and Gordillo-Vázquez, F. J. (2012), Mesospheric electric breakdown and delayed sprite ignition caused by electron detachment. *Nature Geoscience*, *5*(1), 22.

[9] Eliasson, B. (1986), Basic data for modeling of electrical discharges in gases: oxygen. *Asea Brown Boveri Corporate Research Report*, KLR86-11C.

Chen XU

L'impact du streamer de bleu jet sur la chimie stratosphérique

Résumé :
L'objectif des travaux dans cette thèse est de mener une étude détaillée de l'impact potentiel des streamers des jets bleus (BJs) sur la chimie stratosphérique via le développement d'un modèle de chimie plasma pour identifier les mécanismes clés associés aux différentes échelles temporelles (millisecondes, centaines de secondes, jours). Après une revue des connaissances dans le domaine d'étude, le modèle de chimie du plasma développé est présenté ainsi que les paramétrisations permettant de modéliser la décharge du streamer. Puis les caractéristiques des simulations (cas d'étude et initialisation) sont décrites. La comparaison à l'étude de W2015 est consacrée à la validation du modèle ainsi qu'à l'analyse des résultats obtenus en fonction de la paramétrisation considérée pour représenter le streamer: i) paramétrisation simplifiée avec impulsion électrique simple utilisée dans les études citées, ii) paramétrisation réaliste développée dans le cadre de ces travaux de thèse avec une impulsion électrique issue d'un modèle électrodynamique. L'étude se focalise sur la moyenne stratosphère (27 km) au cœur de la couche d'ozone. L'étude systématique de l'impact de la décharge électrique des BJ sur la perturbation du système chimique est dédiée en fonction de l'altitude considérée entre 20 km et 50 km d'altitude aux différentes échelles de temps.
Mots clés: streamer de jet bleu, ozone stratosphérique, modèle de chimie à plasma neutre, paramétrisation de streamer électrodynamique, azote, chlore, brome

The effect of blue jet streamer on stratospheric chemistry

Summary:
This thesis carried out a detailed study of the potential impact of blue jet (BJ) streamers on stratospheric chemistry with the development of a plasma chemistry model, and identified the key mechanisms associated with different time scales (e.g. milliseconds, hundreds of seconds, days). After a review of knowledge in the field of study, the model development of plasma chemistry is presented, as well as the parameterizations of streamer discharge. Then the characteristics of the simulations (case study and initialization) are described. Compared to the study of W2015, the model validations focus on the altitude of 27 km, where ozone is abundant. The results were analyzed according to the parametrization used to represent the streamers, namely: i) a simplified parameterization with simple electrical impulses used in the cited studies, ii) a realistic parameterization from an electrodynamic model. A systematic study of the BJ streamer impacts on the disturbance of the chemical system is then performed at the altitudes between 20 km and 50 km. The chemical impact study focuses mainly on the nitrogen, chlorine and bromine families at different time scales.
Keywords: blue jet streamer, stratospheric ozone, neutral-plasma chemistry model, electrodynamic streamer parametrization, nitrogen, chlorine, bromine

LPC2E-CNRS
3A avenue de la Recherche Scientifique
45071 Orléans Cedex 2, FRANCE